Simulation of Thermally Assisted Forming of Aluminum Sheet

Samenstelling van de promotiecommissie:

voorzitter en secretaris:	
Prof. dr. ir. F. Eising	Universiteit Twente
promotor:	
Prof. dr. ir. J. Huétink	Universiteit Twente
assistent promotor:	
Dr. ir. A.H. van den Boogaard	Universiteit Twente
leden:	
Dr. Y. An	Corus RD & T
Prof. dr. ir. A.J. Huis in 't Veld	Universiteit Twente
Prof. Dr.-Ing. M. Merklein	Universität Erlangen
Prof. dr. ir. D. Schipper	Universiteit Twente
Prof. dr. ir. J. Sietsma	Technische Universiteit Delft

ISBN 978-90-77172-56-8

1st Printing May 2010

Keywords: plasticity, material models, warm forming, stretch forming, intermediate annealing, aluminum

This thesis was prepared with LaTeX by the author and printed by Ipskamp Drukkers, Enschede, from an electronic document.

SIMULATION OF THERMALLY ASSISTED FORMING OF ALUMINUM SHEET

PROEFSCHRIFT

ter verkrijging van
de graad van doctor aan de Universiteit Twente,
op gezag van de rector magnificus,
prof. dr. H. Brinksma,
volgens besluit van het College voor Promoties
in het openbaar te verdedigen
op donderdag 24 juni 2010 te 15.00 uur.

door

Srihari Kurukuri

geboren op 02 januari 1974
te Sangayagudem, India

Dit proefschrift is goedgekeurd door de promotor:

Prof. dr. ir. J. Huétink

assistent promotor:

Dr. ir. A.H. van den Boogaard

Contents

Summary

Driven by a desire for weight reduction, the use of aluminum sheet is increasingly taken into consideration in the industry. Apart from the aerospace industry, where aluminum is the first choice material for most parts, the interest from the automotive industry is growing. This concerns *e.g.* inner and outer body panels, and hydroformed aluminum tube. The formability of aluminum, however, is in general less than *e.g.* steel. Therefore in many industrial forming processes for aluminum the mechanical loading is combined with a thermal component *i.e.* deformation at elevated temperatures or annealing between deformation steps.

A particular example from the aerospace industry is the stretching of aluminum parts in a number of stages with intermediate annealing treatments. The heating and cooling cycles are time consuming and should therefore be minimized. In the process of warm forming, parts of the blank are heated and other parts are cooled to increase the formability. However, the temperature distribution introduces an extra degree of freedom in the production process for which experience is lacking. A good simulation tool will reduce the trial-and-error process that would be necessary to optimize the process conditions.

In the research on warm forming, three different aluminum alloys: Al–Mg alloy (AA 5754) and Al–Mg–Si alloys (AA 6016 and AA 6061) used in the automotive industry are considered. In the stretch forming with intermediate heat treatments, aerospace Al–Cu alloy (AA 2024) is considered. In non-heat treatable Al–Mg alloys, hardening is mainly due to the presence of solute atoms in solid solution and in heat treatable Al–Mg–Si and Al-Cu alloys, strengthening is determined by precipitates formed during ageing treatment.

In this thesis a numerical model is developed to simulate the thermally assisted forming of aluminum sheet. An important part of the numerical model is the modeling of the material behavior. For room temperature forming, the material behavior of aluminum sheet is completely determined by work hardening and almost independent of the strain rate. Above 125 °C, the strain rate sensitivity increases. Hence, apart from the effect of solutes and precipitates, material models will also need to consider temperature and strain rate effects on work hardening. Material models based on the underlying physical processes are expected to have a larger range of usability in this respect.

In this research, two such physically based hardening models: the Bergström and the Nes models are compared. These models incorporate the influence of the temperature and strain rate effects on the flow stress and on the hardening rate based on storage and dynamic recovery of dislocations. The Nes model directly takes into account the chemical composition such as the solute concentrations, grain size, volume fraction and size of the precipitates. Thus, the Nes model is quite capable to describe the changing material behavior during the ageing of heat treatable alloys. The Nes model also includes the DSA effect in

the non-heat treatable alloys. Both the Bergström and the Nes models can be fitted well to the results of monotonic tensile tests. The Nes model gives better prediction than the Bergström model. Large differences appear, however, if strain rate jumps are applied. After a strain rate jump, the Bergström model grossly overestimates the strain increment that is needed to reach the corresponding constant strain rate curve. With the Nes model, an initial jump in the flow stress is observed, followed by an asymptotic curve approaching the new constant strain rate curve, which is a better representation of the experiments.

The biaxial stress–strain response and the anisotropy of the aluminum sheet is described by accurate planar anisotropic yield functions: the Vegter and Barlat Yld2000 models. The biaxial stress–strain response of the material is experimentally determined by uniaxial stress, plane strain, simple shear and equi-biaxial stress tests and used as an input to the yield functions.

The implemented models for warm forming are first verified with uniaxial tensile test simulations. At room temperature the predicted localization strain corresponds to the experimental ultimate strain. At elevated temperatures, the Nes model predicts the localization strain very well, much better than the Bergström model. The industrial relevance of the models is further confirmed with warm deep drawing of cylindrical and square cups. The favorable comparison found between the numerical and experimental results shows that a promising future exists for the use of the implemented models to simulate industrial stamping operations.

The effect of anisotropy in deep drawing is generally viewed based on the number of ears, their location with respect to the RD and their amplitude. In this work, the effect of temperature on anisotropy is studied both experimentally and numerically by measuring the number, position and amplitude of the ears. In the simulations, the effect of temperature on anisotropy is studied by identifying the Vegter yield function data from crystal plasticity analysis by assuming the activation of more slip systems at higher temperatures.

In the stretch forming of aircraft skin parts with intermediate heat treatments, the work hardening during stretching is described with a phenomenological power law model and the physically based Nes model. The stress removal during heat treatment is modeled based on the observed physics such as the particle coarsening and the static recovery. The results are compared with the phenomenological approach by assuming the initial mechanical properties are restored during heat treatment. It can be concluded that the physics based material modeling gives better results.

Samenvatting

Producten uit plaatmateriaal worden met het oog op gewichtsreductie steeds vaker uit aluminum materialen vervaardigd. Naast de vliegtuigbouw, waar aluminum de eerste keus is voor veel onderdelen, is er een groeiende interesse vanuit de automobiel industrie. Hierbij gaat het vooral om in- en uitwendige plaatonderdelen en gehydrovormde buizen. Alhoewel aluminum vele voordelen heeft ten opzichte van staal, is het vaak moeilijker vervormbaar. Hierdoor treden er sneller materiaaldefecten op. Om deze defecten te voorkomen, wordt de mechanische belasting die opgelegd wordt tijdens het productieproces vaak gecombineerd met een thermische component. Dit wil zeggen dat omvorming plaatsvindt onder een verhoogde temperatuur (warmvormen) of er worden warmtebehandelingen toegepast tijdens het omvormingsproces.

Een specifiek voorbeeld vanuit de vliegtuigbouw is het strekvormen van aluminum plaatonderdelen. Het strekvormen wordt uitgevoerd in meerdere stappen, waarbij het materiaal tussen de stappen door gerelaxeerd wordt. Het verwarmen en afkoelen van het product, wat onderdeel uitmaakt van het relaxatieproces, is een tijdrovend proces. Het aantal benodigde stappen moet daarom worden geminimaliseerd om het product zo goedkoop mogelijk te produceren. Tijdens het warmvormen worden bepaalde delen van de matrijzen verwarmd en worden andere delen afgekoeld. Dit gebeurt om de vervormbaarheid van het materiaal te verhogen. De temperatuurverdeling over de matrijs introduceert een extra vrijheidsgraad in het productieproces waarvoor extra kennis vereist is. Goede simulatietechnieken zullen daarom de *trial and error* fases van het procesontwerp verkorten en zo het productieproces optimaliseren.

Voor het onderzoek naar warmvormen wordt er gekeken naar drie typen aluminum legeringen: Al–Mg legering (AA 5754-O) en twee Al–Mg–Si legeringen (AA 6016 en AA 6061). Deze legeringen worden vooral toegepast in de automobielindustrie. Voor het strekvormproces met achtereenvolgende warmtebehandelingen wordt gekeken naar de legering Al–Cu (AA 2024). Deze legering wordt veel toegepast in de vliegtuigbouw. In de Al–Mg legeringen, die niet geschikt zijn voor warmtebehandelingen, wordt versteviging van het materiaal veroorzaakt door de aanwezigheid van opgeloste atomen. Voor de Al–Mg–Si en Al–Cu legeringen, die geschikt zijn voor warmtebehandelingen, wordt versteviging van het materiaal veroorzaakt door precipitaten die tijdens het verouderingsproces worden gevormd. In dit proefschrift wordt een numeriek model beschreven dat gebruikt kan worden voor het simuleren van aluminum omvormprocessen met een thermische component. Een belangrijk onderdeel van dit numerieke model is de modellering van het materiaalgedrag. Tijdens het omvormen van aluminum bij kamertemperatuur wordt de versteviging van het materiaal beschreven door de geïntroduceerde hoeveelheid rek in het materiaal en is deze verstevi-

ging nagenoeg onafhankelijk van de snelheid waarmee dit gebeurd. Boven de 125 °C neemt reksnelheidsafhankelijkheid toe. Daarom zullen naast de invloed van opgeloste atomen en precipitaten op de hoeveelheid versteviging ook temperatuurs- en reksnelheidseffecten meegenomen moeten worden. Materiaalmodellen die gebaseerd zijn op deze fysische aspecten zullen waarschijnlijk een breed toepassingsgebied hebben voor dergelijke productieprocessen.

In dit onderzoek worden twee fysisch gebaseerde modellen vergeleken: het Bergström model en het Nes model. De invloed van temperatuurs- en reksnelheidseffecten op de vloeispanning en de verstevigingssnelheid worden in deze modellen meegenomen door de opslag en het dynamisch herstel van dislocaties in rekening te brengen. Het Nes model is gebaseerd op de chemische compositie van het materiaal, zoals de concentratie opgeloste atomen, korrelgrootte, volumefracties en de grootte van de precipitaten. Het Nes model zal daarom geschikt zijn om het materiaalgedrag te beschrijven tijdens het verouderingsproces van aluminum. Daarnaast beschrijft het Nes model het dynamisch verouderingsgedrag dat voorkomt in legeringen die niet geschikt zijn voor warmtebehandelingen. Beide modellen kunnen de resultaten van een monotone trekproef accuraat beschrijven, hoewel de benadering van het Nes model nauwkeuriger blijkt. Grote verschillen tussen de modellen ontstaan echter wanneer sprongen in de reksnelheid worden geïntroduceerd. Na een sprong in de reksnelheid geeft het Bergström model een grove overschatting van de incrementele rek die nodig is om de bijbehorende constante reksnelheidscurve te beschrijven. Het Nes model beschrijft een initiële sprong in de vloeispanning gevolgd door een asymptotische curve die de nieuwe constante reksnelheidscurve benaderd. Dit geeft een betere representatie van de experimentele resultaten.

De biaxiale trek–rek respons en het anisotrope materiaalgedrag van aluminum wordt beschreven door accurate planaire vloeicriteria: het Vegter en het Barlat Yld2000 model. De biaxiale trek–rek respons van het materiaal is experimenteel bepaald door middel van uni-axiale, vlakvervormings, afschuiving en equi-biaxiale spanningstesten. De resultaten van de experimenten worden gebruikt als input voor de yield criteria.

Voor warmvormen zijn de geïmplementeerde modellen geverifieerd aan de hand van uni-axiale trekproef simulaties. De rek waar insnoering wordt voorspeld tijdens kamertemperatuur komt overeen met experimenteel bepaalde waarden. Voor verhoogde temperaturen voorspelt het Nes model de rek waar insnoering ontstaat beter dan het Bergström model. De industriële relevantie van de modellen is verder bevestigd aan de hand van het warm dieptrekken van cilindrische en vierkante bakjes. Uit de vergelijking van experimentele met numerieke resultaten blijkt dat deze zeer goed overeenkomen. Geconcludeerd kan worden dat de geïmplementeerde modellen een veelbelovende toekomst hebben voor het simuleren van industriële omvormprocessen.

Het effect van het anisotrope materiaalgedrag tijdens dieptrekprocessen wordt bepaald door het aantal gevormde oren, de locatie van deze oren ten opzichte van de rolrichting en de mate waarin de oren voorkomen. De temperatuursafhankelijkheid van het anisotrope materiaalgedrag is zowel numeriek als experimenteel bestudeerd aan de hand van deze parameters. De Vegter parameters die gebruikt zijn voor het bestuderen van de temperatuursafhankelijkheid zijn bepaald door kristalplasticiteit analyses. Bij deze analyses is aangenomen dat het aantal geactiveerde glijsystemen toeneemt bij een stijging van de temperatuur.

In het strekvormproces met achtereenvolgende warmtebehandelingen van vliegtuigplaatonderdelen, wordt materiaalversteviging tijdens het strekken beschreven door een fenomenologisch model gebaseerd op machtsfuncties en het fysisch gebaseerde Nes model. Relaxatie van het materiaal tijdens warmtebehandelingen wordt gemodelleerd aan de hand van geobserveerde fysica zoals korrelgroei en statisch herstel. Resultaten zijn vergeleken met de fenomenologische benadering, aangenomen dat materiaaleigenschappen zich na een warmtebehandeling volledig herstellen tot de begincondities. Geconcludeerd kan worden dat het fysisch gebaseerde model betere resultaten oplevert.

Preface

The research described in this thesis was carried out at the Applied Mechanics group, University of Twente, the Netherlands. The results from the former project ME97033 of the Netherlands Institute for Metals Research on the forming of light metals form the basis of the current project. Within project ME97033, experiments were performed to study the formability of an Al–Mg and an Al–Mg–Si alloy. During stretching or drawing of rectangular or cylindrical cups the flange was heated to temperatures up to 250 °C. The limiting drawing ratio for both alloys could in this way be increased by 25%. Simulations performed with material models that were available gave a qualitative description of the experiments with the Al–Mg alloy, but for precipitating alloys these models have limited value. Thus the focus of the current project is on modeling sheet forming of precipitating alloys, following the industrial interest in Al–Mg–Si and Al–Cu alloys. The Netherlands Institute for Metals Research (the current M2i) accepted the proposal and the project was carried out under project number MC1.02106 in the framework of the Strategic Research Program of the Materials Innovation Institiute, M2i (http://www.m2i.nl) in the Netherlands.

Acknowledgements

This thesis would not have been possible without the help and support of many people, and I would like to take this opportunity to thank all of them here. First of all I would like to thank Prof. Han Huétink and Ton van den Boogaard for the opportunity to do this research at the Mechanics of Forming Technology group, University of Twente. I am very thankful to you for the positive and open working environment as it gives a lot of encouragement and motivation.

This thesis would not have reached this far without Ton van den Boogaard who not only served as my supervisor but also encouraged and supporteded me throughout this project. Your way of supervising is incredibly supportive and stimulating and I enjoyed every bit of this research.

Many thanks to all permanent members of the group—Bert Geijselaers, Timo Meinders, Wilko Emmens, Harm Wisselink and the former and present researchers of the group—for their time, valuable suggestions and interesting ideas during DiekA group meetings. I want to thank in particular Semih Perdahcioğlu, for sharing his technical as well as administrative experiences in shaping up this thesis. Many thanks to Muhammad for his patience and great help in last stage compilation of my PhD thesis latex files on snoopy, when I was unable to connect with snoopy machine from LIMATB–UBS, France. Working with DiekA software on Unix machines would simply not be possible without Nico van Vliet and Herman van

Corbach and their support is greatly acknowledged. I owe lots of thanks to Harm Wisselink for his enthusiasm, patience in helping me number of times whenever I just didn't understand something in DiekA. I have enjoyed sharing my office space with Maarten van Riel, Ashraf Hadoush, Johan Hol and Jan Harmen Wiebenga. It was a highly motivating environment, with a group of extremely smart people around.

I would like to express my gratitude to Prof. Leo Kestens, Prof. Jilt Sietsma, Alexis Miroux and Manojit Ghosh, who were my academic partners in the project at the Technical University Delft for performing their part of work. I am very sure that the thesis would not be in this final shape without the great contribution of Alexis Miroux and Manojit Ghosh for the physically based materials, microstructral studies and mechanical experiments. Bjørn Holmedal from NTNU, Norway is greatly acknowledged for providing the computer codes of the Nes model.

I would like to express my gratitude to the members of my promotion committee for taking time to read my dissertation and for assessing the manuscript.

Special thanks to the industrial partners that have been involved in the research project. I would like to acknowledge the Response Group of industrial partners for the discussions, meetings, input and their support: Ruth van de Moesdijk, Tony Chezan, Yuguo An and Jenny Loiseaux (Corus RD&T), Pieter Jan Bolt and Robert Werkhoven (TNO), E. Straatsma and C. van Tilborgh (Fokker Aerostructures), and L. 't Hoen–Velterop (NLR). Robert Werkhoven from TNO performed the cylindrical cup warm deep drawing experiments. The warm deep drawing of the square cup, equi-biaxial yield data and the material data were determined by Corus RD&T.

I should not forget to mention the nice working environment that the M2i, former NIMR provided: the courses on presentation skills, personal development and career counseling and the social events made it a great company to work for. I am greatly indebted to Tanja Gerrits and Debbie Vrieze-Zimmerman van Woesik for helping me with numerous administrative and other personal questions during my stay at the University of Twente, Enschede.

I would like to acknowledge Han Huétink, Ton van den Boogaard and Muhammad Niazi for carefully reading the thesis and helping me to improve its contents considerably. In adition, the efforts of Vivien Cook to correct the English language and my office roommate Johan Hol for the Dutch translation of the Summary are greatly acknowledged.

Apart from the scientific work, I have had a very pleasant social life in Enschede due to all desi friends. Vijaya Ambati is the first Indian, I contacted him even before coming to interview for this PhD position, and I am fortunate to have met a person like him. I appriciate his kind and constant support all through these years, in particular during the stressful days of my stay in the Netherlands. I broaden my warm gratitude to my friends who made the past four years memorable ones. It is a great pleasure to thank all my Indian friends: Kittu, Vijaya-Sangeeta, Ram-Veda (little Druv babu), Chandra-Meenakshi, Srikanth-Punya, Pramod-Visakha (little Vibhor), Vijay-Ranjini, Shodan-Chaitanya, Pandu-Pallavi, Digvijay-Aba, Kishore-Hema, Giri-Varsha, Srikumar-Sowjanya, Jitendra-Neelam (cute Bhiravi), Tariq-Sehar, Hrudya, Srivatsa and many other Indian friends.

And now it is time to thank the most important people in my life, three generations that supported me in different ways. I am very thankful to my parents for their continuous and endless support, inspiration and motivation. My little angel Puji, although now, when I write this, you are still too young to understand what your father did, one day you will.

The research did not get more difficult with you around, maybe in a way it just got easier. Bujjamma (Lakshmi), yes we did it, the work is done and I emphasize that WE did it, thank you for the support during those hard times and you make me enjoy life with your sweet caring and unconditional love.

Nomenclature

Roman symbols

$\mathbf{B}$	left Cauchy-Green deformation tensor
B	static recovery kinetics parameter
B_ρ	pre-exponential parameter used in dynamic recovery of dislocations in cell interior
B_δ	pre-exponential parameter related to dynamic recovery with subgrain growth
$\mathbf{b}$	body force vector
b	magnitude of the Burgers vector
$\mathbf{C}$	right Cauchy-Green deformation tensor
C	dislocation storage parameter
c	Mg solute concentration factor
c_0	concentration other solute atoms other than Mg
c_{sc}	solute concentration at the dislocation core
$\mathbf{D}$	rate of deformation
D	average grain size
$\mathbf{d}$	material displacement vector
$\mathbf{E}$	Green-Lagrange strain tensor
$\mathbf{e}$	Euler-Almansi strain tensor
$\mathbf{F}$	deformation gradient
f	volume fraction of cell walls during stage II hardening
f_{r}	volume fraction of particles

G	shear modulus
k	Boltzmann's constant ($1.3807 \cdot 10^{-23}$ J/K)
l_a	activation length used in the expression of dynamic recovery
L_D	slip length due to grain size
L_ρ	slip length due to dislocations
L_eff	effective slip length
L_p	slip length due to particles
M	Taylor orientation factor
n	bulk diffusion coefficient in overageing model
$\mathbf{q}$	heat flux vector
q	static recovery kinetics parameter
q_b	scaling parameter between ρ_i and ρ_w in stage II
q_c	scaling parameter between ρ_i and δ in stage II
$\mathbf{R}$	rotation tensor
$\mathbf{R}_\mathrm{m}$	material rotation tensor
R	universal gas constant (8.3144 J/(mol K))
R_θ	Lankford R value, ratio between width and thickness strain
r	average radius of particles
T	temperature
$\mathbf{U}$	right stretch tensor
U_s	activation energy for diffusion of atoms in solution
U_sd	activation energy for self diffusion
$\mathbf{u}$	degrees of freedom vector in a discretized system
V_t	activation volume
$\mathbf{v}$	material velocity vector
$\mathbf{w}$, w	weighting functions

Greek symbols

α_1	constant, related to dislocation spacing
α_2	constant, related to boundary spacing
δ	subgrain size
ΔU_s	activation energy between solutes and dislocations
ΔU_sc	activation energy for diffusion of Mg solute atoms in aluminum
$\dot{\boldsymbol{\varepsilon}}^\mathrm{p}$	plastic strain rate tensor
$\varepsilon_\mathrm{eq}^\mathrm{p}$	equivalent plastic strain
γ	(resolved) shear strain
$\Gamma_{1,2}$	statistical distributions of subgrain sizes
Γ	boundary of analysis domain
κ_2	grain boundary shape factor
κ_3	particle shape factor
ν_D	Debye frequency
Ω	analysis domain
Ω	recovery parameter in Bergström model
φ	misorientation angle in Nes model
ρ	total dislocation density
ρ_0	dislocation density prior to deformation
ρ	mass density
ρ_d	dislocation density of deformed configuration
ρ_i	interior dislocation density
ρ_m	mobile dislocation density
ρ_w	cell wall dislocation density
$\boldsymbol{\sigma}$	Cauchy stress tensor
σ_eq	equivalent stress
σ_f	flow stress
τ	(resolved) shear stress
τ_a	athermal stress

τ_{cl} solute clustering stress

τ_{d} stress due to stored dislocations

τ_{p} stress due to non-shearable particles

τ_{t} thermal stress

ϕ yield function

ξ_{δ} stress intensity factor related to dynamic recovery with subgrain growth

ξ_{ρ} stress intensity factor related to dynamic recovery inside the cell

General subscripts and superscripts

$(.)_{1,2,3}$ principal values

$(.)_{bi}$ equi-biaxial

$(.)^{e}$ elastic part

$(.)^{p}$ plastic part

$(.)_{ps}$ plane strain

$(.)_{sh}$ pure shear

$(.)_{un}$ uniaxial

Abbreviations

b.c.c. body centred cubic

DSA dynamic strain ageing

f.c.c. face centred cubic

GP Guinier Preston zone

ND normal direction

RD rolling direction

SSSS supersaturated solid solution

TD transverse direction

1. Introduction

1.1 Sustainability and the use of Aluminum in Transport Sector

"Light-weighting is a key measure to improve the sustainability of transportation". The transportation sector is responsible for nearly 20% of man-made greenhouse gas emissions (Helms *et al.*, 2005). In 2000, around 7.6 billion tons of CO_2 equivalent were emitted through the use of transport vehicles. It is often believed that the next generation vehicles must run on alternative and clean fuels *e.g.* hydrogen *via* fuel cells to avoid further increase of harmful emissions. This approach appears to be more of a solution that may be feasible and practical in the long-term. A short-term approach would be the realization of low mass vehicles. The prime objective of lightweight construction design concepts is to minimize the dead weight of a construction without disrupting its function, safety or useful life. The reduction in the mass of vehicles can significantly improve fuel efficiency, reducing energy consumption and greenhouse gas emissions. It is estimated that a 10% reduction in vehicle weight improves the fuel effciency by 5.5% (Miller *et al.*, 2000). Exhaust emissions will be proportionally lower. As a general indicator, 1 kg of automotive aluminum substituted for a heavier material in a vehicle typically avoids 20 kg of greenhouse gas emissions during its operating life (According to International Aluminum Institute).

Examples of sheet metal materials showing the relevant lightweight construction potential and appropriate for use in vehicle construction are aluminum, magnesium and high-strength steels and in addition titanium alloys.

It must be accepted, however, that these materials are often associated with limited formability, with the result that the production of large, complex sheet metal components using forming technology is either impossible or is only possible in combination with increased costs, compared to mild steel. It should also be noted that processing high strength materials such as high strength steel requires correspondingly high processing forces and pressures. This has direct consequences for the design of the plant and equipment and the forming tools. Besides, high elastic deformation levels compromise the dimensional stability of the components after forming (Neugebauer *et al.*, 2006). Magnesium sheet is also a good candidate to achieve weight reduction, but the formability is considered less than aluminum and titanium alloys are too expensive for most applications.

Aluminum is an ideal material for transport applications, because of its high strength to weight ratio, corrosion resistance, weldability and very good thermal and electrical conductivity. It also plays an important role in reducing CO_2 emissions in transportation helping to improve the sustainability of the transport industry. Aluminum not only offers significant advantages during the use stage of an automobile, but in particular, also in the end-of-life

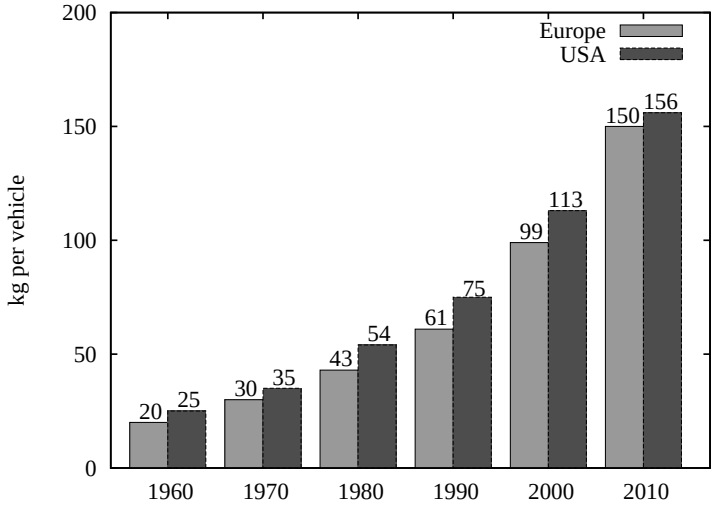

Figure 1.1: Average use of aluminum over years.

stage. The infinite recyclability of aluminum, together with its high scrap value and the low energy needs during recycling make aluminum lightweight solutions in automotive applications highly desirable (Mildenberger and Khare, 2000; Martchek, 2006).

Aluminum has historically been employed in automobiles primarily in the form of castings *e.g.* for engine blocks, transmission housings and wheel rims. In recent years automotive manufacturers are making good use of the wide variety of aluminum products such as the extruded aluminum tubes in space frame structures and aluminum sheet for inner and outer panels. Weight reductions of 50 % for the 'body in white' have been achieved by the substitution of steel by aluminum (Carle and Blount, 1999; Miller *et al.*, 2000).

Figure 1.1 illustrates the usage of aluminum for European and American vehicles over years (Toros *et al.*, 2008). As shown in Figure 1.1, the amount of aluminum used in 1960 is substantially low. Despite the obvious advantages of the high strength to weight ratio and corrosion resistance of aluminum alloys, they have a distinguishable downside in that their formability is considerably lower than traditional steel alloys at room temperature conditions. It is usually caused by the high alloy percentages that are required for high strength (Novotny and Geiger, 2003). To enlarge the application of aluminum sheet in many industrial forming processes, the mechanical loading is combined with thermal component *e.g.* deformation at elevated temperature or intermediate annealing between deformation steps. The numerical simulation of such processes is the subject of this thesis.

1.2 Formability of Aluminum Sheet

Most commonly used sheet metal forming processes are bending, deep drawing, and stretching. To fabricate a doubly curved product from a sheet material, the deep drawing or the stretching process is widely used. The deep drawing process can reach production cycles

of less than 10 s, and is thus a suitable process for mass production. In deep drawing and stretching, the stresses normal to the sheet are generally very small compared to the in-plane stresses and are therefore neglected. Hence, a biaxial stress state is considered.

The formability of aluminum sheet is, under room temperature conditions, lower than for a typical deep drawing steel grade. For example, the formability of aluminum alloys is only about two-thirds of a mild steel, their Young's modulus is about one-third of steel, which in turn causes higher vulnerability of wrinkling and springback (Bolt *et al.*, 2001), and their elongation is about half of steel's (Li and Ghosh, 2003). The inferior formability of aluminum alloys makes it more difficult and expensive to use them in mass production of structural and body parts, which means that the maximum attainable strain in one process step is less than that for mild steel along the same strain path (Van den Boogaard, 2002). To improve the formability of an aluminum sheet in many industrial forming processes, the mechanical loading is combined with thermal component. A particular example is warm forming, *i.e.* utilization of the increased formability of aluminum at elevated temperatures up to the recrystallization temperature. In this process, parts of the tools are heated and other parts are cooled which make it possible to manipulate local flow behavior, in order to increase the formability (Shehata *et al.*, 1978; Bolt *et al.*, 2001; Neugebauer *et al.*, 2006). Another example from aerospace industry is stretch forming of aluminum parts in a number of stages with intermediate annealing steps and a final solution heat treatment, quenching and ageing.

1.2.1 Forming at Elevated Temperature

In the automotive industry, two most widely used aluminum alloys are Al–Mg alloy and Al–Mg–Si alloys. Al–Mg (5xxx series) alloys exhibit relatively good formability in annealed condition, however, they suffer from the problem of dynamic strain ageing effects resulting in stretcher lines, which affect the surface quality. In automotive applications, therefore, these alloys are mostly used in fabricating inner panels. Also they are not heat treatable and can only be hardened by mechanical working. On the other hand, 6xxx alloys are heat treatable and free of Lüdering. This is because of the fact that it contains low Mg compared to 5xxx series. Typically, 6xxx alloys are used for fabricating outer panels because of absence of stretcher lines.

The mechanical properties of aluminum alloys can be influenced by varying temperature, *i.e.* use the temperature strategically as a process parameter during a forming operation. Finch *et al.* (1946) started the investigation with both rectangular and circular cups from annealed and hardened aluminum sheet alloys as early as 1946. Their results showed significant improvement in the drawability at a relatively moderate temperature of about 150 °C even for the precipitation hardened alloys (like 2024-T4 and 7075-T6). Shehata *et al.* (1978) studied the combined effect of temperature and strain rate on punch velocity. They concluded that the cup height increased with increasing forming temperature and/or decreasing punch speed for an Al–Mg alloy. Extending the same experiment to 5182-O, Ayres and Wenner (1979) have drawn the same conclusions about temperature and forming speed. After some publications in the 1970s and 1980s by Shehata *et al.* (1978); Wilson (1988), the research accelerated in the last decade (Naka and Yoshida, 1999; Bolt *et al.*, 2000, 2001; Moon *et al.*, 2001). Extensive review on warm forming of aluminum alloys

was given by Toros *et al.* (2008). It was demonstrated that the formability improves by a uniform temperature increase, but the best results are obtained by the selective and localized heating strategies on the forming dies, causing an inhomogeneous temperature distribution on the blank. In deep drawing experiments with AA 5754-O, the limiting drawing ratio could be increased from 2.1 to 2.6 by heating the flange up to 250 °C and by cooling the punch to room temperature (Van den Boogaard *et al.*, 2001). This leads to an increase in maximum attainable cup height by 70 %. An extra benefit of warm forming is that the stretcher lines that develop when Al–Mg alloys are deformed at room temperature do not appear at elevated temperatures.

1.2.2 Stretch Forming with Intermediate Heat Treatments

Stretch forming is a method that combines controlled tension and bending of sheet material around dies to produce accurately contoured parts. It is extensively used in the aerospace industry to form large sheet panels of mild curvature, *e.g.* the leading edge of a wing (Chancerelle, 2002). A commonly used material for aircraft skins is the heat-treatable aluminum alloy AA 2024. Possible failure modes during forming of this material are necking , wrinkling, Lüders lines or orange peel. In order to avoid these failures and still achieve large deformations it is often necessary to use expensive intermediate heat treatments, especially for complex shapes (Wisselink and van den Boogaard, 2005). An important topic in industry is the production of good parts for minimal costs. Therefore the main factors in the cost price, *e.g.* the amount of material and the number of heat treatments needed during forming, have to be minimized for an optimal process.

1.3 Objective of this Thesis

Controlling the temperature distribution in sheet metal parts can improve the formability of aluminum. However, the temperature distribution brings in an extra degree of freedom in the production process for which experience is lacking. A good simulation tool will reduce the trial-and-error process that would be necessary to optimize the process conditions. Similarly, in the stretch forming of aircraft skin parts with intermediate heat treatments, the heating and cooling cycles are time consuming and should therefore be minimized. The current practice is that a maximum amount of strain increment per deformation step is allowed. This does not take the changing material behavior into account, as can be done within a finite element analysis, assuming that a proper material is available. A reduction of the number of deformation stages would be very beneficial. The objective of the thesis is to show how these thermally assisted forming processes of aluminum sheet can be simulated. The resulting simulation models should be able to predict the manufacturability of a product for the two forming processes under consideration: warm forming and cold forming with intermediate annealing.

A simulation of these processes necessitates the use of a set of advanced thermo-mechanical material models. The models should describe the relation between strain, strain rate, temperature and stress by considering the effect of solutes and precipitates on strain hardening at room temperature, the interaction of static recovery and precipitation and the effect of concurrent precipitation on work hardening during warm forming together with the

effect of dynamic recovery. These physical mechanisms will be modeled up to a level that is required for macroscopic process simulations. Material models based on the underlying physical processes are expected to have a large range of applicability in this respect as they describe the material behavior over a large range of strains, strain rates and temperatures.

In broad outline, warm forming tensile and deep drawing experiments, and modeling of material behavior and its application to warm forming process is discussed in the first part of this thesis. The material models and their application to stretch forming processes is the subject of the remaining part.

1.4 Outline

The general outline of the thesis is as follows. In Chapter 2 the experimental observations on Al–Mg–Si alloys are described, including uniaxial tensile tests at different temperatures and strain rates, and biaxial tests at room temperature. Furthermore, the procedure and the results of warm cylindrical cup deep drawing experiments are presented, which includes the effect of various parameters on warm forming processes, such as the effect of punch velocity, holding time, temper and temperature on the punch force–displacement response. The plastic anisotropy of the material which can be directly reflected by the earing behavior of the drawn cups has also been studied.

Several material models for warm forming of aluminum sheet are discussed in Chapter 3. Firstly, the constitutive framework of plasticity is introduced. To describe the multiaxial and anisotropic behavior of the aluminum sheet material, two advanced yield functions are considered. To model the temperature and strain rate dependent work hardening, phyiscally based hardening models by Bergström (1983) and Nes (1998) are used. Finally, the predictive power of different work hardening models are compared with the uniaxial tensile tests on 5754-O alloy used as a representative example of aluminum alloys.

Chapter 4 concerns the application of warm forming. First, a uniaxial tensile test is simulated, including the non-uniform part of the clamping area. It is investigated whether simulations for strains beyond the uniform strain yield realistic predictions. In the second application, simulation of warm cylindrical cup deep drawing are considered. The results are extensively compared with experimentally obtained punch force–displacement curves and thickness distributions of different aluminum alloys (AA 5754-O, AA 6016, AA 6061 with different tempering conditions T4 and T6). Finally, the material models are further verified by simulating the warm deep drawing of square cup, as it experiences a more complex deformation path than the cylindrical cup deep drawing.

Chapter 5 is about stretch forming of aircraft skin parts with intermediate annealing steps. Finally, Chapter 6 summarizes the conclusions from this research and directions for future work are given.

2. Warm Forming Experiments

Mechanical experiments are used to establish the material properties that are required for engineering applications of the material. The aim of this chapter is first to investigate the mechanical behavior of aluminum sheet at temperatures up to 250 °C, since under these conditions the temperature and strain rate dependency vary considerably. Based on the experimental observations, appropriate material models and their parameter identification should be deduced. In order to validate these material models, typical warm cylindrical cup deep drawing experiments are used.

In this work, three different aluminum alloys were used to validate the physically based material models, that will be elaborated in Chapter 3. The non-heat treatable Al–Mg alloy 5754-O and two heat treatable Al–Mg–Si alloys AA 6016 and AA 6061 are considered. It is noted that the experimental results of 5754-O alloy were taken from the pioneering work of Van den Boogaard (2002) and further description of these experiments is not given in this thesis.

Firstly, basic work hardening mechanisms in aluminum alloys are introduced. In Section 2.2, some characteristics of the materials AA 6016 and AA 6061 are presented. The procedure of uniaxial tensile tests and their results are described in Section 2.3, which includes the temperature and strain rate effects on work hardening along with the effect of precipitates on mechanical response. The room temperature biaxial tests used to describe the shape of the yield locus are presented in Section 2.4. Warm cylindrical cup deep drawing experiments are described in Section 2.5. The experimental deep drawing results are used to validate the material models in Chapter 4.

2.1 Work Hardening in Aluminum Alloys

Work hardening is an important phenomenon that takes place during plastic deformation behavior of polycrystalline materials (Hull, 1965; Courtney, 1990). Important issues in plastic deformation like plastic flow localization and fracture are strongly influenced by work hardening properties. A better understanding and characterization of work hardening is required to deduce a suitable work hardening model to represent a good match with experimental stress–strain relations. The main ingredients responsible for work hardening are dislocations. Dislocations interact with each other by generating stress fields in the material. The interaction between the stress fields of dislocations can impede dislocation motion by repulsive or attractive interactions. Additionally, if two dislocations cross, dislocation line entanglement occurs, causing the formation of a jog which opposes dislocation motion. These entanglements and jogs act as pinning points, which oppose dislocation motion.

The work hardening is also influenced by the grain boundaries, where the grain boundaries act as pinning points impeding further dislocation propagation. The number of dislocations within a grain also have an effect on how easily dislocations can traverse grain boundaries and travel from grain to grain. Thus, by changing grain size one can influence dislocation movement and yield strength.

The work hardening in *non-heat treatable alloys* such as in Al–Mg alloys, is further increased by the presence of solute atoms in solid solution. In solid solution hardening, solute atoms such as Mg, Mn and Cu are added to base material aluminum, resulting in either substitutional or interstitial point defects in the crystal. The solute atoms cause lattice distortions that impede dislocation motion, increasing the yield stress of the material. Solute atoms have stress fields around them which can interact with those of dislocations. The presence of solute atoms impart compressive or tensile stresses to the lattice, depending on solute size, which interfere with nearby dislocations, causing the solute atoms to act as potential barriers to dislocation propagation and/or multiplication. Increasing the concentration of the solute atoms will increase the yield strength of a material; however, there is a limit to the amount of solute that can be added, and one should look at the phase diagram for the material and the alloy to make sure that a second phase is not created. Solutes also introduce other effects such as dynamic strain ageing resulting in serrated flow stress in Al–Mg alloys.

The work hardening in *heat treatable alloys* such as in Al–Mg–Si alloys, is further influenced by the formation of extremely small uniformly dispersed second phase particles within the original phase matrix in a process known as "Precipitation (or Age) Hardening". The precipitate particles act as obstacles to dislocation movement and thereby strengthen the heat treatable alloys. Precipitation hardening involves raising the temperature of the alloy into the single phase region so that all of the precipitates dissolve. The alloy is then rapidly quenched to form a supersaturated solid solution (SSSS) and to trap excess vacancies and dislocation loops which can later act as nucleation sites for precipitation. The precipitates can form slowly at room temperature (natural ageing) and more quickly at slightly elevated temperatures, typically 100 °C to 200 °C (artificial ageing).

In Al–Mg–Si alloy system, precipitation occurs through a sequence of different phases. According to Dutta and Allen (1991) and Edwards *et al.* (1998), the precipitation sequence in Al–Mg–Si alloys is:

$$\textit{clusters of Si atoms} \longrightarrow \textit{GP-I zones} \longrightarrow \textit{GP-II zones}/\beta'' \longrightarrow \beta' \longrightarrow \beta \mathrm{Mg_2Si}$$

Owing to the higher solubility of Mg in Al, Si comes out of the solution and form clusters when stored at room temperature. Further storing or heating cause diffusion of Mg and formation of Mg–Si natural ageing cluster (NA). The first phase to precipitate on the small clusters is called GP (Guinier-Preston) zones. Formation of GP zones occurs by quench-in vacancies. According to Edwards *et al.* (1998), GP zones exist in two different phases, namely GP-I and GP-II or alternatively β''. Fully coherent spherical GP-I ranges 1–3 nm in size. Partially coherent GP-II appears as needles having $4 \times 4 \times 50$ nm^3 in size. The next phase in the transformation sequence is β'. It has a lower Mg/Si ratio than β. Aluminum alloys containing magnesium and silicon as the major solutes get strengthened by precipitation of metastable precursors (β'') of the equilibrium $\beta \mathrm{Mg_2Si}$. An excess Si (Mg:Si$<$ 1) like in 6016 is reported to enhance the age hardening response by increasing the density of β'' metastable precipitates (Edwards *et al.*, 1998). It also reduces the Mg:Si

ratio in early GP zones and co-clusters. For a Cu containing alloys like AA 6061, Cu is found to increase the kinetics of precipitation during artificial ageing. It also reduces the deterioration of age hardening response arising from natural ageing of Al–Mg–Si alloys. The determination of the ageing sequence for such alloys is complicated by the presence of more than one co-existing phase for the same heat treatment stage (Zandbergen *et al.*, 1997; Andersen *et al.*, 1998). According to Andersen *et al.* (1998), Cu addition increases the level of super saturation of Mg and Si by forming clusters during natural ageing. The extra precipitation of β'' has been identified apart from GP-I zones for the same ageing conditions with Cu rich alloys which is absent for Cu lean alloys. Laughlin *et al.* (1998) reported that the Cu level has a large effect on the age hardening kinetics in the underaged region and a smaller but noticeable effect on the value of the peak hardness. The microstructure of the alloy with a higher Cu content is much finer than that with a lower Cu content. The degree of hardening obtained depends on the size, number and relative strength of the precipitates. These factors are determined by the composition of the alloy and by the tempering temperature and tempering time.

Based on the above discussion, two alloys are selected purposefully in the present investigation, namely: AA 6016 and AA 6061. Alloy 6016 is a Si excess alloy (Mg/Si=0.4 in wt.%), while alloy 6061 is almost balanced (Mg/Si=1.5 in wt.%). It is aimed to generate a unified work hardening model irrespective of alloy conditions, temperature and strain rate. The effect of change in precipitate states should be a part of the work hardening model.

2.2 Material Characteristics

In this section the materials AA 6016 and AA 6061 used in the experiments are characterized. The mechanical behavior of an alloy is mainly determined by its chemical composition, grain size, texture and microstructure.

2.2.1 Composition, Microstructure, Texture

The chemical composition of the alloys was given by the manufacturer and is presented in Table 2.1. The materials were cold rolled, solution treated and naturally aged (T4). The final thickness of AA 6016 was 1.01 mm and AA 6061 was 1.2 mm. Alloy 6016 is a Si excess alloy (Mg/Si=0.4 in wt.%) while alloy 6061 is almost balanced (Mg/Si=1.5). Another noticeable difference between the two alloys is the higher Cu content of alloy 6061. Naturally aged (T4) has been made to peak aged condition (T6) by applying a heat treatment at 150 °C for four hours followed by 170 °C for four hours in salt bath and quenched in water.

In Figure 2.1(a), the OIM (Orientation Imaging Microscopy) measured from EBSD for AA 6016-T4 alloy is presented. It is clear that the as-received material is fully recrystallized owing to uniform crystallographic orientation inside each grain. All the as-received materials show similar recrystallized microstructures. Also the comparison of OIM from AA 6016-T4 and AA 6016-T6 materials in Figure 2.1, confirms that heat treatment did not bring any change in grain shape and size meaning that grain coarsening was prevented by precipitates on grain boundaries. In both tempering conditions the grains are flat ellipsoids.

Table 2.1: Chemical composition (wt%) of the investigated alloys.

Alloy	%Si	%Fe	%Cu	%Mn	%Mg	%Cr	%Other	%Al
AA 6016	1.03	0.25	0.06	0.15	0.42	0.02	<0.15	rem.
AA 6061	0.62	0.35	0.20	0.08	0.95	0.15	<0.15	rem.

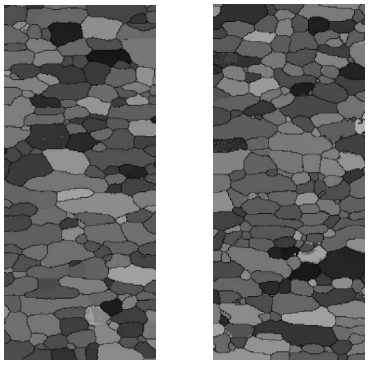

(a) AA 6016-T4 (b) AA 6016-T6

Figure 2.1: OIM measured from EBSD of as-received materials.

The observations on AA 6061 material are very much similar to the results obtained on AA 6016 material.

Texture of the as-received materials was determined at the surface, sub-surface (15% of the thickness) and at mid-plane of the sheet using X-ray diffraction technique. It is noticed that texture components do not vary a lot through the thickness direction. This remains true for all other investigated alloys. The materials have cube texture and an average grain size (equivalent circular diameter) of 17 μm to 25 μm.

2.3 Uniaxial Tensile Tests

Uniaxial tensile tests are the most common among all mechanical tests because of their easy control over the test parameters. The uniaxial test results are typically important in estimating various parameters that influence formability such as work hardening, anisotropy etc. In this section, the procedure and results of uniaxial tensile tests are presented. In the present research, tensile tests were carried out on the thermo-mechanical simulator Gleeble 3800. The dimensions of the tensile test specimen are presented in Figure 2.2.

An extensometer was attached at the middle of the sample and the process is gauge controlled so the measurement of the deformation was restricted within the two arms of

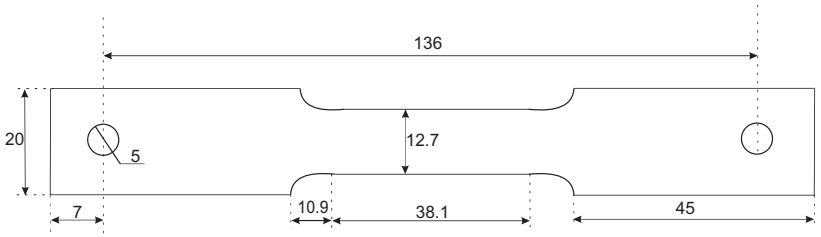

Figure 2.2: Geometry of the tensile test specimen (dimensions in mm).

the extensometer. The distance between the two arms of the extensometer was 10 mm, each maintaining 5 mm distance from the center of the specimen. Initially, the samples were preloaded with a stress of 0.5 MPa. Then the specimens were heated by means of the Joule effect and the clamps were cooled down with a circulating water system, consequently a temperature difference forms during heating. The maximum temperature difference of 4 °C was observed in the gauge length, which is reasonable for this kind of test. After deformation the specimens were cooled by compressed air and unloaded. For the tests performed at room temperature, the same sequence has been maintained without heating and cooling by compressed air. From the load–deformation curve so generated the true stress–true strain response of the materials was calculated.

Uniaxial tensile tests were performed at temperatures of 25 °C, 150 °C and 250 °C at strain rates of 0.01 and 0.1 s^{-1}. Few tests were performed at an extremely slow strain rate of 0.001 s^{-1} and the effect of holding time was also investigated at 250 °C for T4 material with different holding times of 2 , 30 and 60 s in order to observe presence of any dynamic precipitation. The tensile tests on naturally aged material (T4) were done approximately one year after their production to have a guarantee of complete natural ageing. For every combination of temperature and strain rate, 2 to 4 tests were performed, in some cases with more than one year interval. The reproducibility of the tests was confirmed through the average scatter of true stress being less than ± 1 MPa for the same value of true strain.

For every combination of temperature and strain rate at different tempering conditions, one representative stress–strain curve for AA 6016 alloy and for AA 6061 alloy is shown in Figure 2.3. Figure 2.3, also illustrates the effect of temper for both the alloys at two strain rates. T6 material is stronger compared to T4 for both alloys at any strain rate, although the rate of work hardening is higher for T4 state at all temperatures. The difference in rate of hardening is very small at room temperature while at 250 °C there is practically no work-hardening effect in T6 state, appearing like a plateau before it starts necking.

It can also be observed from Figure 2.3 that the strain rate sensitivity increases with increasing temperature. At 25 °C, almost no effect of strain rate is shown on the work hardening behavior. At higher temperatures, due to the dynamic recovery of dislocations, the flow stress increases with increasing strain rate. This increasing flow stress with increase of strain rate is more clearly visible for T6 condition at 250 °C. However, in Figure 2.3(a) and Figure 2.3(c), at 250 °C the lowest strain rate of 0.001s^{-1} yields the highest flow stress. It is mainly due to more time for dynamic precipitation at the slowest strain rate.

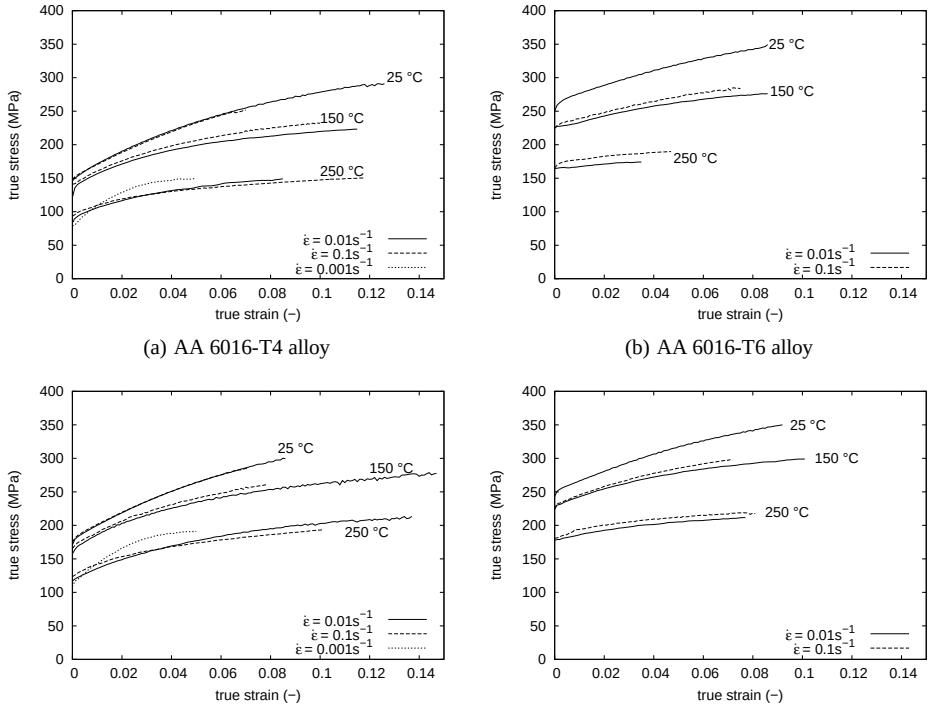

(a) AA 6016-T4 alloy

(b) AA 6016-T6 alloy

(c) AA 6061-T4 alloy

(d) AA 6061-T6 alloy

Figure 2.3: Temperature and strain rate influence on true stress–strain curves for different tempering conditions of AA 6061 alloy.

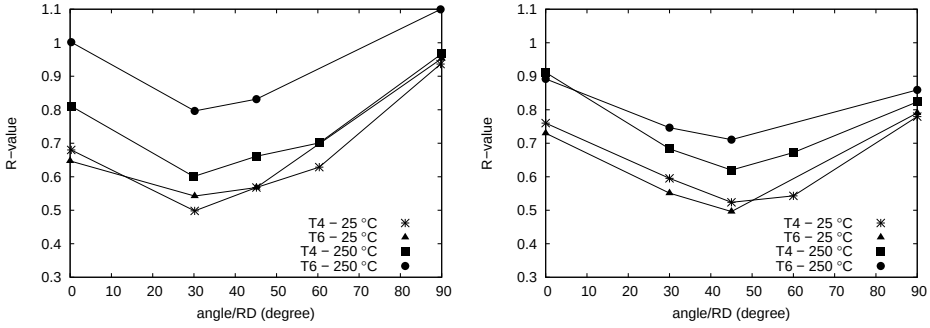

(a) AA 6016 alloy

(b) AA 6061 alloy

Figure 2.4: Effect of temper on R-value.

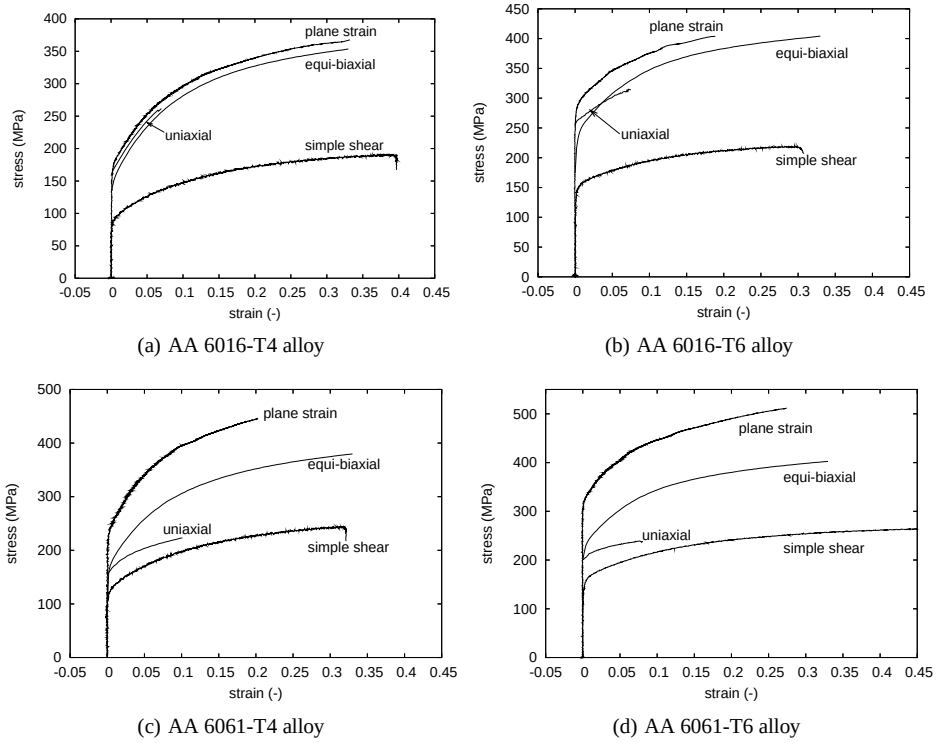

(a) AA 6016-T4 alloy

(b) AA 6016-T6 alloy

(c) AA 6061-T4 alloy

(d) AA 6061-T6 alloy

Figure 2.5: Stress–strain curves for different types of loading at room temperature.

The R values measured at 10% elongation for different tempering conditions and at different temperatures are shown in Figure 2.4. In the case of 6016, R-value is lowest at 30° and for AA 6061, it is at 45° irrespective of temperature and temper condition. For both alloys there is negligible difference in R values between T4 and T6 at room temperature while a much improved R value profile can be noticed for T6 state compared to T4 at 250 °C. This difference is more pronounced for AA 6016.

2.4 Biaxial Tests

The tests presented in Section 2.3 considered the hardening in uniaxial stress state, at several temperatures and strain rates for different tempering conditions and for different alloys. Usually in sheet forming processes, the stress state is biaxial and an infinite number of stress states can be defined by means of an infinite number of strain paths to reach such a stress state. However, the material behavior in multiaxial stress states can be experimentally quantified by a limited number of stress or strain states.

In addition to the uniaxial tests, normal compression tests, plane strain tests and simple shear tests were performed. The normal compression test is equivalent to an equi-biaxial

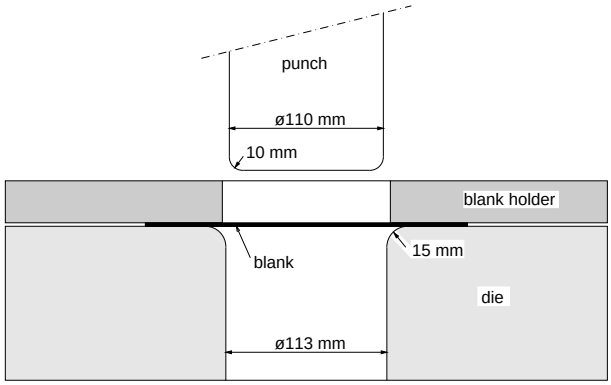

Figure 2.6: Dimensions of the tools for cylindrical cup deep drawing.

tensile test, assuming that the plastic deformation is independent of the hydrostatic stress (Vegter *et al.*, 2003). A stack of sheet specimens was prepared with nominal dimensions of $10 \times 10 \times 10\,\mathrm{mm}^3$. The stack is loaded in the normal direction, and lubricated with oiled PTFE film. The tests were carried out in a MTS hydraulic testing machine and the displacement along both in-plane directions is measured using a cross extensometer.

The plane strain tension and simple shear tests were performed using the *Twente biaxial tester*, described by Pijlman (2001) and Van Riel (2009). In this loading frame a sheet area of $45 \times 3\,\mathrm{mm}^2$ can be deformed in plane strain tension, simple shear or any combination simultaneously and with a possible thickness between 0.7 mm and 2.5 mm. Because, the height of the deformation area is small compared to the thickness the simple shear loading can be applied without material buckling. Also due to the high length-to-width ratio of the deformation region a plane strain condition at the central region of the deformation area is imposed. However, the edges of the deformation area are free and the deformation state will tend to the uniaxial stress state and this edge effect needs to be taken into account. The strains for the plane strain and simple shear experiments are determined by recording the displacements of 16 dots on the deformation region of the specimen and subsequent image processing. With these two equipments, no elevated temperature tests can be executed.

Plane strain tension tests were performed with the loading direction perpendicular to the rolling direction and at 45° to the rolling direction. Simple shear tests were performed with the shear direction at $-45°$, 90° and 45° to the rolling direction. For each direction two samples were tested. The stress–strain curves are presented in Figure 2.5 together with one uniaxial curve for comparison for two different alloys at two different tempering conditions. For the uniaxial, plane strain and equi-biaxial tests, the true stress and strain in the loading direction are presented. For the simple shear test, the shear stress and the shear angle γ are used. These biaxial tests are used to describe the shape of the anisotropic yield loci described in Chapter 3.

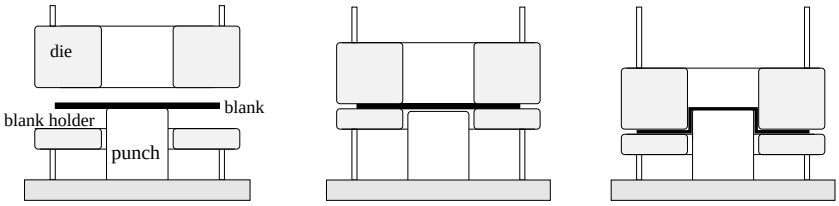

(a) Positioning (b) Holding (c) Drawing

Figure 2.7: Schematic deep drawing operation.

2.5 Cylindrical Cup Deep Drawing

Deep drawing is one of the most widely used processes for forming sheet metal parts in the automotive industry. It is also a popular process in assessment of formability of sheet metals. In this section, experiments of warm cylindrical cup deep drawing are presented. The objective of these deep drawing tests are to obtain the force–displacement curves during the deep drawing process. After the experiments, the cups were removed and the thickness distribution from the center to the outer diameter in the rolling and transverse direction was measured. Also the earing[1] profile was measured in order to assess the effect of sheet anisotropy in forming operations. Experimental drawing test data is used to validate the modeling approach presented in Chapter 4.

The drawing tests were performed for both AA 6016 and AA 6061 alloys of T4 and T6 tempers. Experiments were performed with a tool set of which the dimensions are given in Figure 2.6. All the experiments were performed on blanks of 220 mm diameter that were taken from the same batch of which the uniaxial and biaxial tests were performed. In the experiments, the effective punch stroke was 65 mm and punch velocities of 13 mm/min to 80 mm/min were used. The die and the blank holder were given a temperature of 25 °C, 180 °C and 250 °C, while the punch was kept at 25 °C. Room temperature drawing tests were done with the blank holding force equal to 90 kN and warm deep drawing tests were done with 54 kN blank holding force.

2.5.1 Experimental Procedure

Experiments were performed with a tool set schematically presented in Figure 2.7. The blanks were placed on top of cold punch which was slightly extended vertically from the blank holder as shown in Figure 2.7(a). The blanks were lubricated with a water-based paste that contained MoS_2. The paste was applied on both sides of the blank before being placed on top of the punch. For drawing at warm temperature, the die and the blank holder were

[1] Plastic anisotropy during deep drawing may entail the formation of uneven rims of the drawn product, usually referred to as earing. One important consequence of that is—besides the irregular shape of the drawn specimen—an inhomogeneous distribution of the mechanical properties and of the wall thickness due to volume conservation.

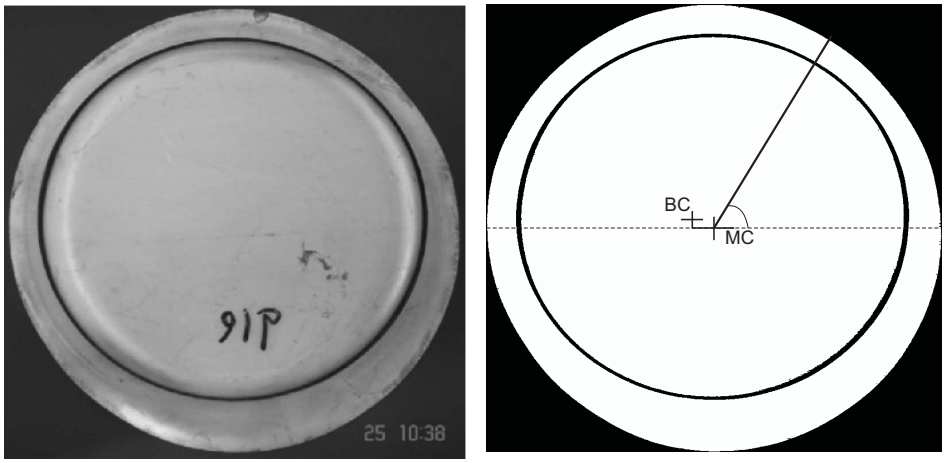

(a) Digital image (b) Binary image

Figure 2.8: Earing profile measurement.

heated with internal heating rods and the punch was cooled with water through internal water circulating channels. Thermocouples were used to measure the temperatures of punch and the die. During the heating process, water of the lubricant evaporates leaving the lubricant on the blank, which still gave sufficient lubrication at 250 °C. The blank was heated up and reached the desired temperature soon after it came into contact with the die and blank holder. This is referred to as *holding* shown in Figure 2.7(b). Drawing was performed by moving down the blank holder and the die, and the punch remained immobile as shown in Figure 2.7(c). During drawing operation, the force exerted by the punch was recorded against the punch displacement. It was stopped when the desired depth was reached. The cups were water quenched after the drawing. For drawing at room temperature the sequence of operation remained exactly the same except the heating and cooling steps.

After removing the cup from the tools, thickness distribution from the center to the outer diameter in the rolling and transverse direction was measured by using a micrometer. Measurement accuracy was found to be ± 0.012 mm.

The effect of sheet anisotropy during deep drawing operation was characterized by measuring the footprint. To measure the footprint digital pictures of the cups were binarized as shown in Figure 2.8. The distance between the pixels of the outer circumference and the central axis of the cup were plotted as a function to the angle from the rolling direction. It can be observed from the Figure 2.8 that the center of the bottom and the center of the outer circumference of the cup may be different and thus it is necessary to identify both centers and then trace the footprint. The center of bottom is referred as bottom center (BC) and the center of the pixels situated on the perimeter of the rim as mass center (MC). Digital image processing tool “QWin” was used to binarize, clean and filling holes of the colour picture to get BC and the pixels at the outer circumference. Another program, “GetPix”, was used to get MC and the distance of the pixels at the outer circumference from either

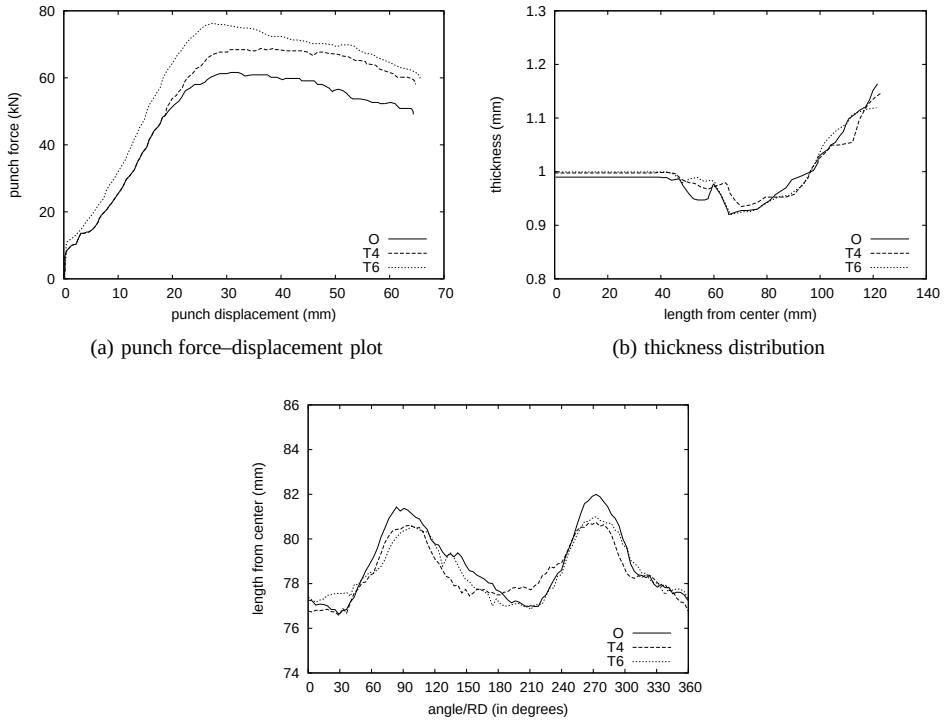

(a) punch force–displacement plot

(b) thickness distribution

(c) earing profile

Figure 2.9: Effect of tempering on cup deep drawing at 250 °C (AA 6016 alloy).

BC or MC as a function to the angle from the rolling direction, resulting in the footprint curves. The deviation of BC from MC was due to the misalignment of blank center to the center of the punch during deep drawing operation. In principle, MC is sensitive to plastic flow anisotropy effect while BC shows the effect of deviation from the bottom center of the sheet. It was observed that the deviation between MC and BC was more severe (minimum of 1.3 mm and maximum 6.2 mm) in warm deep drawing experiments, while this deviation was very small in room temperature deep drawing experiments.

2.5.2 Deep Drawing Results

In this section, the experimental cylindrical cup deep drawing results of AA 6016 and AA 6061 sheets are presented. From the results of the deep drawing tests, various effects become visible such as the effect of precipitates, temperature and strain rates on work hardening and anisotropy.

Effect of Temper In Figure 2.9, the effect of tempering on punch force–displacement, thickness distribution along the length from center to the flange and the footprint measure-

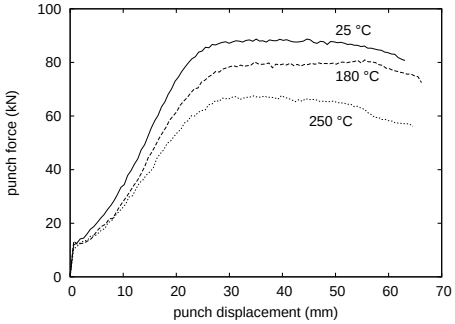

(a) AA 6016-T4 alloy

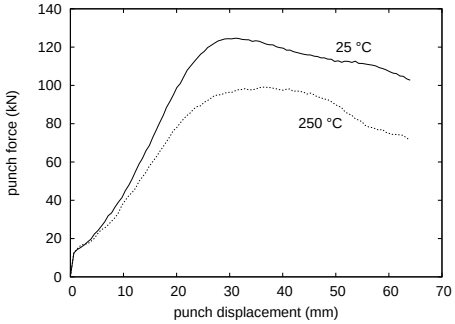

(b) AA 6061-T4 alloy

Figure 2.10: Effect of temperature on punch force–displacement plots.

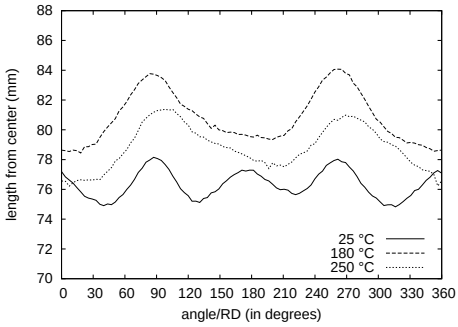

(a) AA 6016-T4 alloy

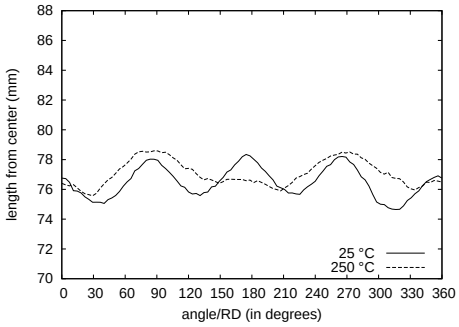

(b) AA 6061-T4 alloy

Figure 2.11: Effect of temperature on earing profiles.

ments of deep drawn cups at 250 °C are presented. The punch force–displacement plot shows that the response of T4 and "O" (fully annealed) at the beginning of deformation are equal before T4 gets stronger and deviates after some point. The earing profiles show almost no effect of precipitates (different tempering conditions). The anisotropy remained constant for all levels of temper conditions and did not bring any change in the number and position of ears. The basic nature of the thickness distribution (see Figure 2.9(c)) remained equal, like the earing profile. More thinning at the bottom of the deep drawn cup made of "O" is compared to T4 and T6 is observed, but this is within the accuracy limit of the experiment.

Effect of Temperature The effect of temperature on punch force–displacement curves, thickness distribution along the length from center to the flange and the earing profiles of deep drawn cups at 25 °C, 180 °C and 250 °C for both AA 6016-T4 and AA 6061-T4 alloys are shown in Figures 2.10, 2.11 and 2.12. From Figure 2.10, it is clearly seen that

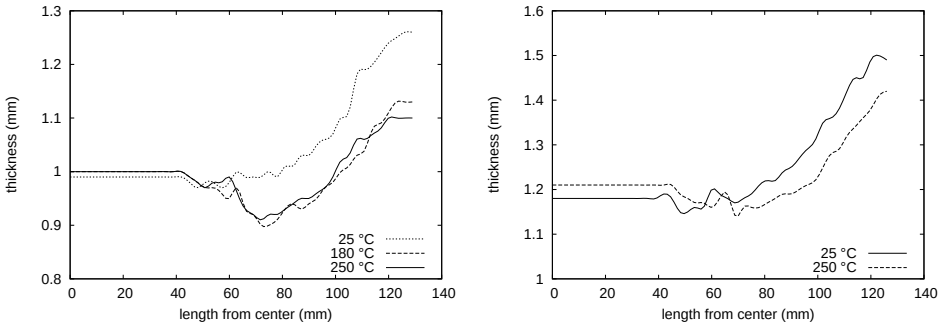

(a) AA 6016-T4 alloy (b) AA 6061-T4 alloy

Figure 2.12: Effect of temperature on thickness distribution plots.

increasing temperature from 25 °C to 250 °C significantly decreases the drawing force. Also it can be observed that, AA 6061 is stronger than AA 6016 alloy at all temperatures, which corresponds to the observation of the other mechanical tests. At 25 °C, both alloys show similar earing profiles (see Figure 2.11), *i.e.* they exhibit maxima along RD and TD and minima along 45 ° direction. At higher temperatures AA 6016 shows a minimum along the RD while AA 6061 shows minimum along $\pm 30°$ directions exhibiting a local maximum at RD. From the thickness distribution along RD presented in Figure 2.12, it can be seen that for both alloys thickness change in the wall and flange of the cup is found to be more pronounced at 250 °C compared to room temperature.

Effect of Holding Time The effect of holding time was investigated for both alloys by holding the sheets at 250 °C for different time span before drawing. The punch velocity and blank holding pressure remained constant. The holding time was varied from 10 s to 600 s. From Figure 2.13, it is clearly seen that the effect of precipitates is very limited as there is not so much difference among the punch force–displacement curves of different holding times. Although, for longer holding time the punch force–displacement curve is steeper, interestingly the maximum punch force for all the holding times has been found to be the same.

Effect of Punch Velocity The effect of punch velocity is investigated for AA 6016 at 250 °C. The punch velocity was varied from 13 mm/min to 78 mm/min. With lower punch velocity there will be more time for dynamic precipitation leading to stronger response of the material and this fact corresponds with the results obtained (see Figure 2.14). However, the effect of precipitation is small compared to other parameters, *e.g.* temperature. Punch velocity seems to have no effect on earing behavior as the nature of the curves for all three velocities are the same. The difference in magnitude of the earing profile for the punch velocity of 13 mm is due to a slightly lower drawing depth (63 mm) than the other two velocities (63 mm). As observed with the thickness distribution plot no influence of punch velocity on the thickness data is apparent.

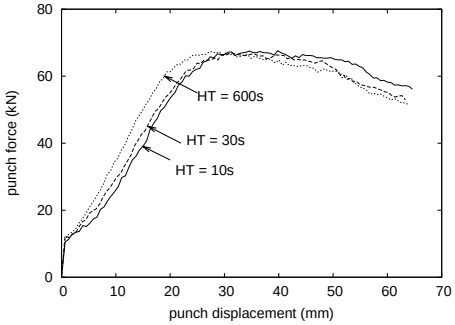

(a) AA 6016-T4

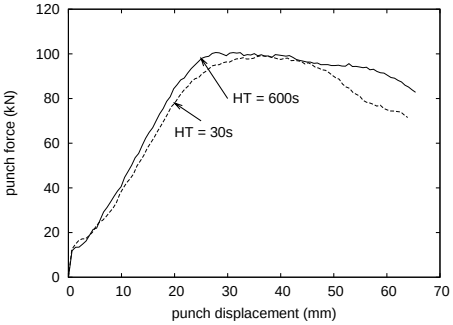

(b) AA 6061-T4

Figure 2.13: Effect of holding time on punch force–displacement plots.

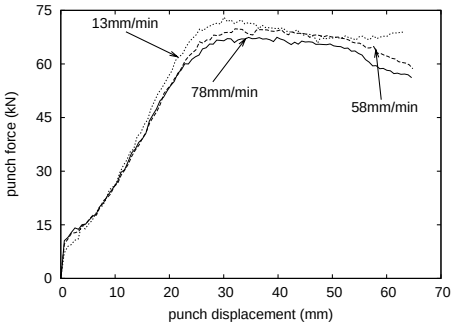

(a) punch force–displacement plot

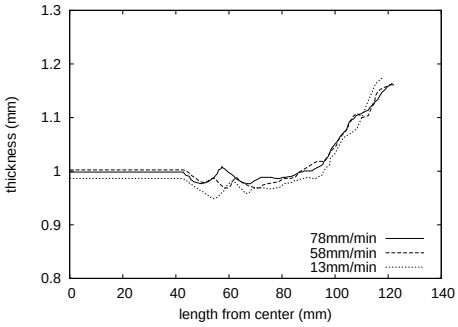

(b) thickness distribution

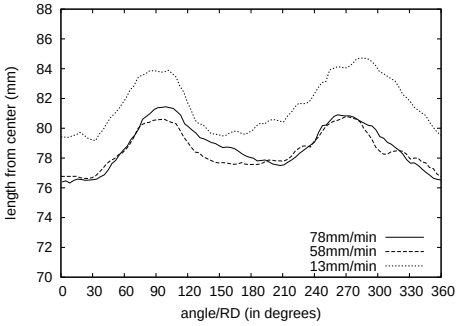

(c) earing profile

Figure 2.14: Effect of punch velocity on cup deep drawing at 250 °C (AA 6016-T4 alloy).

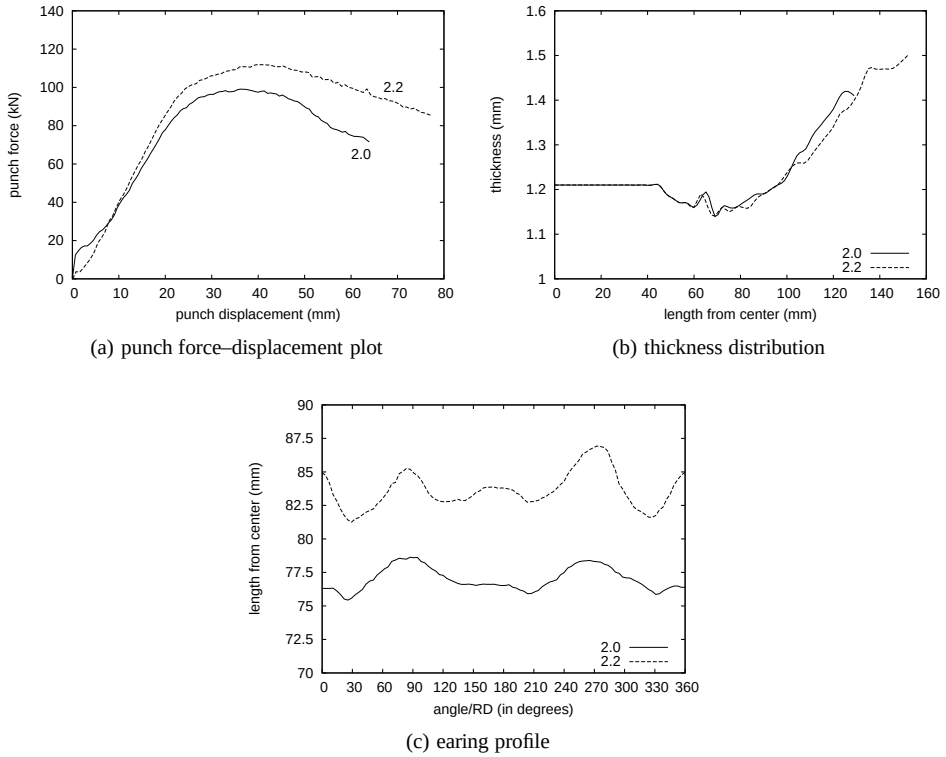

(a) punch force–displacement plot

(b) thickness distribution

(c) earing profile

Figure 2.15: Effect of drawing ratio on cup deep drawing at 250 °C (AA 6061-T4 alloy).

Effect of Drawing Ratio The effect of drawing ratio has been investigated only for AA 6061-T4 at 250 °C by performing the experiments at two different drawing ratios 2.0 and 2.2 respectively. As expected, increasing the drawing ratio increases the drawing force as shown in Figure 2.15. The earing profiles show exactly the same position of maxima and minima on footprint graphs. For higher drawing ratio the local maximum along RD has been found to be much more pronounced. From the thickness distribution plots, it is very clearly seen that there is almost no effect of drawing ratio.

2.6 Change of Anisotropy in Deep Drawing at Elevated Temperatures

When cylindrical cup deep drawing is performed on circular blanks it causes an uneven cup rim (*i.e.* a number of high points called *ears* and an equal number of low points known as *troughs*) as a result of of directional properties or anisotropy of the blank. The effect of anisotropy in deep drawing is generally viewed based on the number of ears, their location with respect to rolling direction and their amplitude. In the previous section, it was clearly

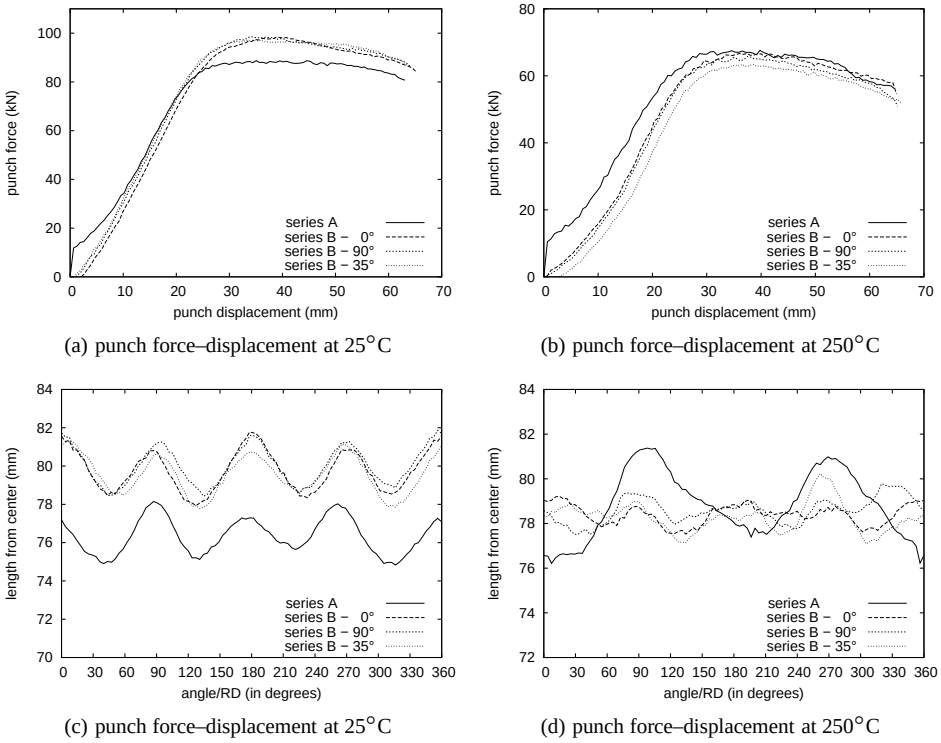

(a) punch force–displacement at 25°C

(b) punch force–displacement at 250°C

(c) punch force–displacement at 25°C

(d) punch force–displacement at 250°C

Figure 2.16: Effect of tool orientation on cup deep drawing (AA 6016-T4 alloy).

seen at room temperature the earing profile exhibits four ears in RD and TD and troughs at 45 ° with similar amplitude in their respective directions. Where as at elevated temperatures, the earing profile exhibits two ears at TD and troughs close to RD positions. It was noticed that earing appearance is similar for both alloy compositions of interest for the present investigation. It was also noticed that the difference in temper, punch velocity and holding time did not bring any change in the number and position of ears. However, for AA 6061 alloy, there was a tendency to maintain room temperature anisotropy (four ears) and this tendency was more pronounced with higher drawing ratio.

In order to understand the possible reasons for change of earing profiles from four ears to two ears with the increase of temperature, further analysis was carried out in terms of the effect of orientation of the blank with respect to the reference axis of the tool. A few tests were also conducted to study the effect of friction between the tools and the blank at elevated temperature.

In addition to the series of deep drawing tests presented in Section 2.5 (herein after called series A), two extra series of deep drawing tests (namely, series B and series C) were performed in order to be more conclusive about the earing or anisotropy behavior based on the punch force–displacement and earing profile measurements. The series B and series

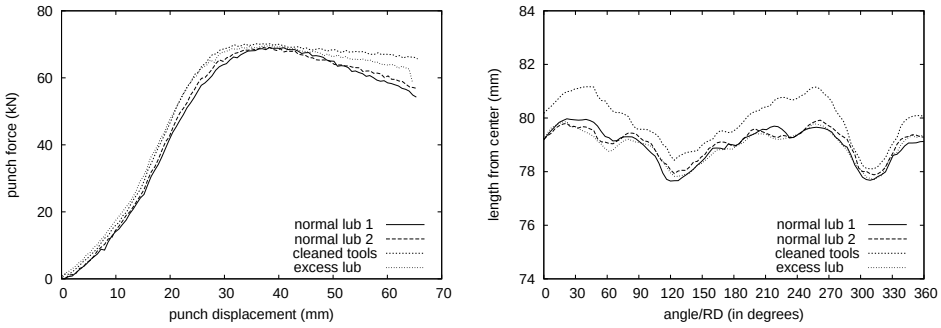

(a) punch force–displacement plot (b) earing profiles

Figure 2.17: Effect of friction at 250 °C (AA 6016-T4 alloy).

C deep drawing tests on AA 6016-T4 alloy were performed by keeping as much similar process parameters as possible in series A. Series B and series C tests were performed 4 years later than the series A tests. A very important note here is that the press tool was rebuilt before performing each series of tests, *i.e.* the orientation of press tool was really different (unknown) between each series of tests. It is also pointed out that, unless stated otherwise, all the deep drawing results of Al–Mg–Si alloys presented in this thesis are from series A.

Effect of Tool Orientation In this section, the effect of tool orientation is studied by placing the rolling direction of the blank in three different directions *i.e.* 0 °, 90 ° and an arbitrary direction 35 ° to a reference axis of the tool. In Figure 2.16, the punch force–displacement curves and earing profiles from different series of tests at 25 °C and 250 °C are compared. Tests at room temperature show that there is absolutely no effect of blank direction on the punch force–displacement as they are quite reproducible. The slightly higher maximum force for series B and C is attributed to the longer natural ageing period. A big scatter is observed for the punch force–displacement curves at 250 °C presented in Figure 2.16(b). A tendency of decreasing maximum punch force with increasing distance between BC and MC during the earing profile measurements done at 250 °C was noticed.

The earing profile of the cups deep drawn at room temperature exhibit four ears with ears at RD and TD and troughs at $\pm 45°$ from the RD. It shows absolutely no effect of tool orientation on earing behavior (see Figure 2.16(c)). At 250 °C, series B tests show not so well defined earing profiles and approximately shows four ears along RD and TD. But, on the other hand, the height of the ears are reduced considerably making the material to be more isotropic at elevated temperature.

Effect of Friction Effect of friction was studied by varying the amount of lubrication. In these tests of series C, the first two tests were performed with the normal application of the water-based lubricant on both sides of the blank. For the next test, the entire tools were cleaned in order to avoid the lubricant leftovers on the tools from previous tests and a regular

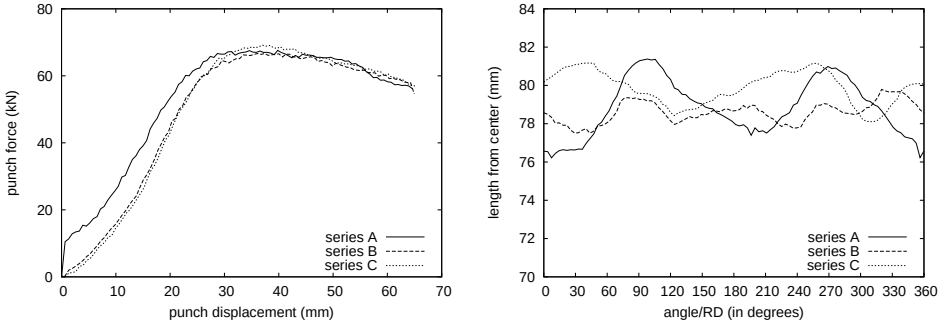

(a) punch force–displacement plot

(b) earing profiles

Figure 2.18: Comparing different series of tests at 250 °C (AA 6016-T4 alloy).

amount of lubricant was applied on the blank. For the last test excess amount of lubricant was applied on both sides of the blank. The punch force–displacement curves and earing profiles from these tests are compared in Figure 2.17.

From the punch force–displacement curves presented in Figure 2.17(a), tests with normal application of lubricant are well reproducible. When the tools are cleaned before doing a test, not only is the maximum punch force larger, but it is also overestimated at larger drawing depths in particular. In the test with extra lubricant, the punch force is larger than the test with normal application of the lubricant: this was not expected. From the earing profile plot it is clearly seen that the results are well reproducible and lubrication conditions do not have an effect on the earing profile, but the height of the ears are dependent on lubrication conditions. It is also noticed that the earing profile for series C is different from series B.

In Figure 2.18, the deep drawing test results from different series of experiments at 250 °C are compared. From the punch force–displacement plot, the maximum punch force for series B and C is slightly higher due to the longer natural ageing period. When comparing the earing profiles from different series of experiments, they are completely different from each other, even though the height of the ears are small for series B and C. It is reminded here that the press tool was rebuilt for each series of tests and it can be concluded that the earing behavior at elevated temperature is highly sensitive to the press tool setup.

2.7 Discussion

In this chapter some characteristics of Al–Mg–Si alloys were introduced that are relevant for the warm forming process. The work hardening rate in a precipitation hardened alloy is generally controlled by the solute levels left in the metal matrix that control the dynamic recovery and the interaction of dislocations with precipitates. The decrease of work hardening rate due to change in temper state from T4 to T6 is associated with the formation of shearable and coarser precipitates in T6 state. This results in greater hindrance for dislocations to pass or cut through the precipitates under T6 state resulting in a decrease of the storage of so-called geometrically necessary dislocations at the vicinity of grain bound-

aries or subgrain boundaries. Optimum sized shearable precipitates or any other dislocation storage sites leads to a higher initial yield strength. The hardening rate also reduces with increasing temperature. The test with extremely slow deformation rate gave evidence of dynamic precipitation followed by dynamic recovery.

Precipitates do not seem to have any influence on anisotropy. The R value profile remains similar under different tempering conditions. The oriention of the press tools and friction between tool and blank do not have any influence on the earing profile only at room temperature. The earing behavior at elevated temperature is highly sensitive to the press tool setup.

With a proper material model, it should be possible to represent all the above observations. The mechanical response of different alloys introduced in this chapter provides a good basis for finding the parameters of the material models under different temperatures and strain rates presented in the next chapter.

3. Material Models for Warm Forming

Numerical analysis is a critical tool for understanding the complex deformation mechanisms that occur during sheet forming processes. Accuracy of numerical analysis depends largely on the use of a constitutive model that describes the complex behavior of the material. In this chapter, a number of material models for warm forming of aluminum alloys are presented and their predictive capabilities are verified. Material models for plastic deformation that are used in process simulations commonly use the concept of yield surface, the flow rule and the hardening rule. The same approach is used here.

In Section 3.1, a short repetition of classical constitutive framework of plasticity theory is presented. Special attention is paid to anisotropic plastic behavior in a plane stress condition. In Section 3.2, two different yield functions are described that are suitable for use in numerical simulation of aluminum sheet forming. In Section 3.3 the work hardening and the influence of the temperature and strain rate are considered. The yield functions and hardening models will be used in the warm forming simulations in the next chapters. In Section 3.7, the predictive power of different hardening models is compared with uniaxial tensile tests on 5754-O alloy used as a representative example of aluminum alloys. The chapter ends with a short summary.

3.1 Constitutive Framework—Plasticity

In this work, material models are considered for application in finite element analyses of thermo-mechanical sheet forming processes such as temperature enhanced forming or stretch forming with intermediate heat treatments. Thus a material model or constitutive model should describe thermo-mechanical deformation in terms of the macroscopic stresses and strains. Several classes of constitutive models are well-known in the continuum mechanics framework: elasticity, plasticity, creep, viscosity etc. This section deals with the basic concepts, that are used in elasto-plasticity, namely: the yield surface, the flow rule and the hardening rule. These phenomena are most relevant to the deformation of sheet metals. The yield surface determines *when* plastic flow occurs, the flow rule determines the *direction* of the plastic flow, the hardening rule determines the *evolution* of the yield surface. A more comprehensive overview of the formulations can be found in (Belytschko *et al.*, 2006; Zienkiewicz and Taylor, 2005; Simo and Hughes, 2000; Crisfield, 1997).

The yield surface can change size, position and shape, due to *e.g.* plastic deformation or a temperature change. A change of size, while the center of the yield surface and the shape remain constant, can be modeled with isotropic hardening or softening. This is the most commonly used hardening model.

3.1.1 The Yield Surface

A yield surface is defined as the hyper surface which encloses the elastic region in the 6-dimensional stress space. Usually in the analysis of sheet metal forming all out of plane components of the stress vector are assumed to be equal to zero and the yield criterion is defined in the plane stress space. For sheet forming simulations, the σ_x–σ_y-plane is the commonly used cross section to present a yield locus, where x and y denote two orthogonal axes in the sheet plane. A typical example is shown in Figure 3.1.

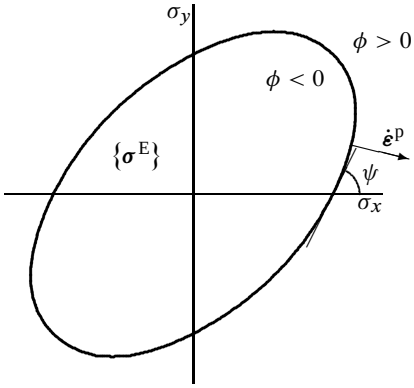

Figure 3.1: Typical yield locus for the σ_x–σ_y-plane.

The yield surface bounds the elastic region $\{\boldsymbol{\sigma}^{\mathrm{E}}\}$. For numerical computations, a yield function $\phi = \phi(\boldsymbol{\sigma}, ...)$ can be defined. The yield function depends on the stress tensor and additional variables, *e.g.* determined by the deformation history. The equation $\phi = 0$ represents the yield surface. If $\phi < 0$ the material behaves elastically. Stress states where $\phi > 0$ are not feasible in an elasto-plastic theory. If the stress state is on the yield surface, plastic deformation can occur. Following Drucker's postulate, the plastic strain rate $\dot{\boldsymbol{\varepsilon}}^{\mathrm{p}}$ is perpendicular to the yield surface,

$$\dot{\boldsymbol{\varepsilon}}^{\mathrm{p}} = \dot{\lambda} \frac{\partial \phi}{\partial \boldsymbol{\sigma}} \tag{3.1}$$

where $\dot{\lambda}$ is a consistency parameter. As a consequence of Drucker's postulate, the yield surface must be convex. Equation (3.1) referred to as *associated flow rule*, establishes the relation between the stress and the plastic strain increments (or rates). In associated plasticity the yield surface $\phi(\boldsymbol{\sigma})$ is used as a plastic dissipation potential.

3.1.2 Anisotropy: Lankford Strain Ratio

The properties of aluminum and its alloys, as with most metals, are never completely uniform in all directions—some degree of anisotropy is always present. The exact nature of this anisotropy depends upon both alloy composition and process history (*e.g.* casting, rolling, extrusion, annealing, etc). Anisotropic properties can have a major effect on subsequent process stages, especially sheet metal forming processes such as deep drawing and stretch

forming, and on in-service performance. Rolling the sheet causes orthotropic symmetry with three main directions: the rolling direction (RD), the transverse direction (TD) and the normal direction (ND). If a uniaxial tensile test specimen will be cut from such a piece of rolled sheet material, with the tensile direction x at an angle θ to the rolling direction, the strain ratio R_θ is defined as Lankford strain ratio, which is the ratio between the strain in width direction ε_y and the thickness strain ε_z.

$$R_\theta = \frac{\varepsilon_y}{\varepsilon_z} \tag{3.2}$$

where: $\varepsilon_y = \ln(w/w_0)$ and $\varepsilon_z = \ln(t/t_0)$, the true strain in the width and thickness directions respectively. Since the thickness strain is difficult to measure, the volume constraint is invoked and the strain ratio can be calculated as

$$R_\theta = \frac{\varepsilon_y}{-(\varepsilon_x + \varepsilon_y)} \tag{3.3}$$

If the sheet is *planar isotropic*, it has the same properties in all directions within the plane of the sheet. Therefore, in this case, R is independent of θ. If R is dependent on θ, then the sheet is *planar anisotropic*. Materials with a high R value have a low thickness strain compared to the strain in width direction. They have thus a high resistance against sheet thickness fluctuations, and are therefore said to have a good formability.

3.2 Yield Functions for Sheet Forming Simulations

Many yield criteria have been developed over the years. For isotropic metallic materials, the well-known Von Mises or Tresca yield functions are often sufficient to describe the plastic behavior of metals. However, in sheet metal forming the sheet materials are usually anisotropic with respect to their plastic properties. In order to take into account this plastic anisotropy, the yield function can be considered by introducing additional parameters to describe the plastic anisotropic behavior. These parameters may be adjusted to a set of selected experimental data obtained by subjecting specimens of the considered material to mechanical tests. The most prominent yield function of this type has been proposed by Hill (1948). Hill's classical yield function, also known as the Hill '48, is the most frequently used yield function to account for plastic anisotropy, mainly due to its simple handling in numerical calculations. Lankford coefficients are sufficient to define the Hill '48 parameters and only three uniaxial tensile tests are needed to measure the Lankford coefficients R_0, R_{45} and R_{90}. However, this yield function is only able to describe the plane stress yield locus as a more or less stretched ellipse. This yield locus shape is very often inconsistent with experimental yield loci or those obtained from polycrystal calculations, especially for aluminum alloys. This is the origin of the so-called anomalous behavior of aluminum sheet (Woodthorpe and Pearce, 1970). With the above-stated reasons, Hill '48 yield function is not used in this work.

3.2.1 Vegter Yield Function

The Vegter yield function (Vegter and van den Boogaard, 2006) is one of the most accurate yield functions for aluminum alloy sheets defined in plane stress conditions . The Vegter

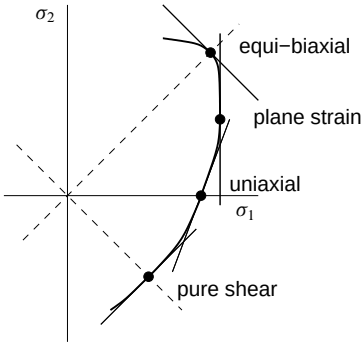

Figure 3.2: Basic stress points required to construct the Vegter yield locus.

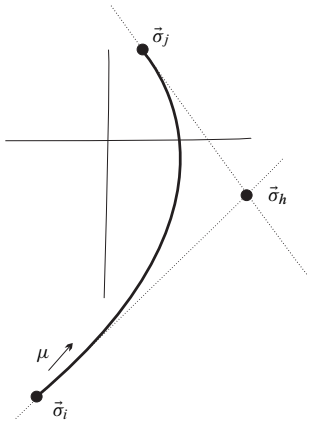

Figure 3.3: A second order Bezier curve.

yield locus is constructed in principal stress space and uses the Bezier interpolation to connect the measured yield stresses in equi-biaxial, plane strain tension, uniaxial tensile and pure shear tests as shown in Figure 3.2. This leads to 4 stress points in the region where $\sigma_1 > \sigma_2$. For the situations where $\sigma_1 < \sigma_2$ can be determined if the sample is rotated by 90 °. The compressive part of the yield locus is usually not measured from the experiments, but is defined by the assumption that initial yield stress in compression is equal to that in tension.

Continuous differentiability of the yield locus has been verified by not only measuring the yield stress at yielding, but also the direction of the strains to determine the local tangent of the yield surface, since Drucker's postulate states that the plastic flow is perpendicular to the yield surface. With the stress points and their tangents available, second order Bezier curves can be constructed between the stress points as shown in Figure 3.3. A stress state in the two-dimensional stress space is represented with a vector:

$$\vec{\sigma} = \begin{Bmatrix} \sigma_1 \\ \sigma_2 \end{Bmatrix} \tag{3.4}$$

For every part of the yield locus between the two reference stress states, $\vec{\sigma}_i$ and $\vec{\sigma}_j$, a second order Bezier function is determined and the hinge point $\vec{\sigma}_h$ is defined with the tangents drawn at the two reference stress states. The yield locus between the two reference stress states is defined by:

$$\vec{\sigma}_{\text{locus}} = \vec{\sigma}_i + 2\mu\left(\vec{\sigma}_h - \vec{\sigma}_i\right) + \mu^2\left(\vec{\sigma}_i + \vec{\sigma}_j - 2\vec{\sigma}_h\right) \qquad \mu \in [0,1] \tag{3.5}$$

Now the definition of stress state in the classical rate independent plasticity setting is given by:

$$\vec{\sigma} = \frac{\sigma_{\text{eq}}}{\sigma_{\text{f}}}\left[\vec{\sigma}_i + 2\mu\left(\vec{\sigma}_h - \vec{\sigma}_i\right) + \mu^2\left(\vec{\sigma}_i + \vec{\sigma}_j - 2\vec{\sigma}_h\right)\right] \qquad \mu \in [0,1] \tag{3.6}$$

where σ_{f} is the current flow stress and σ_{eq} is the equivalent stress. The quantity $\sigma_{\text{eq}}/\sigma_{\text{f}}$ gives the magnitude of the stress. A yield function ϕ that is defined as

$$\phi(\boldsymbol{\sigma}, \varepsilon^{\text{p}}_{\text{eq}}) = \sigma_{\text{eq}}(\boldsymbol{\sigma}) - \sigma_{\text{f}}(\varepsilon^{\text{p}}_{\text{eq}}) \tag{3.7}$$

fulfills the condition that $\phi = 0$ on the yield locus and $\phi < 0$ in the elastic regime. The direction of the plastic strain rate can be calculated from the derivative of ϕ to the stress $\boldsymbol{\sigma}$. Since ϕ is continuously differentiable, the plastic strain rate direction is continuous.

Planar anisotropic behavior can be modeled by defining all reference stress points and corresponding normals depending on the angle θ. The reference stress points and normals are defined by an interpolation, based on Fourier series.

$$\vec{\sigma}_k(\theta) = \sum_{j=0}^{n} \vec{\varsigma}_{kj} \cos(2j\theta) \tag{3.8}$$

$$\left(\frac{\partial \phi}{\partial \vec{\sigma}}\right)_k (\theta) = \sum_{j=0}^{n} \vec{\varphi}_{kj} \cos(2j\theta) \tag{3.9}$$

To use the Vegter model for common rolled material, that develop four ears in deep drawing of cylindrical cup experiments in 3 directions (0°, 45° and 90° directions with respect to the rolling direction) are required to determine the 14 material parameters.

3.2.2 Barlat Yld2000 Yield Function

The Yld2000 anisotropic yield function presented by Barlat *et al.* (2003) is another accurate yield function for aluminum alloy sheets. The Barlat anisotropic yield functions are derived based on the approach of linear transformations of a stress tensor.

The anisotropic yield function for plane stress plasticity can be expressed in general form (Hosford, 1972; Barlat *et al.*, 2003):

$$\phi = \phi' + \phi'' = 2\sigma_{\text{f}}{}^a \tag{3.10}$$

where $\phi' = |\tilde{S}'_1 - \tilde{S}'_2|^a$ and $\phi'' = |2\tilde{S}''_2 + \tilde{S}''_1|^a + |2\tilde{S}''_1 + \tilde{S}''_2|^a$ with $a = 6$ and $a = 8$ for b.c.c. and f.c.c. materials respectively. ϕ' and ϕ'' are two isotropic plane stress functions. Equivalently, the anisotropic function ϕ is associated with the effective stress

$$\sigma_{\text{eq}} = \left\{\frac{1}{2}\left(|\tilde{S}'_1 - \tilde{S}'_2|^a + |2\tilde{S}''_2 + \tilde{S}''_1|^a + |2\tilde{S}''_1 + \tilde{S}''_2|^a\right)\right\}^{1/a} \tag{3.11}$$

$\tilde{S}'_{1,2}$ and $\tilde{S}''_{1,2}$ are the principal values of the linear transformations on the stress deviator $\mathbf{s}$ are given by

$$\tilde{\mathbf{S}}' = \mathbf{G}' \cdot \mathbf{s} = \mathbf{G}' \cdot \mathbf{T} \cdot \boldsymbol{\sigma} = \mathbf{L}' \cdot \boldsymbol{\sigma} \tag{3.12a}$$

$$\tilde{\mathbf{S}}'' = \mathbf{G}'' \cdot \mathbf{s} = \mathbf{G}'' \cdot \mathbf{T} \cdot \boldsymbol{\sigma} = \mathbf{L}'' \cdot \boldsymbol{\sigma} \tag{3.12b}$$

In the above equations, $\mathbf{G}'$ and $\mathbf{G}''$ are linear transformation tensors on stress deviator $\mathbf{s}$. The tensors $\mathbf{L}'$ and $\mathbf{L}''$ representing linear transformations of the Cauchy stress $\boldsymbol{\sigma}$ are given by: are

$$\begin{bmatrix} L'_{11} \\ L'_{12} \\ L'_{21} \\ L'_{22} \\ L'_{66} \end{bmatrix} = \begin{bmatrix} 2/3 & 0 & 0 \\ -1/3 & 0 & 0 \\ 0 & -1/3 & 0 \\ 0 & 2/3 & 0 \\ 0 & 0 & 0 \end{bmatrix} \begin{bmatrix} \alpha_1 \\ \alpha_2 \\ \alpha_7 \end{bmatrix} \tag{3.13}$$

$$\begin{bmatrix} L''_{11} \\ L''_{12} \\ L''_{21} \\ L''_{22} \\ L''_{66} \end{bmatrix} = \frac{1}{9} \begin{bmatrix} -2 & 2 & 8 & -2 & 0 \\ 1 & -4 & -4 & 4 & 0 \\ 4 & -4 & -4 & 1 & 0 \\ -2 & 8 & 2 & -2 & 0 \\ 0 & 0 & 0 & 0 & 9 \end{bmatrix} \begin{bmatrix} \alpha_3 \\ \alpha_4 \\ \alpha_5 \\ \alpha_6 \\ \alpha_8 \end{bmatrix} \tag{3.14}$$

The independent coefficients α_k (for $k : 1, \ldots, 8$) are all that is needed to describe the anisotropy of the material. For the isotropic case they reduce to 1.

At least eight independent test results are required to identify the eight anisotropy coefficients. Usually, six of eight input data are the uniaxial flow stresses and R values measured in three different directions from rolling, σ_0, σ_{45}, σ_{90}, R_0, R_{45} and R_{90}. The other two are the equi-biaxial flow stress σ_b and the equi-biaxial strain ratio, R_b measured from the bulge test/disk compression test. R_b defines the slope of the yield surface at the equi-biaxial stress state ($R_\mathrm{b} = \dot{\varepsilon}_{yy}/\dot{\varepsilon}_{xx}$). With eight test results, eight nonlinear equations can be obtained using the yield function for the flow stresses and the associated flow rule for the R values and solved for the anisotropic constants.

3.3 Flow Stress and Hardening

The flow stress σ_f is a measure for the resistance to plastic deformation of a material. It is usually defined as the true yield stress in a uniaxial tensile test. In most metal alloys, the flow stress increases upon plastic deformation. This is known as *work hardening* or *strain hardening*. The warm forming uniaxial experiments presented in Section 2.3 showed that the work hardening in aluminum alloys also depends on the temperature and strain rate.

3.3.1 Phenomenological Vs. Physically Based Models

For numerical analysis, a description of this work hardening is required. A class of traditional models describe the flow stress in terms of mathematical equations such as power laws, as a function of strain with many empirical constants by fitting the experimental test data. These *phenomenological* models are also named engineering models as they are more common in

engineering applications. Usually, empirical models have little *or* no physics in them and the constants usually cannot be related to any physical process or phenomenon. In spite of this inherent disadvantage, these models are extensively used in FEM codes to model plasticity as they require low computational resources and provide excellent fits for a given deformation condition, but these models do not have any predictive power beyond the experimental data range. A well-known phenomenological model based on Nadai hardening law with strain rate and temperature effects (Van den Boogaard and Huétink, 2006; Abedrabbo *et al.*, 2007) is described in Section 3.4.

For warm forming of aluminum, the strain rate and temperature have a significant influence on the flow stress. Regardless of their remarkably good fit to the measured stress–strain curves within a certain range of strains, strain rates and temperatures, empirical relations have no predictive power beyond that range of deformation conditions. Hence, their usage is limited only to the range of deformation conditions at which they were curve-fitted, and the accuracy outside that range is often not satisfactory. Models that are based on the physics of plastic deformation may have a wider applicability, *i.e.* model the microstructure evolution indirectly, so that the effects of the micro level processes are somehow accounted for, perhaps in an average way, on the macro level. These type of models are called *physically based models*. Such type of approach, using the notion of dislocation density, is the subject of the study in this thesis.

In Section 3.5 and Section 3.6, the two mainstream dislocation density based models (Bergström (1969, 1983); Nes (1998)) are discussed. They all have similar basic assumptions and ideas about dislocation density evolution processes, which basically consist of *storage* and *recovery*. But the particular forms of the equations are often different. In the subsequent chapter it will be shown also that such phenomena as strain rate and temperature effects can be accounted for by these kinds of dislocation models. The accuracy of one or another model should be validated by further experimental observations.

3.4 Phenomenological Extended Nadai Model

The phenomenological model is based on the Nadai hardening law and power law strain rate dependency:

$$\sigma = C(\varepsilon + \varepsilon_0)^n \left(\frac{\dot{\varepsilon}}{\dot{\varepsilon}_0}\right)^m \tag{3.15}$$

The temperature dependence is included by letting C, n and m be functions of the temperature T (in Kelvin). The following functions for the parameters were used in order to fit the tensile tests.

$$C(T) = C_0 + a_1\left[1 - \exp\left(a_2\frac{T-273}{T_\mathrm{m}}\right)\right] \tag{3.16a}$$

$$n(T) = n_0 + b_1\left[1 - \exp\left(b_2\frac{T-273}{T_\mathrm{m}}\right)\right] \tag{3.16b}$$

$$m(T) = m_0 \exp\left(c\frac{T-273}{T_\mathrm{m}}\right) \tag{3.16c}$$

where T is the absolute temperature. T_m is used to make that part of the formulas dimensionless and can be chosen arbitrarily.

3.5 Bergström Model

The physically based model given here was first described by (Bergström, 1969). The deformation resistance of metals is divided into three parts:

$$\sigma_\mathrm{f} = \sigma_0(T) + \sigma_\mathrm{w}(\rho, T) + \sigma^*(\dot{\varepsilon}, T) \tag{3.17}$$

with σ_0 the strain rate independent stress, σ_w the contribution of the strain hardening and σ^* a dynamic stress that depends on the strain rate and temperature.

The influence of the dynamic stress σ^* is decreasing with increasing temperature and is independent of the strain. Van den Boogaard (2002) observed in experiments with 5754-O alloy that the influence of the strain rate on the initial yield stress is almost absent between 300 K and 450 K and increases rapidly at higher temperatures. This cannot be modeled with the common notion of the dynamic stress and therefore the dynamic stress is neglected (Van den Boogaard and Huétink, 2006).

For the contribution of strain hardening σ_w a simple one parameter model is used where the evolution of the dislocation density ρ is responsible for the hardening. The relation between the dislocation density and the strain hardening is given by the Taylor equation:

$$\sigma_\mathrm{w} = \alpha G(T) b \sqrt{\rho} \tag{3.18}$$

with α a scaling parameter, G the elastic shear modulus and b the Burgers vector (Van den Boogaard, 2002).

The essential part of (3.18) is the evolution of the dislocation density. The creation and storage of dislocations is taken to be proportional to the mean free path, while dynamic recovery is taken to be proportional to the dislocation density itself. This leads to the basic equation for the Bergström model (Bergström, 1969).

$$\frac{\mathrm{d}\rho}{\mathrm{d}\varepsilon} = c_1 \frac{1}{L} - c_2 \rho \tag{3.19}$$

where the recovery parameter c_2 depends on temperature and strain rate. In the original Bergström model, the mean free path L was considered to be constant.

The formation of dislocation walls and the principle of similitude led Vetter and van den Beukel (1977), to a storage factor that is proportional to the square root of the dislocation density. The dynamic recovery term is considered to be due to annihilation and remobilization of immobile dislocations. The remobilization is a thermally activated process, based on vacancy climb (Bergström, 1983). The evolution of dislocation density is now reformulated as

$$\frac{\mathrm{d}\rho}{\mathrm{d}\varepsilon} = U(\rho) - \Omega(\dot{\varepsilon}, T)\rho \tag{3.20}$$

with U the immobilization rate of dislocations and Ω the remobilization rate of dislocations:

$$U = U_0 \sqrt{\rho} \tag{3.21}$$

$$\Omega = \Omega_0 + C \exp\Big(- \frac{m Q_v}{RT} \Big) \dot{\varepsilon}^{-m} \tag{3.22}$$

with U_0 the intrinsic immobilization rate, Ω_0 the low temperature, high strain rate limit value of the remobilization probability, C and m constants, Q_v the activation energy and R the gas constant.

Equation (3.20) can be integrated analytically for constant U_0 and Ω (Van Liempt, 1994; Estrin, 1996). For an incremental algorithm, the dislocation density ρ_{j+1} at time t_{j+1} can be calculated from:

$$\rho_{j+1} = \left[\frac{U_0}{\Omega} \Big(\exp(\tfrac{1}{2}\Omega \Delta\varepsilon) - 1 \Big) + \sqrt{\rho_j} \right]^2 \exp(-\Omega \Delta\varepsilon) \tag{3.23}$$

where U_0 and Ω are assumed to be constant during the time increment. This gives a contribution to the flow stress of:

$$\sigma^w_{j+1} = \alpha G b \sqrt{\rho_{j+1}} \tag{3.24}$$

which leads to:

$$\sigma^w_{j+1} = \alpha G b \left[\Big(\frac{U_0}{\Omega} - \sqrt{\rho_j} \Big) \Big(1 - \exp(-\tfrac{1}{2}\Omega \Delta\varepsilon) \Big) + \sqrt{\rho_j} \right] \tag{3.25}$$

The strain rate independent stress σ_0 is assumed to relate to stresses in the atomic lattice. Therefore the temperature dependence of the shear modulus $G(T)$ is also used for the strain rate independent stress (Rietman, 1999; Van den Boogaard, 2002).

Combining (3.17) with the information described above results in:

$$\sigma_f = g(T) \Big(\sigma_0 + \alpha G_{ref} b \sqrt{\rho} \Big) \tag{3.26}$$

with $g(T)$ the shear modulus divided by the reference value G_{ref}. The temperature dependence can numerically be represented by the empirical relation:

$$g(T) = 1 - C_T \exp\left(- \frac{T_1}{T} \right) \tag{3.27}$$

with C_T and T_1 fitting parameters.

3.6 Nes Model

The work hardening model developed by Nes and co-workers has earlier been referred to as ALFLOW and Microstructural Metal Plasticity (MMP) model but will here simply be referred to as the Nes model (Nes, 1998; Marthinsen and Nes, 2001; Nes and Marthinsen, 2002). The Nes model gives a detailed description of the microstructure evolution by multi parameters given in Section 3.6.2. The influence of microstructure on flow stress is described in Section 3.6.1.

The work hardening curve, as shown in Figure 3.4(a), can generally be divided into four or five different stages. Stage I, easy glide, only occurs in single crystals. The other stages occur in single crystals as well in polycrystal materials. Stage II is characterized by a constant work hardening rate as shown in Figure 3.4(b). In stage III the work hardening rate decreases while in stage IV the work hardening rate is nearly constant again. At very high temperatures also a stage V, a constant saturation stress, is observed.

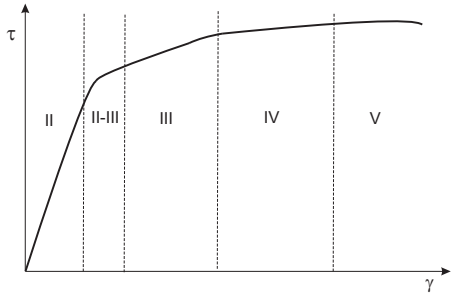

(a) Different stages in a stress–strain curve

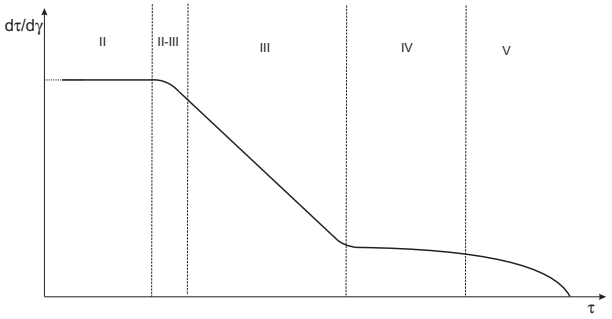

(b) Different stages in work hardening rate Vs flow stress curve

Figure 3.4: Schematic representation of different stages in work hardening.

The Nes theory relies on composite description for the microstructure evolution. At small strains during stage II deformation a very strong hardening is caused by a rapid increase of the density of stored dislocations. The main part of the dislocations is then stored in the complex three dimensional Frank network. Cell walls are formed, in which the dislocation density is slightly higher and is characterized by a cell size, δ, cell walls of thickness, h, and wall dislocation density, ρ_b, and a density within cells, ρ_i as shown in Figure 3.5(a). At large strains the difference is that the cell walls have collapsed into subboundaries as shown in Figure 3.5(b) with a well defined misorientation, φ, *i.e.* stage III behavior occurs as the recovery in the Frank network becomes stronger and balances the storage rate. The further hardening in late stage III and stage IV is caused by the reduced average spacing between subgrain boundaries, which is a result of dislocations forming new subgrain boundaries

when stored. Stage III is strongly influenced by the collapse of cell walls into sharper subgrain boundaries. Many of the dislocations become stored in old walls/boundaries and increase the misorientations between subgrains. Extensive presentations are given in Nes (1998); Marthinsen and Nes (2001); Nes and Marthinsen (2002). In this section a brief overview is presented.

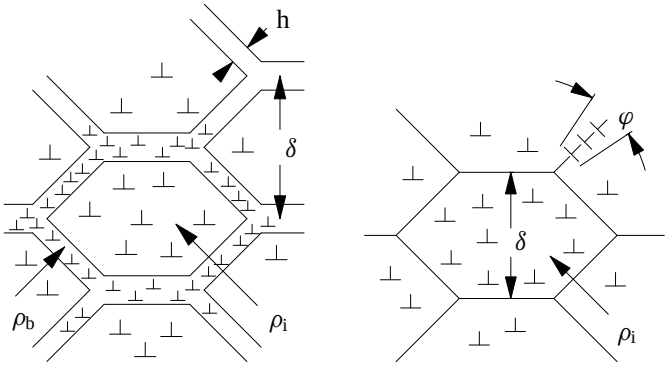

(a) Small deformations (b) Large deformations

Figure 3.5: Schematic presentation of the dislocation cell structure

3.6.1 The Flow Stress

The flow stress, τ, at a known microstructure is commonly defined in terms of a thermal component, τ_t, and an athermal stress component τ_a, so that $\tau = \tau_t + \tau_a$. The thermal component τ_t is due to the rate and temperature *dependent* interactions with short range obstacles and the athermal component characterizes the rate and temperature *independent* interactions due to long range barriers.

The thermal stress To calculate the thermal stress τ_t, it is assumed that the mobile dislocation density ρ_m is proportional to the total stored dislocation density ρ, *i.e.* $\rho_m \propto m\rho$. Where ρ is given as:

$$\rho = \rho_i + \frac{\kappa_0 \varphi}{b\delta} \tag{3.28}$$

In pure metals the thermal stress component reflects the short range interactions associated with cutting of "trees" and dragging of jogs. In alloys with a significant amount of atoms in solid solution (like Al–Mg alloys), the thermal stress component is expected to be controlled by thermal activation of solute atoms away from climbing jogs on screw dislocations. In any of these cases the thermal stress is determined by the Orowan equation:

$$\dot{\gamma} = \rho_m b v \tag{3.29}$$

The average speed of the mobile dislocations, v, may generally be expressed as:

$$v = l_a B_t \nu_D \exp\left(-\frac{U_t}{kT}\right) 2\sinh\left(\frac{V_t \tau_t}{kT}\right) \tag{3.30}$$

where k is the Boltzmann constant, ν_D is the Debye frequency, V_t is an activation volume and U^t is an activation energy, B_t is a constant and T is the temperature. If the solute content is sufficiently large the average dislocation speed is controlled by the dragging of elements in solid solution. Then the relaxation distance, $l_a = b c_{sc}^{e_t - 1}/\omega_t$, is the distance traveled by a climbing jog in between thermal activation and subsequent pinning of a solute atom. In the case of pure metals the activation energy is expected to be approximately that of self diffusion, $U_t \approx U_{sd}$. For solid solution alloys, U_t should be replaced by summation of activation energy for solute diffusion U_s and interaction energy between solute and dislocations ΔU_s. The activation volume is given by the spacing of solute atoms along the dislocation core, $V_t = b^2 l_s = b^3 \omega_t / c_{sc}^{-e_t}$. Where l_s scales with the spacing of the solute atoms along the dislocation core, ω_t is a parameter which needs to be determined from experimental flow curves and the exponent e_t is expected to have a size in the range 0.5 to 1.

The athermal stress The athermal component, τ_a is the stress contribution due to non-deformable particles (τ_p), clusters (τ_{cl}) and due to the stored dislocations (τ_d) and are considered as long range contributions.

$$\tau_a = \tau_p + \tau_{cl} + \tau_d \tag{3.31}$$

The *Orowan bypass stress* τ_p, due to presence of non-shearable particles

$$\tau_p = \left(\frac{AGb}{2\pi 1.24}\right) \frac{\ln(\lambda/b)}{\lambda} \tag{3.32}$$

Here A is a constant and $\lambda = 0.8\left(\sqrt{\pi/f_r} - 2\right) r$ is the spacing between non-shearable particles in the slip plane with average radius, r, filling a volume fraction, f_r.

The *clustering stress*, τ_{cl}, due to clusters formed by low diffusivity alloying components *e.g.* Fe, Mn, Si.

According to Nes and Marthinsen (2002), for the description of stress contribution due to *stored dislocations* (τ_d), a one-parameter stress relation is assumed to be valid in the small strain regime, namely the critical resolved shear stress is proportional to the square root of the total dislocation density. It means that the multi-parameter description of the microstructure is strictly not necessary at these small strains, since the microstructure quantities can be determined from the total dislocation density by the so-called *principle of scaling*. The dislocation density in the cell interior ρ_i is related to the wall dislocation density ρ_w as $\rho_w = q_b^2 \rho_i$, similarly the cell wall spacing as $\delta = q_c/\sqrt{\rho_i}$ with the assumed constant volume fraction, f, of cell walls. Here q_b and q_c are the scaling parameters.

A "composite" of two phases is considered:

$$\rho = \begin{cases} \rho_i & \text{in a volume fraction } (1-f) \text{ inside the subgrains} \\ \rho_w = q_b^2 \rho_i & \text{in a volume fraction } f \text{ of subgrains} \end{cases} \tag{3.33}$$

The microstructure is solely represented by one parameter:

$$\rho = (1 - f)\rho_{\mathrm{i}} + f\rho_{\mathrm{w}} \tag{3.34}$$

A volume average of the stress contributions of a "composite" is given by:

$$\tau_{\mathrm{d}} = \alpha_1 Gb\sqrt{\rho} = (1 - f)\alpha_1 Gb\sqrt{\rho_{\mathrm{i}}} + f\alpha_1 Gb\sqrt{\rho_{\mathrm{w}}} \tag{3.35}$$

The principle of scaling is broken by the onset of dynamic recovery. The cell walls are then transformed into sharp subgrain boundaries with misorientations. The subgrain boundaries now represent a very small volume and do not contribute significantly from the "composite" point of view ($f\alpha_1 Gb\sqrt{\rho_{\mathrm{w}}} \to 0$). As the spacing between the subboundaries becomes small, a new mechanism becomes important, namely the stress due to bow out of the dislocations caused by the spacing between subboundaries. This term is proportional to the inverse of the spacing between boundaries. If the effect of grain boundaries is also considered, then the stress component due to storage of dislocation is given by

$$\tau_{\mathrm{d}} = \alpha_1 Gb\sqrt{\rho_{\mathrm{i}}} + \alpha_2 Gb\left[\frac{1}{\delta} + \frac{1}{D}\right] \tag{3.36}$$

The transition from stage II to stage III, for most commercial alloys, is difficult to distinguish *i.e.* end of stage II and the start of stage III are not at the same points due to the effect of variable subgrain/grain sizes. Therefore Nes and Marthinsen (2002) modeled the transition of stage II to stage III in a stochastic manner. It is assumed that stage II ends when the recovery becomes significant while stage III starts when the dislocation density in the cell interior becomes constant. In the work of Nes and Marthinsen (2002); Nes *et al.* (2004) assume a statistical distribution of the subgrain sizes, from which they estimate the volume fraction, f_{sc}, of the largest subgrains where the recovery is small and the stage II scaling behavior still holds. More details are given in Nes *et al.* (2004). Then the unified relation for stress contribution due to stored dislocations with statistical distribution of subgrain sizes in different stages of work hardening are given by

$$\tau_{\mathrm{d}} = \alpha_1 Gb\left[\Gamma_1\left(\frac{q_{\mathrm{c}}}{\delta\sqrt{\rho_{\mathrm{i}}}}\right)\sqrt{\rho_{\mathrm{i}}} + \Gamma_2\left(\frac{q_{\mathrm{c}}}{\delta\sqrt{\rho_{\mathrm{i}}}}\right)\frac{q_{\mathrm{c}}}{\delta}\right] + \hat{\alpha}_2 Gb\left[\Gamma_2(0)\frac{1}{\delta} + \frac{1}{D}\right] \tag{3.37}$$

with

$$\hat{\alpha}_2 = f_{\mathrm{sc}}\alpha_2^{\mathrm{sc}} + (1 - f_{\mathrm{sc}})\alpha_2 \tag{3.38}$$

where

$$\alpha_2^{\mathrm{sc}} = \alpha_1 f(q_{\mathrm{b}} - 1)q_{\mathrm{c}} \tag{3.39}$$

and

$$f_{\mathrm{sc}} = \frac{1 - \Gamma_1\left[\frac{q_{\mathrm{c}}}{\delta\sqrt{\rho_{\mathrm{i}}}}\right]}{1 - \Gamma_1(1)} \tag{3.40}$$

Here the functions Γ_1 and Γ_2 are the statistical distributions of subgrains and are given as follows

$$\Gamma_1(x) = \frac{\int_0^x x^3 \mathrm{f}(x)\mathrm{d}x}{\int_0^\infty x^3 \mathrm{f}(x)\mathrm{d}x} = 1 - \exp(-5x)\sum_{n=0}^{7}\frac{(5x)^n}{n!} \tag{3.41}$$

and

$$\Gamma_2(x) = \frac{\int_x^\infty x^2 \mathrm{f}(x)\mathrm{d}x}{\int_0^\infty x^3 \mathrm{f}(x)\mathrm{d}x} = \frac{5}{7}\exp(-5x)\sum_{n=0}^{6}\frac{(5x)^n}{n!} \tag{3.42}$$

with $\mathrm{f}(x) = \frac{5^5 x^4}{24}\exp(-5x)$ and $x = \left(\frac{q_c}{\delta\sqrt{\rho_i}}\right)$.

In applications of the model the stress tensor at a macroscopic continuum scale is required representing contributions from many grains of various crystallographic orientation and microstructure. The equivalent flow stress and strain can be calculated as

$$\sigma_\mathrm{f} = M\tau \qquad \text{and} \qquad \varepsilon^\mathrm{p}_\mathrm{eq} = \gamma/M \tag{3.43}$$

Here M is the Taylor orientation factor translating the effect of the resolved shear stress in different slip systems into effective stress and strain quantities. It depends on the crystal structure and is affected by texture. However, in sheet forming operations the texture changes are small and the texture can be captured by one of the advanced phenomenological anisotropic yield functions presented in previous sections, providing a computational cost-effective approach.

In the implementation of the Nes hardening model within an implicit finite element code the hardening coefficient h is required, *i.e.* the slope on the hardening curve.

$$h = \frac{\mathrm{d}\sigma_\mathrm{f}}{\mathrm{d}\varepsilon^\mathrm{p}_\mathrm{eq}} = M^2\frac{\mathrm{d}\tau}{\mathrm{d}\gamma} = M^2\left(\frac{\mathrm{d}\tau_\mathrm{a}}{\mathrm{d}\gamma} + \frac{\mathrm{d}\tau_\mathrm{t}}{\mathrm{d}\gamma}\right) \tag{3.44}$$

Where $\frac{\mathrm{d}\tau_\mathrm{a}}{\mathrm{d}\gamma}$ and $\frac{\mathrm{d}\tau_\mathrm{t}}{\mathrm{d}\gamma}$ can be written as follows.

In Equation (3.31) for the athermal stress contribution, the relations for τ_p and τ_cl are constant with respect to the microstructure evolution. Therefore, $\frac{\mathrm{d}\tau_\mathrm{a}}{\mathrm{d}\gamma} = \frac{\mathrm{d}\tau_\mathrm{d}}{\mathrm{d}\gamma}$ and is given by:

$$\frac{\mathrm{d}\tau_\mathrm{a}}{\mathrm{d}\gamma} = \frac{\partial\tau_\mathrm{a}}{\partial\rho_\mathrm{i}}\frac{\partial\rho_\mathrm{i}}{\partial\gamma} + \frac{\partial\tau_\mathrm{a}}{\partial\delta}\frac{\partial\delta}{\partial\rho_\mathrm{i}}\frac{\partial\rho_\mathrm{i}}{\partial\gamma} \tag{3.45}$$

and the expression for the thermal stress given in Equation (3.30), is a function of three microstructural evolution parameters, ρ_i, δ and φ through Equation (3.28). Then,

$$\frac{\mathrm{d}\tau_\mathrm{t}}{\mathrm{d}\gamma} = \frac{\partial\tau_\mathrm{t}}{\partial\dot{\gamma}}\frac{\partial\dot{\gamma}}{\partial\gamma} + \frac{\partial\tau_\mathrm{t}}{\partial\rho_\mathrm{i}}\frac{\partial\rho_\mathrm{i}}{\partial\gamma} + \frac{\partial\tau_\mathrm{t}}{\partial\delta}\frac{\partial\delta}{\partial\rho_\mathrm{i}}\frac{\partial\rho_\mathrm{i}}{\partial\gamma} + \frac{\partial\tau_\mathrm{t}}{\partial\varphi}\left(\frac{\partial\varphi}{\partial\rho_\mathrm{i}} + \frac{\partial\varphi}{\partial\delta}\frac{\partial\delta}{\partial\rho_\mathrm{i}}\right)\frac{\partial\rho_\mathrm{i}}{\partial\gamma} \tag{3.46}$$

In the above relations, $\frac{\partial\rho_\mathrm{i}}{\partial\gamma}$, $\frac{\partial\delta}{\partial\gamma}$ and $\frac{\partial\varphi}{\partial\gamma}$ are obtained from the microstructure evolution equations, (3.48)–(3.50). $\frac{\partial\tau_\mathrm{a}}{\partial\rho_\mathrm{i}}$ and $\frac{\partial\tau_\mathrm{a}}{\partial\delta}$ are obtained by differentiating the athermal stress relation, τ_a with respect to state variables ρ_i and δ given in Section B.1.

Similarly, $\frac{\partial\tau_\mathrm{t}}{\partial\rho_\mathrm{i}}$, $\frac{\partial\tau_\mathrm{t}}{\partial\delta}$ and $\frac{\partial\tau_\mathrm{t}}{\partial\varphi}$ are obtained by differentiating the thermal stress relation, τ_t with respect to state variables ρ_i, δ and φ respectively and are given in Section B.2.

The relation $\frac{\partial \dot{\gamma}}{\partial \gamma}$ is obtained from the fact that in incremental analysis the equivalent plastic strain rate is defined by the equivalent plastic strain increment:

$$\dot{\gamma} = \frac{\Delta\gamma}{\Delta t} \Rightarrow \frac{\partial \dot{\gamma}}{\partial \gamma} = \frac{1}{\Delta t} \tag{3.47}$$

where $\Delta\gamma$ is the equivalent plastic strain increment and Δt is the time step of the incremental analysis, which are input parameters in a finite element simulation.

3.6.2 Microstructure Evolution

In order to provide a realistic description of the microstructure evolution the problems of athermal storage of dislocations and their annihilation by dynamic recovery need to be solved. In the present multi-parameter microstructural description this implies that the evolution equations must be properly defined and solved. On the basis of the treatments of Nes (1998); Marthinsen and Nes (2001); Nes and Marthinsen (2002), these evolution equations can be written in compact form as follows

$$\frac{\mathrm{d}\rho_\mathrm{i}}{\mathrm{d}\gamma} = \frac{1}{\left(1 + f(q_\mathrm{b}^2 - 1)\right)} \frac{2}{bL_\mathrm{eff}} - \frac{\rho_\mathrm{i} v_\rho}{\dot{\gamma}} \tag{3.48}$$

$$\frac{\mathrm{d}\delta}{\mathrm{d}\gamma} = -\frac{2\delta^2\rho_\mathrm{i}}{\kappa_0\varphi} \frac{SL^2}{L_\mathrm{eff}} + \frac{b v_\delta}{\dot{\gamma}} \tag{3.49}$$

$$\frac{\mathrm{d}\varphi}{\mathrm{d}\gamma} = g\left(\rho_\mathrm{i}, \delta, \varphi\right) \tag{3.50}$$

Equations (3.48) and (3.49) represent the combined effect of athermal storage of dislocations (first term on the right-hand side in these equations) and their dynamic recovery (second term).

Athermal storage of the dislocations. In the storage terms, L_eff is the effective slip length, the average radius the dislocation loops expand before being stored. It is determined by interactions between the mobile and the stored dislocations in the dislocation forest. If there are no other barriers than the dislocations stored in the Frank network this length scales with the spacing between the stored dislocations:

$$L_\rho = \frac{C}{\sqrt{\rho}} \tag{3.51}$$

Here C is a statistical parameter proportional to the chance for a dislocation to become stored in the Frank network. C remains constant for a given alloy but depends on the solute content. However, in most commercial aluminum alloys, other barriers will also be present like grain boundaries and precipitate particles. These barriers will also impede mobile dislocations and affect the athermal storage rate. The presence of grain boundaries and particles reduces the slip length and are taken into account by the following relation

$$\left[\frac{1}{L_\mathrm{eff}}\right]^2 = \left[\frac{1}{L_\rho}\right]^2 + \left[\frac{1}{L_\mathrm{p}}\right]^2 + \left[\frac{1}{L_\mathrm{D}}\right]^2 \tag{3.52}$$

with

$$L_{\mathrm{p}} = \frac{r/2f_{\mathrm{r}}}{\kappa_3}, \quad L_{\mathrm{D}} = \frac{D}{\kappa_2}$$

Here κ_2 and κ_3 are constants accounting for geometrical shapes and the measuring methods applied and expected to be of the order of unity. L_{p} and L_{D} represent the slip length contributions due to precipitate particles and grain size (D) respectively. In Equation (3.48), the first term represents the athermal storage in the newly formed subgrain boundaries S is a cell/subboundary storage parameter, for more details see Marthinsen and Nes (2001); Nes and Marthinsen (2002).

Dynamic recovery. The last terms in Equations (3.48) and (3.49) represent, respectively, the dynamic recovery effects on the dislocation density inside the cell ρ_{i}, and the subgrain size, δ. In other words, the dynamic recovery is incorporated by analyzing the stability of the cell interior dislocations ρ_{i} in terms of the *recovery* in the *Frank network* and the subboundary structure in terms of *subgrain growth*.

In Equation (3.48), the second term in principle defines the rate controlling annihilation frequency of the dislocations inside the subgrain. For aluminum alloys, the annihilation frequency can be written in the following form:

$$v_\rho = \sqrt{\rho_{\mathrm{i}}} l_\rho \xi_\rho B_\rho \nu_{\mathrm{D}} \exp\left(-\frac{U^*}{kT}\right) 2\sinh\left(\frac{V_\rho G b \sqrt{\rho_{\mathrm{i}}}}{2\pi kT}\right) \tag{3.53}$$

where $l_\rho \approx b c_{\mathrm{sc}}^{e_\rho - 1}\omega^{-1}$, $U^* = U_{\mathrm{s}} + \Delta U_{\mathrm{s}}$, and $V_\rho \propto \xi_\rho b^3 \omega c_{\mathrm{sc}}^{-e_\rho}$. Here, l_ρ is an activation length, c_{sc} is the solute concentration at the dislocation core, ω is a constant (≈ 1) and e_ρ is a constant of value in the range from 0.5 to 1. U_{s} is the activation energy for diffusion of solute atoms and ΔU_{s} is the interaction energy between the solute atoms and the dislocation. For a detailed analysis of dynamic recovery of subgrain interior dislocations, see (Nes, 1994; Nes and Marthinsen, 2002).

The last term in Equation (3.49) contains a velocity term corresponding to the growth rate for a given subgrain size. The average subgrain size in a dynamic situation will increase at a rate

$$\frac{\mathrm{d}\delta^+}{\mathrm{d}t} = \dot{\gamma}\frac{\mathrm{d}\delta^+}{\mathrm{d}\gamma} = b v_\delta = b\nu_{\mathrm{D}} B_\delta \exp\left(-\frac{U^*}{kT}\right) 2\sinh\left(\frac{P V_\delta}{kT}\right) \tag{3.54}$$

where B_δ is a constant, and the driving pressure is given by $P = 4\gamma_{\mathrm{sb}}/\delta$, ($\gamma_{\mathrm{sb}}$ is the subboundary energy), V_δ is an activation volume, $V_\delta \propto b^3 c_{\mathrm{sc}}^{-e_\delta}\xi_\delta$, where ξ_δ is a stress intensity factor which needs to be determined from experiments, for details see (Marthinsen and Nes, 2001; Nes and Marthinsen, 2002).

The misorientation aspect. When dislocations are consumed by the sharpening of old boundaries they are stored in a way that does not contribute to the hardening of the material. To handle this aspect in the Nes model, the following empirical equation based on physical observations is used:

$$\frac{\mathrm{d}\varphi}{\mathrm{d}\gamma} = \left[f_{\mathrm{II}}\frac{bK_{\mathrm{II}}}{\varphi L_{\mathrm{eff}}} + (1 - f_{\mathrm{II}})\, K_{\mathrm{III}}\right]\left[1 - \left(\frac{\varphi}{\varphi_{\mathrm{IV}}}\right)^3\right] \tag{3.55}$$

Here f_{II} must equal unity during Stage II and vanish at larger strains:

$$f_{\mathrm{II}} = \left[\frac{\delta\sqrt{\rho_{\mathrm{i}}}}{q_{\mathrm{c}}}\right]^{15} \tag{3.56}$$

In warm deformation the increase of the misorientation occurs more rapidly:

$$K_{\mathrm{III}} = \begin{cases} 0.02 & T \leq 300K \\ 0.02(T/300)^2 & T > 300K \end{cases} \tag{3.57}$$

For more details, see (Marthinsen and Nes, 2001; Nes and Marthinsen, 2002).

3.6.3 Dynamic Strain Ageing

Al–Mg alloys are known to exhibit negative strain rate sensitivity due to dynamic strain ageing (DSA), causing instabilities that influence their formability and lead to serrated flow curves. This behavior is known as Portevin–Le Chatelier effect and it can lead to so-called stretcher lines in a product which are unfavorable for visible parts. The DSA effect is also included as a sub-model into the framework of a microstructure-based work hardening Nes model. Extensive presentations of this sub-model are given by Holmedal *et al.* (2005a,b).

The material strengthening is due to the diffusion of Mg solute atoms towards the dislocation core. Mg easily diffuses and has a high solubility in the matrix. Whenever there is sufficient time for diffusion to occur, the effective solute concentration near the dislocation cores c_{sc} becomes higher than in the matrix, c. When the dislocations move there might not be enough time for a complete diffusion process. Only if they move sufficiently fast or diffusivity of Mg is very low, $c_{\mathrm{sc}} = c$. The dislocation velocity is given by the Orowan relation $v = \dot{\gamma}/b\rho_{\mathrm{m}}$ and the diffusivity of Mg is expressed as:

$$D = B_{\mathrm{sc}} b^2 \nu_{\mathrm{D}} \exp\left(\frac{\Delta U_{\mathrm{sc}}}{kT}\right) \tag{3.58}$$

Here B_{sc} is a constant, and U_{sc} is the activation energy for diffusion of Mg solute atoms in aluminum. If there is sufficient time for diffusion, the Mg concentration at the dislocation core reaches a steady state value:

$$c_{\mathrm{ss}} = c \exp\left(\frac{\Delta U_{\mathrm{sc}}}{kT}\right) \tag{3.59}$$

ΔU_{sc} is the interaction energy between the solute atoms and the dislocation core. Here, it is required to balance the effect of diffusion by the effect of the dislocation movements. A simple approach developed by Holmedal *et al.* (2005b) is to balance the dislocation speed and a dimensional estimate for the velocity related to the diffusion: D/bv. If this ratio is large the diffusion will dominate, if it is low the dislocations have time to escape the diffusion. In the model, it is assumed that the effective Mg concentration at the dislocation core, c_{sc}, can be expressed solely by this parameter, as follows.

$$c_{\mathrm{sc}} = c_0 + c + (c_{\mathrm{ss}} - c)\left\{1 - \exp\left[-\left(\frac{D}{bv}\right)^{n_{\mathrm{sc}}}\right]\right\} \tag{3.60}$$

Here n_{sc} is a constant in the range between zero and unity. Equations (3.58)–(3.60) constitute a model for the Mg solute concentration near the dislocation core in Al–Mg alloys. The flow stress is affected by c_{sc}, Mg solute concentration at the dislocation core, through the thermal stress component after Equation (3.30). The microstructure evolution is affected through the dynamic recovery of dislocations in the Frank network and the subgrain growth (after Equations (3.48)–(3.49)).

Table 3.1: Parameters for the extended Nadai model.

T_m	800	a_1	134.2	n_0	0.3117
ε_0	0.004118	a_2	3.669	m_0	0.001236
$\dot{\varepsilon}_0$	0.002	b_1	0.2086	c	12.42
C_0	491.7	b_2	1.698		

3.7 Validation of Work Hardening Models for Warm Forming

In this section, the suitability of work hardening models presented in the previous section is investigated by comparing the results for uniaxial tensile tests on 5754-O alloy as representative example of aluminum alloys at various temperatures with constant strain rates and also with the strain rate jumps.

Extended Nadai Model parameters of the extended Nadai model were fitted simultaneously to uniaxial tensile tests, in the temperature range of 25 °C and 250 °C and at strain rates of $0.002\,s^{-1}$ and $0.02\,s^{-1}$. This resulted in the values for 9 fitted parameters and 2 fixed parameters (T_m and $\dot{\varepsilon}_0$) presented in Table 3.1.

Bergström Model In the case of Bergström model, some of the parameters can be selected beforehand, such as the initial dislocation density ρ_0, the magnitude of Burgers vector, the scaling parameter α and the shear modulus at room temperature G_{ref} were taken from the literature. The remaining 8 parameters were determined by a least squares approximation of eight uniaxial tensile test results as used to fit the extended Nadai model. It resulted in the values presented in Table 3.2.

Nes Model The Nes model relies on a multi-parameter microstructure description, from which it follows that a lot of parameters are unavoidable. In their works of Nes and co-workers, the parameters of the model have been tuned to fit a large number of experiments covering a wide range of alloys, temperature and strain rates (Nes, 1998; Marthinsen and Nes, 2001). However, only a few of these parameters are fitting ones in the true meaning of that word. In the works of Nes and co-workers consider the parameters involved are of four types.

Table 3.2: Parameters for the Bergström model.

σ_0	109.3 MPa	m	0.422	ρ_0	$10^{11}\,m^{-1}$
α	1.0	U_0	$6.093 \cdot 10^8\,m^{-1}$	G_{ref}	26354 MPa
b	$2.857 \cdot 10^{-10}$ m	Ω_0	23.63	C_T	38.45
C	$3.3422 \cdot 10^5$	Q_v	$1.0917 \cdot 10^5$ J/mol	T_1	2975 K

Table 3.3: Parameters for the Nes model.

ν_D	$1.0 \cdot 10^{13}\,\mathrm{s}^{-1}$	b	$2.86 \cdot 10^{-10}\,\mathrm{m}$	κ	$1.3 \cdot 10^{-23}\,\mathrm{J/K}$
q_c	12.3	C	34.85	f	0.1
α_1	0.3	α_2	3.5	κ_0	$3.0\,\mathrm{m}^{-1}$
U_s	160000 J/mol	U_{sd}	160000 J/mol	ΔU_s	0.0 J/mol
κ_2	2.0	κ_3	1.5	φ_c	0.3489
B_t	57.0	ω_ρ	1144.0	ω_t	20.0
e_t	1.0	B_ρ	0.23	ξ_ρ	118.2
ω_s	1.0	e_ρ	0.67	B_δ	100.0
ξ_δ	40.0	e_δ	0.65	ρ_0	$1.0 \cdot 10^{11}\,\mathrm{m}^{-1}$
S_{IV}	0.15	q_{IV}	2.0	φ_{IV}	0.052 rad

Physical parameters such as activation energies and volumes and pre-exponential constants: the number of such physically necessary constants follows from the complexities of the model, defined by the dislocation dynamics involved. While the activation energy and volumes in principle were determined experimentally (independent of model tuning), the pre-exponential constants are adjustable parameters and are determined as part of an experimental tuning procedure.
Stereological constants such as the scaling parameter q_c and misorientation parameter, the volume fraction of cell walls f in stage II and ϕ_IV were determined experimentally by careful TEM examination of different Al alloys.
Empirical constants such as the flow stress parameters α_1 and α_2, the athermal storage parameters κ_2 and κ_3 were determined independently of the tuning of the model.
Fitting parameters are the microstructure evolution parameter S_IV, the athermal storage parameter C and the stress intensity factors in dynamic recovery, ξ_ρ and ξ_δ were determined by a least square approximation of eight uniaxial tensile test results as used to fit the extended Nadai and Bergström models.
In addition, the various equations contain the obvious material and physical constants such as the shear modulus, G, magnitude of the Burgers vector, b, the Boltzmann constant, k and the Debye frequency ν_D are taken from literature. Also the Nes model directly takes into account the chemical composition, grain size, volume fraction and size of particles. The chemical composition of the investigated AA 5754-O alloy is (Mg: 3.356 %, Si: 0.130 %, Cu: 0.01 %, Mn: 0.32 %, Ti: 0.009 % with remaining Al) with the average grain size of $20 - 25\mu m$. The selected and fitted parameters are presented in Table 3.3.

In Figure 3.6(a) and Figure 3.6(b), the simulated engineering stress–strain curves are plotted for the Nes model, together with experimental data for various temperatures and strain rates. In Figure 3.6(c) and Figure 3.6(d), the experimental stress–strain results are compared with the Bergström hardening model and the phenomenological extended Nadai model. It can be seen that all the models are more or less capable of describing the trends at various temperatures and strain rates. But the Nes model clearly improves the results compared to Bergström and Nadai models. Note that the comparison is only valid for a uniform strain, which means up to the maximum engineering stress. The necking regime is investigated in Chapter 4.

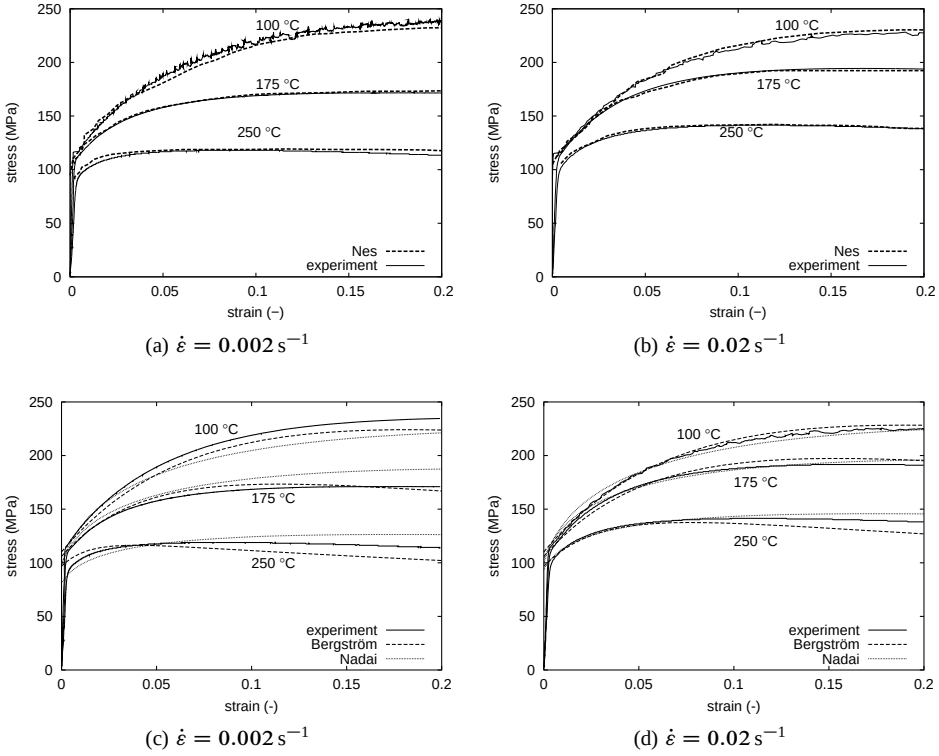

(a) $\dot{\varepsilon} = 0.002\,\mathrm{s}^{-1}$ (b) $\dot{\varepsilon} = 0.02\,\mathrm{s}^{-1}$

(c) $\dot{\varepsilon} = 0.002\,\mathrm{s}^{-1}$ (d) $\dot{\varepsilon} = 0.02\,\mathrm{s}^{-1}$

Figure 3.6: Engineering stress–strain curves—experiments and the different models.

Although the models yield more or less similar stress–strain curves for constant strain rate simulations, the predictions are completely different if a jump in the strain rate is simulated. In Figure 3.7, the stress–strain curves are plotted for deformation at 175 °C and 250 °C and for strain rates of $0.002\,\mathrm{s}^{-1}$ and $0.02\,\mathrm{s}^{-1}$. If strain rate changes from $0.002\,\mathrm{s}^{-1}$ to $0.02\,\mathrm{s}^{-1}$ or from $0.02\,\mathrm{s}^{-1}$ to $0.002\,\mathrm{s}^{-1}$ are applied after a strain of 5 %, the Nadai model immediately follows the curve corresponding to a constant strain rate. With the Bergström model the constant strain rate curve is only slowly approached after continuous straining. With the Nes model, an initial jump in the flow stress is observed, followed by slowly approaching the constant strain rate curve, which is a better representation of the experiments.

From the experimental stress–strain curves shown in Figure 3.8(a), with different strain rates and at a temperature of 100 °C, the lowest strain rate yields the highest stresses and the highest strain rate yields the lowest stresses. This observation is often presented as a negative strain rate sensitivity of aluminum alloys and is attributed to dynamic strain ageing. In Figure 3.8(b), even though the difference is small, it is clearly observed that the Nes model can represent the negative strain rate sensitivity of Al–Mg alloys at low temperatures, whereas this behavior cannot be described with the Bergström model (both strain rate curves coincide) as shown in Figure 3.8(c).

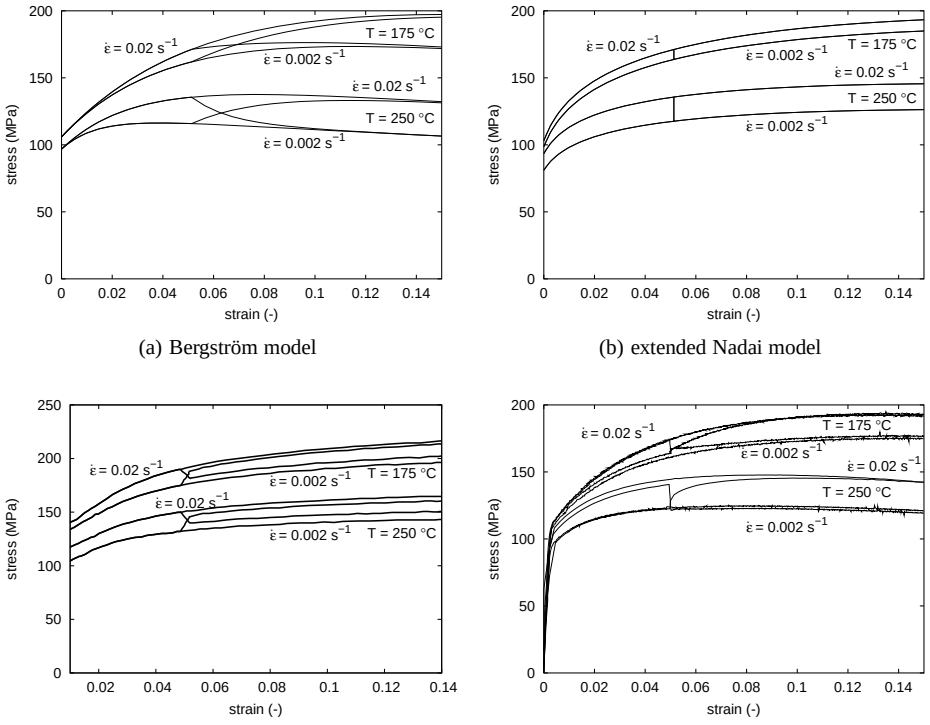

(a) Bergström model

(b) extended Nadai model

(c) Nes model

(d) experiments

Figure 3.7: True stress–strain curves with and without strain rate jumps.

3.8 Large Deformation Analysis

The material models described in the previous sections are based on logarithmic (true) stresses and strains. For simple, proportional logarithmic (true) strain path, the set of three principal axes of stretching is fixed with respect to the material and the logarithms of the principal stretches remain in a fixed ratio. For a general description of large deformations, however, this description is no longer applicable (Yoon *et al.*, 1999; Van den Boogaard *et al.*, 2000). The extension of rate constitutive equations to general large deformations requires the use of *objective* formulations (Belytschko *et al.*, 2006) described in Appendix A.

In the objective formulations, large rotations are accounted for by rotating the stress tensor. For anisotropic material behavior, not only the stresses, but also the relation between stress rate and strain rate must be updated. In this case it is easier to use a co-rotating reference frame and apply the constitutive relations on a strain measure that is neutralized for rigid body rotations.

Thus, planar anisotropic axes are updated using an algorithm based on the polar decomposition of the deformation gradient tensor:

$$\mathbf{F} = \mathbf{RU} \tag{3.61}$$

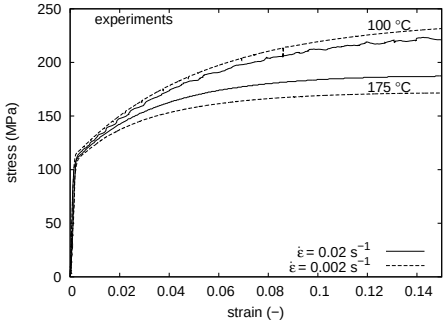

(a) Experimental

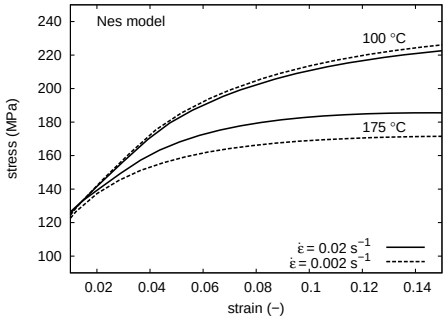

(b) Nes hardening model

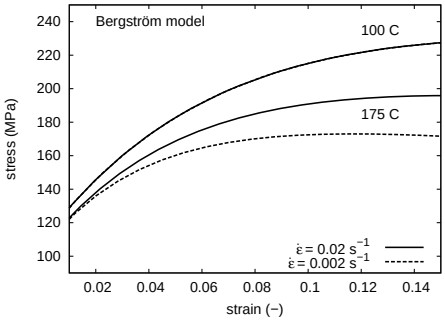

(c) Bergström hardening model

Figure 3.8: Strain rate influence on stress–strain curves—comparison between models.

The material rotation tensor $\mathbf{R}_\mathrm{m}$ is used to formulate the stress–strain behavior in a co-rotating reference frame and the logarithm of the stretch tensor $\ln \mathbf{U}$ is used as a strain measure (the Hencky strain). The decomposition can be performed on the total deformation gradient or on the incremental deformation gradient.

Total algorithm: In this case, the rotation tensor directly determines the rotation of the material. The deformation part, however, must be given in an incremental way, in order to follow the strain path.

$$\mathbf{F}_1 = \mathbf{R}_1\mathbf{U}_1 \qquad \mathbf{F}_0 = \mathbf{R}_0\mathbf{U}_0 \tag{3.62a}$$

$$\mathbf{R}_{\mathrm{m}1} = \mathbf{R}_1 \qquad \Delta\boldsymbol{\varepsilon} = \ln \mathbf{U}_1 - \ln \mathbf{U}_0 \tag{3.62b}$$

Incremental algorithm: If the polar decomposition is performed on the incremental deformation gradient $\mathbf{F}_0^1$, the material rotation $\mathbf{R}_\mathrm{m}$ must be updated at every increment. The incremental deformation gradient is the deformation gradient at the end of the increment with respect to the configuration at the start of the increment. The strain increment is now

only determined by the change of the current configuration.

$$\mathbf{F}_1 = \mathbf{F}_0^1 \mathbf{F}_0 \qquad \mathbf{F}_0^1 = \mathbf{R}_0^1 \mathbf{U}_0^1 \tag{3.63a}$$

$$\mathbf{R}_{\mathrm{m}1} = \mathbf{R}_0^1 \mathbf{R}_{\mathrm{m}0} \qquad \Delta\boldsymbol{\varepsilon} = \ln \mathbf{U}_0^1 \tag{3.63b}$$

Tests with both models on large shear deformations indicate that the incremental algorithm gives results comparable to the use of the Jaumann derivative (Van den Boogaard *et al.*, 2000).

3.9 Numerical Implementation

In this section the implementation of material models in a finite element program is discussed. The three main tasks of a constitutive subroutine for elasto-plasticity in an FEM code are:

- Yield criterion calculation (elastic-to-plastic and plastic-to-elastic transition), presented in Section 3.2.
- Updating the stress state and internal variables for a given total strain increment (Section 3.3).
- Calculation of a consistent constitutive matrix.

If the full implicit Newton–Raphson procedure is executed for equilibrium iterations, the consistent constitutive matrix is required in the computation of the tangent stiffness matrix to achieve asymptotic 2nd order rate of convergence. However, the consistency of the constitutive matrix is not important in the explicit FE solvers where no Newton-Raphson iterations are used. There exist a number of algorithms and techniques to update the stresses and plastic strains, such as forward Euler scheme, generalized trapezoidal or mid-point algorithms, a backward Euler (return map) scheme. In this work the implicit, backward Euler algorithm was chosen.

3.9.1 Stress Update

The return map stress update algorithm is constructed in two steps. First, the so-called trial state is defined as the state of stress when the given total strain increment is taken as elastic and zero plastic strain increment is assumed (elastic predictor step). Second step is the plastic corrector step: the trial stress is projected back onto the yield stress in the direction of the closest projection. According to the implicit backward Euler approach the plastic strain increment is computed in the *updated configuration*, which depends on the updated stresses to be determined. In the heart of the return mapping algorithm for the isotropic hardening case is the calculation of the equivalent plastic strain increment (plastic multiplier) using the condition that the stress remains on the yield surface:

$$\phi = \sigma_{\mathrm{eq}}\left(\boldsymbol{\sigma}_{n+1}\right) - \sigma_{\mathrm{f}}\left(\varepsilon^{\mathrm{p}}_{\mathrm{eq}\,n+1}\right) \tag{3.64}$$

where n denotes the increment number. Now the stress increment is first calculated by assuming that the strain increment $\Delta\boldsymbol{\varepsilon}$ is completely elastic:

$$\Delta\boldsymbol{\sigma} = \mathbf{E} : \Delta\boldsymbol{\varepsilon} \tag{3.65}$$

A trial stress is determined based on the stress increment:

$$\boldsymbol{\sigma}^{\mathrm{tr}} = \boldsymbol{\sigma}_n + \Delta\boldsymbol{\sigma} \tag{3.66}$$

If this results in a stress state outside the yield surface ($\varphi > 0$), then the stress state has to be mapped back to the yield surface, indicating the name *Return Mapping Algorithm*. To construct a residual function for the RMA, Equation (3.65) is rewritten:

$$\Delta\boldsymbol{\sigma} = \mathbf{E} : (\Delta\boldsymbol{\varepsilon} - \Delta\boldsymbol{\varepsilon}^{\mathrm{p}}) \tag{3.67}$$

The direction of plastic strain increment $\Delta\boldsymbol{\varepsilon}^{\mathrm{p}}$ depends on the local derivative of the yield surface, *i.e.* the normality principle (3.1) in incremental form can be written as:

$$\Delta\boldsymbol{\varepsilon}^{\mathrm{p}} = \Delta\lambda \left.\frac{\partial\phi}{\partial\boldsymbol{\sigma}}\right|_{n+1} \tag{3.68}$$

Now Equation (3.65) can be elaborated as:

$$\Delta\boldsymbol{\varepsilon} \quad = \quad \mathbf{E}^{-1} : \Delta\boldsymbol{\sigma} + \Delta\lambda \left.\frac{\partial\varphi}{\partial\boldsymbol{\sigma}}\right|_{n+1} \tag{3.69}$$

To solve the above set of equations, they are casted in to a set of 2 residual functions:

$$\mathbf{r}_\sigma \quad = \quad \Delta\boldsymbol{\varepsilon} - \mathbf{E}^{-1} : \Delta\boldsymbol{\sigma} - \Delta\lambda \left.\frac{\partial\phi}{\partial\boldsymbol{\sigma}}\right|_{n+1} \tag{3.70}$$

$$r_\phi \quad = \quad -\left(\sigma_{\mathrm{eq}} - \sigma_{\mathrm{f}}\right) \tag{3.71}$$

The two residual functions are combined to $\mathbf{r} = \left\{\mathbf{r}_\sigma, r_\phi\right\}^{\mathrm{T}}$. For ease of use in solving the state variables $\Delta\boldsymbol{\sigma}$, $\Delta\lambda$, the residual equations are written in matrix-vector form, *i.e.* the vector with the state variables is written as:

$$\{\mathbf{v}\} = \begin{Bmatrix} \Delta\boldsymbol{\sigma} \\ \Delta\lambda \end{Bmatrix} \tag{3.72}$$

The equations are nonlinear and require an iterative procedure to find $\mathbf{v}^{\mathrm{n+1}}$. A Taylor series expansion is used, which is evaluated as:

$$\mathbf{r}\left(\Delta\mathbf{v}^{n+1}\right) \approx \mathbf{r}\left(\Delta\mathbf{v}^{i}\right) + \frac{\partial\mathbf{r}}{\partial\mathbf{v}^{i}}\,\mathrm{d}\mathbf{v}^{i} = \mathbf{0} \tag{3.73}$$

$$\Longrightarrow\ \mathrm{d}\mathbf{v}^{i} = -\left(\frac{\partial\mathbf{r}}{\partial\mathbf{v}^{i}}\right)^{-1}\mathbf{r}\left(\Delta\mathbf{v}^{i}\right) \tag{3.74}$$

The derivatives of the residual functions are used to construct the Jacobian of this set of equations.

$$\mathbf{J} = \begin{bmatrix} \mathbf{E}^{-1} + \Delta\lambda \dfrac{\partial^2 \phi}{\partial \boldsymbol{\sigma}_{n+1}^2} & \dfrac{\partial \phi}{\partial \boldsymbol{\sigma}_{n+1}} \\ \dfrac{\partial \phi^{\mathrm{T}}}{\partial \boldsymbol{\sigma}_{n+1}} & \dfrac{\partial \phi}{\partial \lambda} \end{bmatrix} \tag{3.75}$$

with

$$\frac{\partial \phi}{\partial \lambda} = \frac{\partial \phi}{\partial \sigma_{\mathrm{f}}} \frac{\partial \sigma_{\mathrm{f}}}{\partial \varepsilon_{\mathrm{eq}}^{\mathrm{p}}} \frac{\partial \varepsilon_{\mathrm{eq}}^{\mathrm{p}}}{\partial \lambda} \tag{3.76}$$

$$\frac{\partial \phi}{\partial \boldsymbol{\sigma}_{n+1}} = \frac{\partial \sigma_{\mathrm{eq}}}{\partial \boldsymbol{\sigma}_{n+1}} \tag{3.77}$$

and

$$\frac{\partial \phi}{\partial \sigma_{\mathrm{f}}} = -1 \tag{3.78}$$

Figure 3.9 shows schematically the loop that describes the RMA. The presented RMA often fails to achieve local convergence, particularly for strain rate dependent hardening models. For instance, if the plastic strain increment in the stress update is too small then the thermal part of the physically based models are going to vanish and if the plastic strain increment is too large then the thermal stress contribution is maximum. In this condition, the Newton–Raphson procedure becomes unstable by *swapping* between two solutions. Often line search can improve the convergence of the common Newton–Raphson iterations by scaling of the iterative increments. The same procedure is adopted here to solve the problem of oscillating between two solutions. Figure 3.10 shows schematically the adopted procedure.

The algorithm presented here is not dependent on the chosen yield function and isotropic hardening model. To implement a particular yield function in this return mapping algorithm, the first and second derivative with respect to the stress are required. For the isotropic hardening model, only a function evolution and the derivative with respect to the equivalent plastic strain is required.

3.9.2 Stiffness Matrix

On the global level of finite element formulation, the stiffness matrix at the material points is required. The local stiffnesses are then assembled to get the global stiffness of the structure. The stiffness matrix can easily be calculated by applying a perturbation method to the residual matrix-vector relation, *i.e.*

$$\begin{bmatrix} \mathbf{E}^{-1} + \Delta\lambda \dfrac{\partial^2 \phi}{\partial \boldsymbol{\sigma}^2} & \dfrac{\partial \phi}{\partial \boldsymbol{\sigma}} \\ \dfrac{\partial \phi}{\partial \boldsymbol{\sigma}}^{\mathrm{T}} & \dfrac{\partial \phi}{\partial \lambda} \end{bmatrix} \begin{Bmatrix} \delta\boldsymbol{\sigma} \\ \delta\lambda \end{Bmatrix} = \begin{Bmatrix} \delta\boldsymbol{\varepsilon} \\ 0 \end{Bmatrix} \tag{3.79}$$

1. Input: $\Delta\boldsymbol{\varepsilon}$
2. Initialize: $i = 0$, $\Delta\lambda = \Delta\varepsilon^{\mathrm{p}}_{\mathrm{eq}} = 0$
3. Compute trial state, flow stress and yield function:
   $\boldsymbol{\sigma}^{\mathrm{tr}} = \boldsymbol{\sigma}_n + \mathbf{E}\Delta\boldsymbol{\varepsilon}$, $\sigma_{\mathrm{f}} = \sigma_{\mathrm{f}}(\varepsilon^{\mathrm{p}}_{\mathrm{eq}}, \dot{\varepsilon}, \dots)$
   $\phi^{\mathrm{tr}} = \phi(\sigma_{\mathrm{eq}}(\boldsymbol{\sigma}^{\mathrm{tr}}), \sigma_{\mathrm{f}})$
4. Check yield condition:
   `IF` ($\phi^{\mathrm{tr}} < 0$) `THEN`
   elastic step: set $\boldsymbol{\sigma} = \boldsymbol{\sigma}^{\mathrm{tr}}$
   `EXIT`
   `ELSE`
   plastic step:
   `DO` $|r^i_\phi| > tol r_\phi$
5. Compute residual vector, $\{\mathbf{r}\}$ and Jacobian $[\mathbf{J}]$
   $\mathbf{r} = \mathbf{r}(\mathbf{r}_\sigma, r_\phi)$
   $\mathbf{J} = \mathbf{J}\left(\Delta\lambda, \dfrac{\partial\phi}{\partial\sigma_{\mathrm{f}}}, \dfrac{\partial\sigma_{\mathrm{f}}}{\partial\varepsilon^{\mathrm{p}}_{\mathrm{eq}}}, \dfrac{\partial\varepsilon^{\mathrm{p}}_{\mathrm{eq}}}{\partial\lambda}, \dfrac{\partial\phi}{\partial\boldsymbol{\sigma}}, \dfrac{\partial^2\phi}{\partial\boldsymbol{\sigma}^2}\right)$
6. Solve for $\Delta\lambda$, $\Delta\boldsymbol{\sigma}$
7. Update solution
   $\lambda = \lambda_0 + \Delta\lambda$, $\boldsymbol{\sigma} = \boldsymbol{\sigma}_0 + \Delta\boldsymbol{\sigma}$
   Increment iteration counter, $i = i + 1$
   `END DO`
   `END IF`

Figure 3.9: Iteration scheme for the return mapping algorithm.

From these equations $\delta\lambda$ is isolated:

$$\delta\lambda = -\left(\frac{\partial\phi}{\partial\lambda}\right)^{-1}\frac{\partial\phi}{\partial\boldsymbol{\sigma}}^{\mathrm{T}}\delta\boldsymbol{\sigma} \tag{3.80}$$

which is substituted back to obtain a relation between the stress and strain increment:

$$\begin{aligned}
\mathbf{E}^{-1}\delta\boldsymbol{\sigma} + \Delta\lambda\frac{\partial^2\phi}{\partial\boldsymbol{\sigma}^2}\delta\boldsymbol{\sigma} - \left(\frac{\partial\phi}{\partial\lambda}\right)^{-1}\frac{\partial\phi}{\partial\boldsymbol{\sigma}}\frac{\partial\phi}{\partial\boldsymbol{\sigma}}^{\mathrm{T}}\delta\boldsymbol{\sigma} &= \delta\boldsymbol{\varepsilon} \\
\Leftrightarrow \left[\mathbf{E}^{-1} + \Delta\lambda\frac{\partial^2\phi}{\partial\boldsymbol{\sigma}^2} - \left(\frac{\partial\phi}{\partial\lambda}\right)^{-1}\frac{\partial\phi}{\partial\boldsymbol{\sigma}}\frac{\partial\phi}{\partial\boldsymbol{\sigma}}^{\mathrm{T}}\right]\delta\boldsymbol{\sigma} &= \delta\boldsymbol{\varepsilon} \qquad (3.81) \\
\mathbf{K}^{-1}\delta\boldsymbol{\sigma} &= \delta\boldsymbol{\varepsilon} \qquad (3.82)
\end{aligned}$$

1. Input: $\Delta\boldsymbol{\varepsilon}$
2. Initialize: $i = 0, nlin\_srch, \Delta\lambda = \Delta\varepsilon^{\mathrm{p}}_{\mathrm{eq}} = 0$
3. Compute trial state, flow stress and yield function:
   $\boldsymbol{\sigma}^{\mathrm{tr}} = \boldsymbol{\sigma}_n + \mathrm{D}\Delta\boldsymbol{\varepsilon}$, $\sigma_{\mathrm{f}} = \sigma_{\mathrm{f}}(\varepsilon^{\mathrm{p}}_{\mathrm{eq}}, \dot{\varepsilon}, \dots)$
   $\phi^{\mathrm{tr}} = \phi(\sigma_{\mathrm{eq}}(\boldsymbol{\sigma}^{\mathrm{tr}}), \sigma_{\mathrm{f}})$
4. Check yield condition:
   IF ($\phi^{\mathrm{tr}} < 0$) THEN
   elastic step: set $\boldsymbol{\sigma} = \boldsymbol{\sigma}^{\mathrm{tr}}$
   EXIT
   ELSE
   plastic step:
   DO $|r^i_\phi| > tolr_\phi$
5. Compute residual vector, $\{\mathbf{r}\}$ and Jacobian $[\mathbf{J}]$
   $\mathbf{r} = \mathbf{r}(\mathbf{r}_\sigma, r_\phi)$
   $\mathbf{J} = \mathbf{J}\left(\Delta\lambda, \dfrac{\partial\phi}{\partial\sigma_{\mathrm{f}}}, \dfrac{\partial\sigma_{\mathrm{f}}}{\partial\varepsilon^{\mathrm{p}}_{\mathrm{eq}}}, \dfrac{\partial\varepsilon^{\mathrm{p}}_{\mathrm{eq}}}{\partial\lambda}, \dfrac{\partial\phi}{\partial\boldsymbol{\sigma}}, \dfrac{\partial^2\phi}{\partial\boldsymbol{\sigma}^2}\right)$
6. Solve for $\Delta\lambda$, $\Delta\boldsymbol{\sigma}$
7. Update solution
   $\lambda = \lambda_0 + \Delta\lambda, \boldsymbol{\sigma} = \boldsymbol{\sigma}_0 + \Delta\boldsymbol{\sigma}$
8. Compute r^j_ϕ
   DO $\left(|r^j_\phi| > |r^i_\phi|$ .and. $j \le nlin\_srch\right)$
   $\Delta\lambda = \Delta\lambda/2$ and $\Delta\boldsymbol{\sigma} = \Delta\boldsymbol{\sigma}/2$
   $\lambda = \lambda_0 + \Delta\lambda, \boldsymbol{\sigma} = \boldsymbol{\sigma}_0 + \Delta\boldsymbol{\sigma}$
   $j = j + 1$
   END DO
   Increment iteration counter, $i = i + 1$
   END DO
   END IF

Figure 3.10: Iteration scheme for the return mapping algorithm with line search.

With $\mathbf{K}$ denoting the tangent stiffness matrix.

3.10 Summary

Within the context of rate independent plasticity, the material model consists of two parts: the definition of yield surface and the work hardening. In this chapter, different material models for warm forming were introduced that will be used in the process simulations presented

in the next chapters. First, basics of rate independent plasticity were outlined. Two very accurate anisotropic yield functions: the Vegter and Barlat Yld2000 for the simulation of aluminum sheet forming were described.

For the description of work hardening at different temperatures and strain rates, a phenomenological extended Nadai and the physically based Bergström and Nes models were introduced. The physically based Bergström model is relatively simple and the microstructure evolution was described by one parameter. The Nes model uses more physical background to describe the plastic deformation. In the Nes model, microstructure evolution was described by three parameters. The alloy 5754-O was used as a representative example of aluminum alloys in order to compare the predictive power of different hardening models. It was shown that all models are more or less capable of describing the trends at various temperatures and strain rates. But the Nes model clearly improves the results compared to Bergström and Nadai models. The Nes model also represents the negative strain sensitivity behavior of Al–Mg alloys at temperatures below 125 °C. If the jump in the strain rate is considered, the extended Nadai model immediately follows the curve corresponding to a constant strain rate. With the Bergström model the constant strain rate curve is only slowly approached after continuous straining. With the Nes model, an initial jump in the flow stress is observed, followed by slowly approaching the constant strain rate curve, which is a better representation of the experiments.

For efficient numerical simulations using strain rate and temperature dependent material models, an accurate stress update algorithm within the context of implicit finite element scheme is required. For efficient and stable simulations, the Newton–Raphson iterations of return mapping algorithm has been adapted with line search criteria.

4. Warm Forming Applications

This chapter discusses the validation of the presented material models for warm forming by comparing model predictions with uniaxial tensile tests and warm deep drawing of cylindrical and square cups. The material models are implemented in the in-house implicit finite element code DiekA.

First, some of the uniaxial tensile tests that were used to determine the material parameters of AA 5754-O alloy are simulated. The simulations include the geometry of the specimens. It is investigated whether simulations for strains beyond the uniform strain yield realistic predictions. In the second application, deep drawing of cylindrical cups is simulated. The results are compared with experimentally obtained punch force–displacement curves and thickness distributions of different aluminum alloys (AA 5754-O and AA 6016, AA 6061 with tempering conditions T4 and T6). Finally, the material models are further verified by simulating the warm deep drawing of a square cup, as it prescribes more complex deformation paths than the cylindrical cup deep drawing. The chapter ends with conclusions.

4.1 Al–Mg (AA 5754-O) Alloy

The AA 5754-O alloy is generally classified as a non-heat treatable alloy. This reflects that no precipitation hardening takes place. In Al–Mg alloys, the work hardening effect is mainly due to the presence of solute atoms in solid solution. These solute atoms cause lattice distortions that impede dislocation motion, increasing the yield stress of the material. The experimental results used in this section are taken from the work of Van den Boogaard (2002).

4.1.1 Simulation of Uniaxial Tensile Tests

Numerical analyses of uniaxial tensile tests were performed to verify the implemented models and check the numerical behavior during necking. In addition to the thermo-mechanical nature, issues regarding stability are also addressed within the context of necking. Therefore, necking is a fairly demanding test problem for a numerical procedure.

The material parameters were derived from uniaxial tensile tests. Only measurements before reaching the maximum tensile force were used in the fitting process, because at higher strains the deformation becomes non-uniform. Therefore, it is to be expected that the experimental flow curves will be represented accurately by the simulation, up to the uniform strain. For tensile test experiments at elevated temperatures, local necking occurs

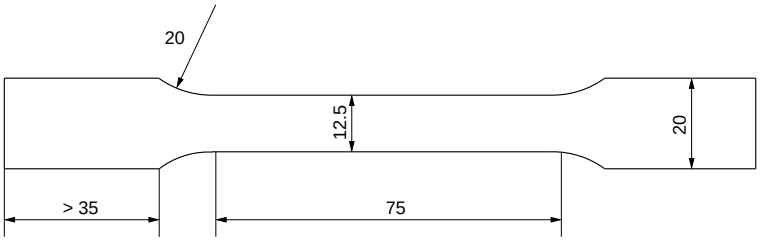

Figure 4.1: Geometry of the tensile test specimen (dimensions in mm).

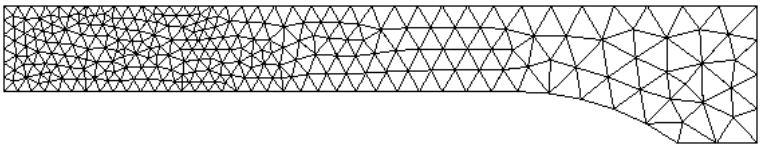

Figure 4.2: Finite element mesh of the tensile test specimen.

far beyond the uniform strain due to strain rate sensitivity. With the simulations it is investigated whether the FEM model can predict the necking strain at different temperatures and strain rates. The dimensions of the tensile test specimen are presented in Figure 4.1. The thickness of the specimen is 1.2 mm.

For the simulations, the Vegter yield function with the Nes and Bergström hardening models were used, fitted to the investigated AA 5754-O sheet. For efficiency, the experiments were simulated with only a quarter section of the specimen discretized by using membrane elements, see Figure 4.2. The typically inclined localization band cannot be modeled in this way, but experimentally this was only observed at room temperature. At elevated temperatures only symmetric failure modes were observed. The finite element models include the geometry of the specimen in the clamping area. This results in a slightly non-uniform strain distribution and strain localization occurs without including a numerical imperfection.

In Figure 4.3, experimental and numerical flow curves are presented for strain rates of $0.02\,\mathrm{s}^{-1}$ and $0.002\,\mathrm{s}^{-1}$ at different temperatures. At 100 °C the strain at localization is in agreement with the experiments. Up to 100 °C, the stress hardly depends on the strain rate at all and the specimen necks when the maximum engineering stress is reached. At higher temperatures, the deformation remains reasonably stable, even beyond the uniform strain. This is attributed to the stabilizing effect of strain rate sensitivity.

At 100 °C the predicted stress–strain curves and localization strain using the Bergström model is also in good agreement with the experiments. At low temperatures, the material behavior hardly depends on the strain rate and the specimen necks when the maximum stress is reached. At a strain rate of $0.02\,\mathrm{s}^{-1}$ and temperature of 175 °C, even though the calculated stress–strain curve follows the experimentally obtained curve well beyond the maximum stress, the numerical localization starts earlier than observed in the experiments.

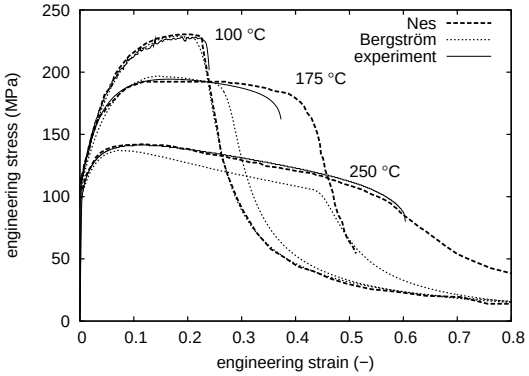

(a) $\dot{\varepsilon} = 0.02\,\mathrm{s}^{-1}$

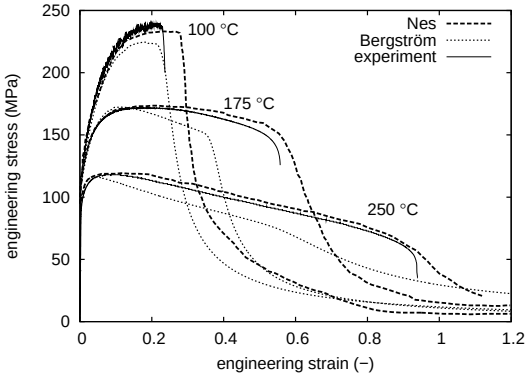

(b) $\dot{\varepsilon} = 0.002\,\mathrm{s}^{-1}$

Figure 4.3: Flow curves for tensile experiments and simulations.

At a temperature of 250 °C, the numerical curve already deviates before the maximum stress is reached. Again, final localization is numerically predicted before the experimental necking strain. Note, again, that for determination of the material parameters, only strains up to the maximum stress were used. At a strain rate of $0.002\,\mathrm{s}^{-1}$, the results are similar.

The calculated flow curves using the Nes hardening model follow the experimentally obtained curves well beyond the maximum stress for both strain rates, and the slope of the curves at higher temperatures also resembles the experimental curves quite well. At elevated temperatures, numerical localization starts only slightly later than observed in the experiments. Beyond the maximum stress, the predicted stress–strain behavior depends on the modeling of strain rate sensitivity. From the results, it can be clearly seen that the strain rate sensitivity is well described by the Nes model.

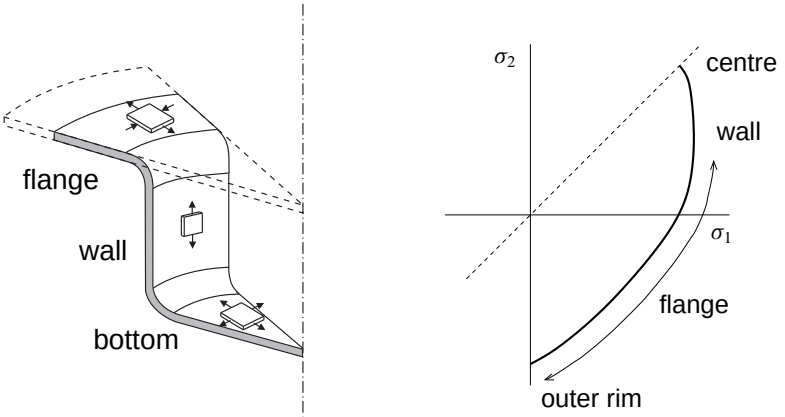

(a) Section with principal strains.

(b) Position on the yield locus.

Figure 4.4: Stress states in deep drawing of a cylindrical cup.

4.1.2 Cylindrical Cup Deep Drawing

Cylindrical cup drawing experiments were performed with a tool set of which the dimensions are given in Figure 2.6. During the deep drawing of cylindrical cups, the parts of the blank are subjected to different stress states under different deformation zones. Four deformation zones can be distinguished: the flange, the bending zone, the wall and the bottom of the cup as shown in Figure 4.4(a). The deformation in the flange is a result of tangential compressive stresses and radial tensile stresses, *i.e.* at the outer blank radius, the flange gets compressed in tangential direction causing the increase of thickness and hardening of the material. Towards die shoulder radius, this changes through pure shear and uniaxial tension in radial direction to plane strain deformation. The material must flow over the edge of the die shoulder and be subjected to bending combined with radial stretching. This can lead to a certain thinning of the sheet material in the bottom, particularly in the transition zone between the bottom and the sides of the cup. In the wall a plane strain situation exists, because the radius of the cylindrical part is constant. Because of symmetry the deformation in the bottom is mainly equi-biaxial, with only a deviation due to planar anisotropy. In Figure 4.4(b), the corresponding positions on the yield locus are denoted in the principal stress space.

All experiments were performed with blanks of 230 mm diameter that were taken from an aluminum (AA 5754-O) sheet of 1.2 mm thickness (Van den Boogaard, 2002). In the experiments, the effective punch stroke was 80 mm and the punch velocity 2 mm/s. The blank holder force was 25.5 kN, equivalent to an initial pressure of 1.0 MPa on the contact area. The die and the blank holder were given temperatures subsequently of 25 °C, 175 °C and 250 °C, while the punch was kept at 25 °C. The friction between tool and work-piece is one of the least known factors in the simulations. For the combination of materials and lubricant used, Van den Boogaard (2002) measured experimentally with a friction coefficient of 0.06 at room temperature. At temperatures above 150 °C, the friction coefficient varied

Table 4.1: Measured stress and strain ratios for the AA 5754-O sheet (Vegter yield locus data).

angle with RD	0°	45°	90°
$(\sigma_1/\sigma_1^{\mathrm{RD}})_{\mathrm{un}}$	1	1	1
f_{ps}	1.15	1.15	1.15
f_{sh}	0.605	0.605	0.605
f_{bi}	1.02		
R-value	0.85	0.67	0.70
$(\varepsilon_2/\varepsilon_1)_{\mathrm{bi}}$	1.17		

between 0.12 and 0.18 in different experiments. In the models, the value of the friction coefficient was 0.06 below 90 °C, 0.12 above 110 °C and linearly interpolated in between.

During deep drawing, the force–displacement curve of the punch was recorded. After the experiments, the cups were removed and the thickness distribution from the center to the outer diameter in the rolling direction was measured. The force–displacement curve and the thickness data will be used to validate the simulations.

The warm forming of aluminum sheet requires the solution of a thermo-mechanically coupled set of equations. The high conduction coefficient of aluminum and low sheet thickness make sure that the temperature is almost constant across the thickness. Thus, Kirchhoff triangular shell elements can be used with only one thermal d.o.f. per node. The gradient in the thickness direction need not be modeled. A heat transfer coefficient, $\alpha = 140\mathrm{W/m \cdot K}$ between tool and sheet is used. Due to the low punch velocity and the large heat capacity of the tools, the temperature of the tools is not much affected by the blank and the blank assumes the tool temperature where it is in contact. Therefore the results are not very sensitive to the value of α. The stiffness of the tools is much higher than that of the blank. It is therefore justified to model the tools as rigid contours with prescribed temperatures.

Orthotropic symmetry was assumed for the material model. A quarter of the blank was modeled and boundary conditions were applied on the displacement and rotation degrees of freedom to represent the symmetry. The blank is discretized using 998 discrete Kirchhoff triangular shell elements with a typical element edge size of 5 mm. Simulations are performed with the Vegter yield locus and the Nes or the Bergström hardening models at various temperatures. The model further contains 1996 contact elements, resulting in a total of 10812 degrees of freedom. The global convergence criterion was set to 0.5 % relative unbalance force. In the simulations punch displacement increments of 0.1 mm were used.

Influence of the Yield Locus

To investigate the influence of the yield locus on the analysis results, simulations were performed with the Vegter and the Barlat Yld2000 yield functions described in Chapter 3. The hardening effect was included in the analysis by using the Bergström hardening model with the material data of the investigated 5754-O alloy given in Table 3.2. The experimentally determined stress ratios were obtained by fitting the first 5 % strain of uniaxial, plane strain,

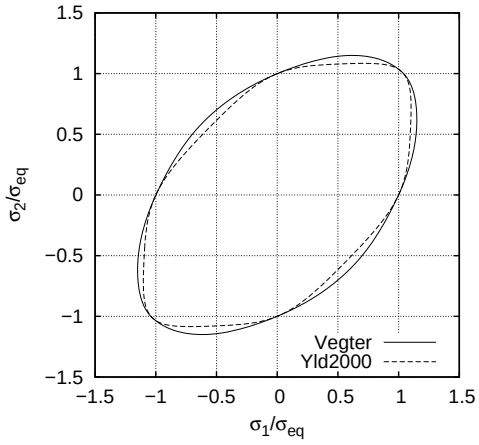

Figure 4.5: Yield locus shapes—Vegter and Yld2000.

simple shear and normal compression curves to each other. R vales and equi-biaxial strain ratios were measured directly on the specimens. The experimental values are presented in Table 4.1 and are directly used as input data for the Vegter yield function.

The eight input parameters of the Barlat Yld2000 function were obtained from the uniaxial stress ratios and R values in three directions $\sigma^{\mathrm{RD}}/\sigma^{\mathrm{RD}}$, $\sigma^{\mathrm{TD}}/\sigma^{\mathrm{RD}}$, $\sigma^{45}/\sigma^{\mathrm{RD}}$ and R_0, R_{90}, R_{45} and the equi-biaxial stress and strain ratio presented in Table 4.1. The calculation of the yield function coefficients from the test data is performed using a Newton–Raphson solver (Barlat *et al.*, 2003). The coefficients are given in Table 4.2.

In Figure 4.6, it can be seen that the punch force–displacement curve for the Yld2000 model is lower than for both the Vegter model and the experiments. This is attributed to the lower shear factor predicted by the Yld2000 model compared to the Vegter model, that is purely based on experimentally obtained values as shown in Figure 4.5. The material deformation takes place mainly in the flange area, and in this area shear deformation dominates. Hence a lower shear factor results in a lower punch force. At larger drawing depths (above 70 mm), *i.e.* at the outer radius, the stress state reaches to uniaxial compression, which is equal for both yield functions gives almost equal punch forces.

In Figure 4.7, the influence of yield locus on the wall thickness prediction is presented. On the abscissa, the arc length is given from the center of the cup to the outer radius in

Table 4.2: Barlat Yld2000 anisotropy coefficients for the AA 5754-O sheet.

α_1	1.0036	α_2	0.94864	α_3	0.95264
α_4	1.0083	α_5	0.99186	α_6	0.92749
α_7	0.96348	α_8	1.0779		

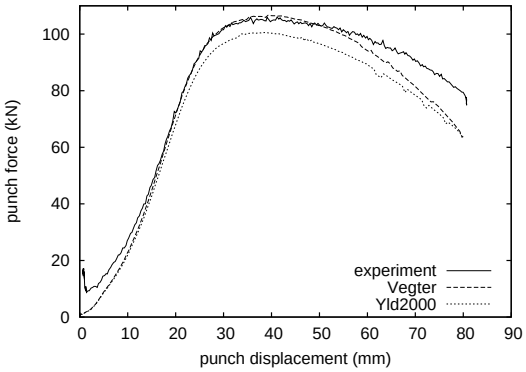

Figure 4.6: Punch force–displacement diagrams—Influence of yield locus.

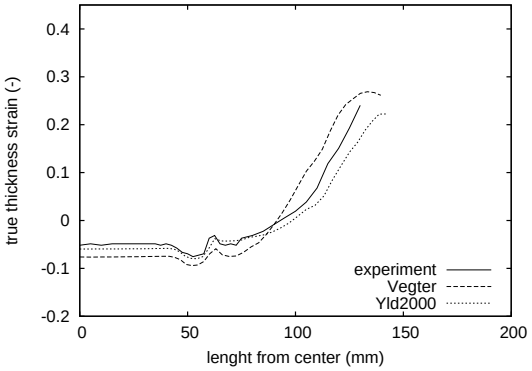

Figure 4.7: Thickness distributions—Influence of yield locus.

the rolling direction and on the ordinate true thickness strain is given. Both the simulations using the Vegter model and Yld2000 predict too much thinning at the bottom of the cup. However, thinning is more severe with the Vegter yield locus. This is attributed to the higher punch force applied at the base of the cup, which is transmitted through the wall to the flange and is due to the higher shear factor of the Vegter yield function.

Influence of the Hardening Model

To investigate the influence of the hardening model, simulations were performed at various temperatures using the Bergström and the Nes hardening models described in Chapter 3. The Bergström and the Nes models input data of the investigated 5754-O alloy are given in Table 3.2 and Table 3.3 respectively. In the simulations, anisotropy of the sheet was described using the Vegter yield function and the input data was given in Table 4.1. In

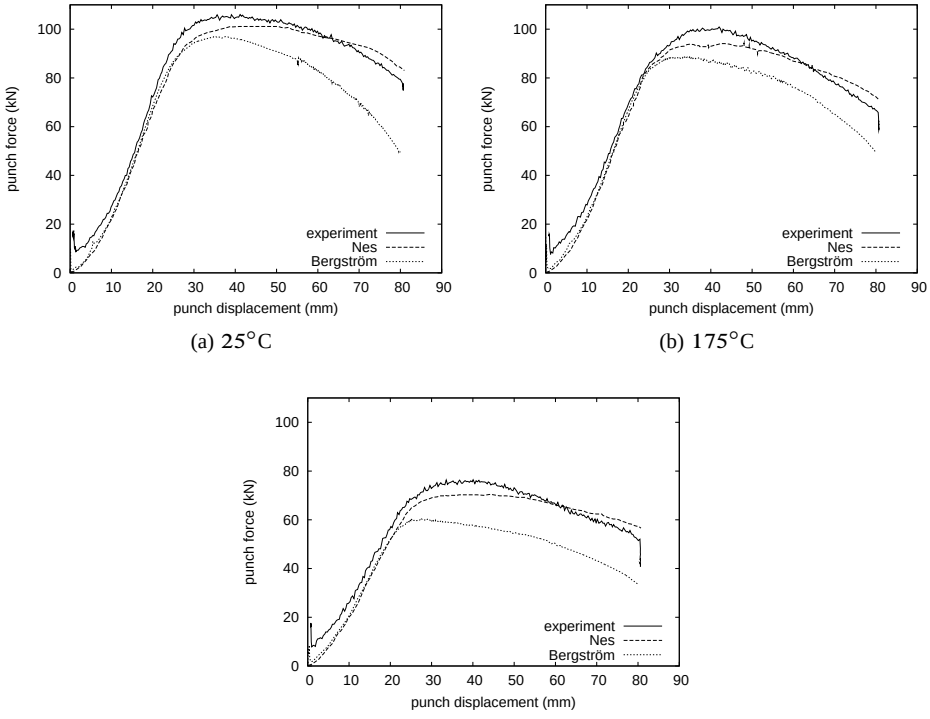

(a) 25°C

(b) 175°C

(c) 250°C

Figure 4.8: Punch force–displacement curves for AA 5754-O.

Figure 4.8 and Figure 4.9, the force–displacement diagrams of the punch and the thickness distributions of the cup at 80 mm punch displacement/drawing depth are plotted for the experiments and the simulations with the Bergström and Nes models, respectively.

Comparing the different punch force–displacement curves, it can be seen that both numerical models underestimate the maximum punch force. The underestimation is more severe with the Bergström model than with the Nes model. At larger drawing depths (above 55 mm), the punch force is slightly overestimated with the Nes model due to high strain rate sensitivity effects. But with the Bergström model, the punch force is significantly underestimated at higher drawing depths as shown in Figure 4.8.

Nevertheless, both numerical models predicted the trends with changing temperature very well. The relatively small difference in punch force between 25 °C and 175 °C is due to the increasing friction coefficient around 100 °C, that counteracts the effect of the decreasing flow stress.

The influence of the temperature on the thickness after 80 mm punch stroke is most pronounced in the bottom of the cup. In the simulations, the thickness reduction in the bottom of the cup is too high with both hardening models. In the die radius area, the Nes model performs slightly better than the Bergström model as shown in Figure 4.9.

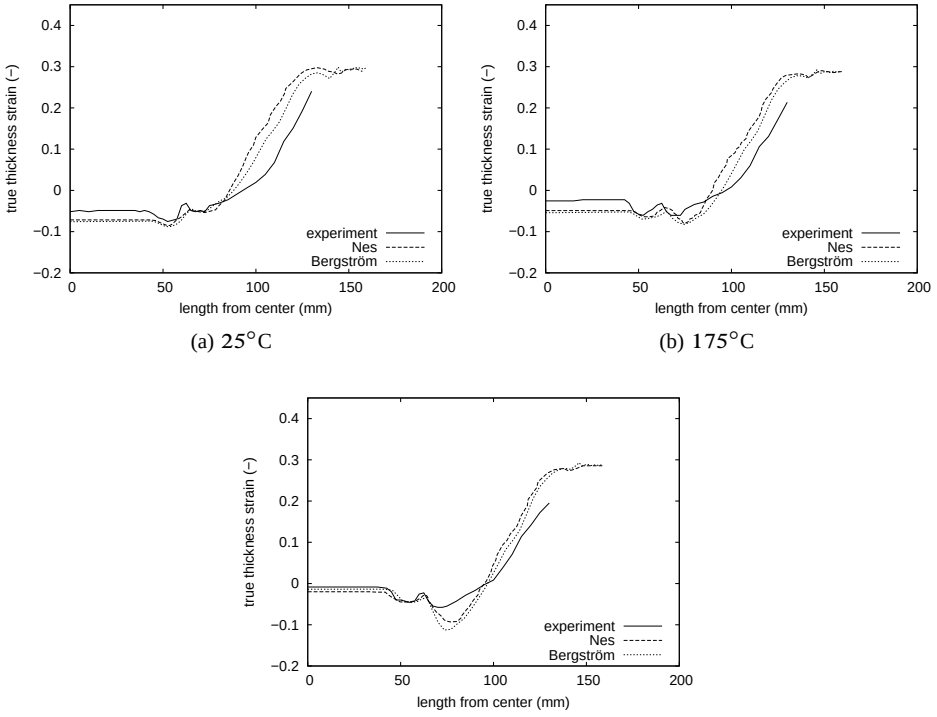

(a) 25°C

(b) 175°C

(c) 250°C

Figure 4.9: Thickness distributions for AA 5754-O.

Although the material behavior is modeled very well with advanced yield functions and microstructure based hardening models, numerically predicted wall thicknesses are not satisfactory. One of the suspected reasons is the temperature independent yield locus. In the simulations, the yield surface was assumed to remain constant with respect to changing temperatures. The used anisotropic yield locus input parameters were identified from the room temperature experiments and could not be performed at elevated temperatures. Alternatively, crystal plasticity based models can be used to identify the yield locus input parameters at elevated temperature, but different slip systems must be assumed. This solution approach will be addressed in Section 4.3.

Another expected reason for the deviation is the modeling of friction. The punch force prediction can easily be improved by increasing the friction. However, the increased friction coefficient leads to an even thinner predicted bottom area (Van den Boogaard and Huétink, 2006). In order to get the full benefit from the improved material models in warm forming simulations, a comprehensive study of friction behavior at elevated temperatures is required.

4.2 Al–Mg–Si Alloys

Most of the investigations existing in the literature were performed with 5xxx series alloys only. Recently, researchers are inclined to 6xxx series alloys, since the Al–Mg–Si alloys have good corrosion resistance and obtain high strength controlled by the precipitates formed during the ageing treatment. The age hardening response of these alloys is very significant and hence control of precipitation during thermo-mechanical treatment is critical for attaining optimal alloy performance. Also this process is industrially more challenging and more complex in terms of microstructure-mechanical behavior relationship.

Bolt *et al.* (2001) conducted warm drawing tests on AA 5754 and AA 6016 in order to compare the performance of these two alloys. They found that the minimum die temperature required for a significant deeper product is lower for the AA 6016-T4 compared to AA 5754-O alloy. At a temperature of 175 °C the increase in maximum height for AA 6016-T4 is 30 % while it is only 11 % for AA 5754-O. These early trials act as an important database for further exploration of warm forming potential of existing and new aluminum alloys. Although 5xxx alloys have been proved to be sensitive to warm forming, recent experiments with 6xxx alloys also show promising results in terms of enhanced ductility at warm temperatures with the added advantage of precipitation hardening. An effort has been made in the present investigation to study the effect of various parameters on warm forming of 6xxx alloys. The effect of punch velocity, drawing ratio, temper and temperature on force–displacement curves and thickness distribution are investigated.

4.2.1 Model Predictions and Discussions

In this section, the validity of the work hardening models presented in Chapter 3 is verified for the investigated Al–Mg–Si alloys. The Nes model involves a larger number of parameters than the Bergström model, some of the parameters of both models are selected beforehand, such as the magnitude of the Burgers vector b, Debye frequency ν_d and the shear modulus G and activation energies are taken from the literature. The Nes model directly takes into account the chemical composition of the investigated alloys AA 6016 and AA 6061 were given in Table 2.1. The atomic fraction of Mg solute concentration (c) and the total atomic fraction of Si and Cu in solid solution (c_0) are calculated from mass balance given in Table 4.3.

For T4 condition, precipitates are considered as GP zones or naturally aged clusters with an average size of < 1nm and are shearable. If the particles are larger than the critical size (approximately 5 –5 nm, the precipitates become incoherent and dislocations are no longer able to cut through them. They must bypass the non-shearable particles by bowing round the particles and this is generally described using the Orowan mechanism given in Equation (3.32). In order to take into account the stress contribution due to both shearable and non-shearable particles, a relation proposed by Myhr *et al.* (2001) is used. The particles with a mean radius r and volume fraction f_r are given as follows:

$$\tau_p = 2AG\frac{b}{r}\left(\frac{3f_r}{2\pi}\right)^{1/2} \min\left[\left(\frac{r}{r_c}\right)^{3/2}, 1\right] \tag{4.1}$$

r_c is the critical radius deciding between shearable and non-shearable mechanisms. In the

Table 4.3: Atomic fractions of Mg (c) and Si & Cu (c_0), grain size of investigated Al–Mg–Si alloys.

Alloy	Mg (at. fraction)	Si and Cu (at. fraction)	grain size (m)	vol. fraction	particle size (m)
6016-T4	0.0038	0.0080	$19 \cdot 10^{-6}$	0.0049	$0.8 \cdot 10^{-9}$
6016-T6	0.0001	0.0034	$20 \cdot 10^{-6}$	0.0098	$4.5 \cdot 10^{-9}$
6061-T4	0.0089	0.0046	$16 \cdot 10^{-6}$	0.0094	$0.8 \cdot 10^{-9}$
6061-T6	0.0068	0.0009	$15 \cdot 10^{-6}$	0.0081	$4.8 \cdot 10^{-9}$

above equation, G is the shear modulus of the aluminum matrix, b is the length of the Burgers vector and A is a constant close to 0.5. The precipitate size and volume fractions (input parameters) are determined by fitting the average yield strength of experimental measurements for both alloys with Equation (4.1) and are given in Table 4.3.

It is observed that the difference in chemical composition between AA 6016 and AA 6061 in T4 condition has negligible effect on work hardening, and therefore, the dependence with the alloy is neglected. Hence the fitting parameters, C, q_c and e_t are determined by a least square approximation of uniaxial tensile tests performed on 6016-T4 and 6061-T4 alloys at temperatures 25 °C, 150 °C and 250 °C at strain rates of 0.01 s^{-1} and 0.1 s^{-1} using a Matlab parameter optimization program. All other parameters are taken from the literature. The selected and fitted parameters for the Nes model for both AA 6061 and AA 6016 in T4 condition are given in Table 4.4.

For comparison, the Bergström model is used and the eight fit parameters are determined by a least squares approximation of uniaxial tensile tests performed on 6016-T4 and 6061-T4 alloys. The parameters are determined *separately* on each alloy at temperatures 25 °C, 150 °C and 250 °C at strain rates of 0.01 s^{-1} and 0.1 s^{-1}. The resulting parameters for AA 6016 and AA 6061 for T4 condition are given in Table 4.5 and Table 4.6 respectively.

The simulated stress–strain curves are plotted for AA 6061-T4 alloy in Figure 4.10 using the Nes and the Bergström models, together with the experimental data. The stress–strain curves for temperatures of 25 °C, 150 °C and 250 °C are plotted in Figure 4.10(a) for a

Table 4.4: Parameters for the Nes model (AA 6061 & AA 6016 alloy in T4 condition).

ν_D	$1.0 \cdot 10^{13} s^{-1}$	b	$2.86 \cdot 10^{-10}$ m	κ	$1.3 \cdot 10^{-23}$ J/K
q_c	9.2	C	31.47	f	0.1
α_1	0.3	α_2	3.0	κ_0	$3.5\,m^{-1}$
U_s	150000 J/mol	U_{sd}	160000 J/mol	ΔU_s	0.0 J/mol
κ_2	2.0	κ_3	0.001	φ_c	0.3489
B_t	57.0	ω_ρ	25.0	ω_t	20.0
e_t	0.581	B_ρ	0.23	ξ_ρ	80.2
ω_s	1.0	e_ρ	0.67	B_δ	100.0
ξ_δ	40.0	e_δ	0.65	ρ_0	$1.0 \cdot 10^{11} m^{-1}$
S_{IV}	0.15	q_{IV}	2.0	φ_{IV}	0.052 rad

Table 4.5: Parameters for the Bergström model (AA 6016-T4 alloy).

σ_0	146.13 MPa	m	0.5	ρ_0	$10^{11}\,\mathrm{m}^{-1}$
α	1.0	U_0	$6.663 \cdot 10^{8}\,\mathrm{m}^{-1}$	G_{ref}	26354 MPa
b	$2.857 \cdot 10^{-10}\,\mathrm{m}$	Ω_0	31.41	C_{T}	134.41
C	$1.89 \cdot 10^{4}$	Q_{v}	$6.82 \cdot 10^{4}\,\mathrm{J/mol}$	T_1	3132 K

Table 4.6: Parameters for the Bergström model (AA 6061-T4 alloy).

σ_0	176.22 MPa	m	1.18	ρ_0	$10^{11}\,\mathrm{m}^{-1}$
α	1.0	U_0	$7.16 \cdot 10^{8}\,\mathrm{m}^{-1}$	G_{ref}	26354 MPa
b	$2.857 \cdot 10^{-10}\,\mathrm{m}$	Ω_0	39.5	C_{T}	124.28
C	$6.765 \cdot 10^{4}$	Q_{v}	$1.0298 \cdot 10^{5}\,\mathrm{J/mol}$	T_1	3132 K

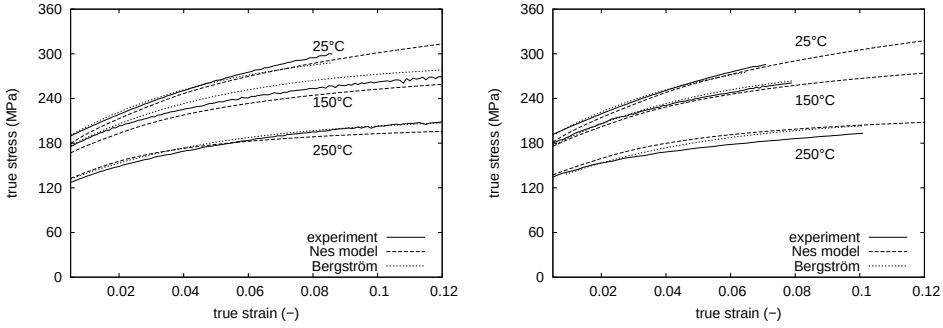

(a) $\dot{\varepsilon} = \mathbf{0.01}\,\mathrm{s}^{-1}$ (b) $\dot{\varepsilon} = \mathbf{0.1}\,\mathrm{s}^{-1}$

Figure 4.10: True stress–strain curves—experiments and different models (AA 6061-T4 alloy).

strain rate of $\dot{\varepsilon} = 0.01\,\mathrm{s}^{-1}$ and in Figure 4.10(b) for a strain rate of $\dot{\varepsilon} = 0.1\,\mathrm{s}^{-1}$. At higher strain rate and the temperatures below 150 °C both models perform quite well. For higher temperatures, *i.e.* at 250 °C the differences are slightly larger. It can also be observed that at low strain rate and temperatures below 150 °C the initial yield stress is underestimated with the Nes model.

The stress–strain curves at several temperatures with the strain rates of $0.01\,\mathrm{s}^{-1}$ and $0.1\,\mathrm{s}^{-1}$ are plotted in Figure 4.11(a) for experiments and in Figure 4.11(b) for the Nes model. From the experimental stress-strain curves, we can observe that at temperatures 25 °C and 150 °C, the lowest strain rate yields lowest hardening rate, which is usual. Even though the difference is small, at 250 °C the lowest strain rate yields the highest hardening rate, which looks unusual. The possible explanation is the higher dynamic precipitation at the lowest strain rate. However, as can be seen in Figure 4.11(b) the Nes model cannot

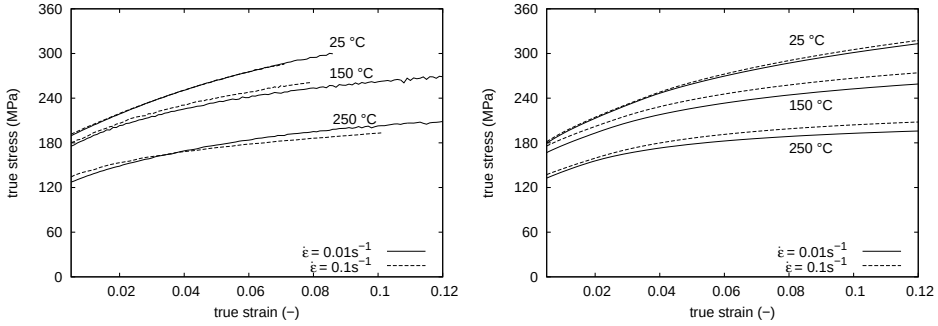

(a) Experiments (b) Nes model

Figure 4.11: Strain rate influence on stress-strain curves—experiments and model (AA 6061-T4 alloy).

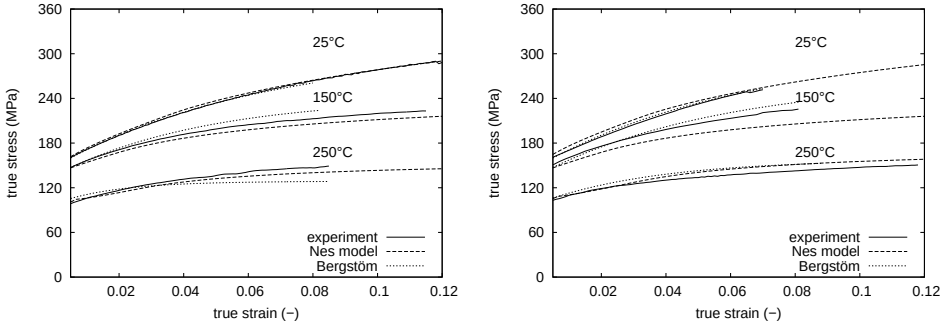

(a) $\dot{\varepsilon} = 0.01\,\mathrm{s}^{-1}$ (b) $\dot{\varepsilon} = 0.1\,\mathrm{s}^{-1}$

Figure 4.12: True stress–strain curves—experiments and different models (AA 6016-T4 alloy).

describe the effect of dynamic precipitation.

Figure 4.12 shows the simulated true stress–strain curves plotted for the Bergström and the Nes models, together with experimental data of 6016-T4 condition for various temperatures and strain rates. It can be seen that the models are more or less qualitatively describing the experiments. For the higher temperatures, the differences are slightly larger. It can also be observed that at higher strain rate and temperature of 150 °C the deviation is more severe with the Nes model.

Work Hardening in Artificially Aged Condition (T6)

The work hardening of heat treatable materials like Al–Mg–Si alloys comes mostly from the nanometer sized particles which are precipitated on certain crystallographic planes. These particles then interfere with the dislocation motion which increases the resistance to

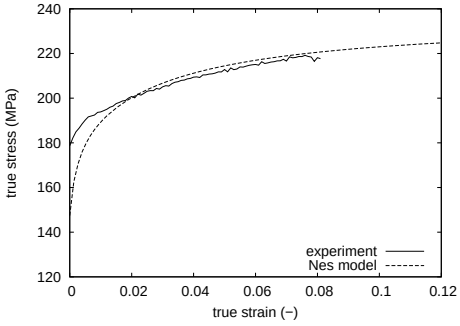

Figure 4.13: Simulated stress–strain curve with the Nes model (with out adaptation).

deformation and raises the strength of the alloys. Also solute atoms left in the metal matrix contribute to the hardening. The main reason for the difference in strength between tempers is due to the different sizes and density of the particles and the mechanism in which the dislocations are impeded by the particles. For the naturally aged temper condition (T4), the particles are precipitated into clusters known as GP zones, which are coherent with the metal matrix. GP zones offers coherency strain fields, which impede the motion of dislocations. For the artificially aged condition (T6), the particles should ideally have the optimum contribution of size and density to give the maximum initial yield strength with reduced work hardening rate. However, the maximum initial strength contribution due to these optimal size and density of the particles is not properly described by Equation (4.1) as shown in Figure 4.13.

In this work, the effect of maximum initial yield strength due to shearing of particles is included by a simple phenomenological relation in terms of temperature

$$\sigma_{\mathrm{p}}^{\mathrm{adapt}} = 96.5023 + 0.2138T - 1.1224 \cdot 10^{-04} T^2 \tag{4.2}$$

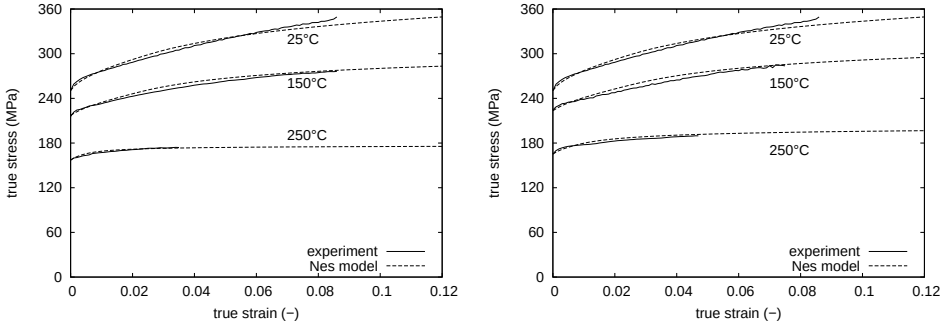

(a) $\dot{\varepsilon} = 0.01\,\mathrm{s}^{-1}$ (b) $\dot{\varepsilon} = 0.1\,\mathrm{s}^{-1}$

Figure 4.14: True stress–strain curves—experiments and the Nes model (AA 6016-T6 alloy).

as obtained by fitting of tensile tests at different temperatures and strain rates. The simulated stress–strain curves with the adapted Nes model together with experimental data for various temperatures and strain rates are presented in Figure 4.14. It can be seen that the adapted Nes model is capable of describing the experimental curves.

4.2.2 Cylindrical Cup Deep Drawing

In this section, the implemented material models are evaluated in terms of a case study concerned with warm deep drawing of cylindrical cups made up of 1.01 mm thick AA 6016 sheet and 1.2 mm thick AA 6061 sheet for different tempering conditions at various punch velocities and temperatures. Orthotropic symmetry was assumed for the material model. A quarter of the blank was modeled and boundary conditions were applied on the displacement degrees of freedom to represent the symmetry. The sheets were modeled with discrete Kirchhoff triangular shell elements with 3 translational, 3 rotational and 1 temperature degree of freedom per node. The tools were modeled as rigid contours with a prescribed temperature. In the presented simulations the die and the blank holder were given a temperature of 25 °C, 180 °C and 250 °C, while the punch was kept at 25 °C. Simulations are performed with the Vegter yield locus and the Nes and the Bergström hardening models implemented in the in-house implicit code DiekA. The Vegter yield locus data for AA 6016-T4 and AA 6061-T4 are presented in Tables 4.7 and 4.8. In the simulations a temperature dependent friction coefficient is used, with a linear relation from 0.06 to 0.12 for temperatures from 90 °C to

Table 4.7: Measured stress and strain ratios for the AA 6016-T4 sheet (Vegter yield locus data).

angle with RD	0°	45°	90°
$(\sigma_1/\sigma_1^{\mathrm{RD}})_{\mathrm{un}}$	1	1	1
f_{ps}	1.095	1.082	1.089
f_{sh}	0.574	0.608	0.58
f_{bi}	0.91		
R-value	0.54	0.47	0.87
$(\varepsilon_2/\varepsilon_1)_{\mathrm{bi}}$	0.7053		

Table 4.8: Measured stress and strain ratios for the AA 6061-T4 sheet (Vegter yield locus data).

angle with RD	0°	45°	90°
$(\sigma_1/\sigma_1^{\mathrm{RD}})_{\mathrm{un}}$	1	1	1
f_{ps}	1.095	1.079	1.09
f_{sh}	0.568	0.601	0.565
f_{bi}	0.95		
R-value	0.84	0.59	1.04
$(\varepsilon_2/\varepsilon_1)_{\mathrm{bi}}$	1.12		

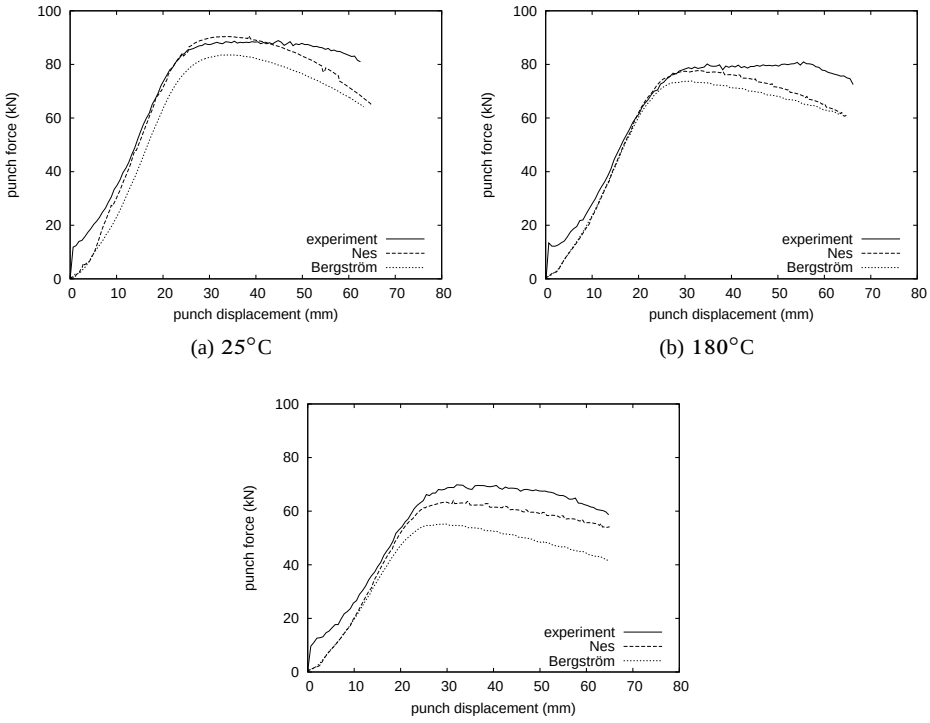

(a) 25°C (b) 180°C

(c) 250°C

Figure 4.15: Punch force–displacement curves for AA 6016-T4 alloy at different temperatures.

110 °C and constant before and after this range.

In Figures 4.15 and 4.16, the force–displacement diagrams of the punch and the thickness distribution of the cup are plotted for the simulations with the Nes and Bergström models together with the experiments performed at several temperatures for the material AA 6016-T4.

Comparing the different punch force–displacement curves, it can be seen that the Nes model performs very well at all the temperatures. At 25 °C, the Nes model slightly overestimated the maximum punch force and underestimated the punch force at larger drawing depths. The Bergström model shows a more severe underestimation of the punch force than the Nes model. At 250 °C, the Bergström model is even less accurate than at room temperature. However, the trends with changing temperature are predicted well with both numerical models.

At room temperature, both hardening models predict the same thickness reduction at the bottom as observed in the experiments. At elevated temperature, it can also be observed that the predicted thickness reduction in the bottom of the cup is too high using the Bergström model than the prediction of the Nes model.

Similarly for the material AA 6061-T4, the simulated force–displacement diagrams of

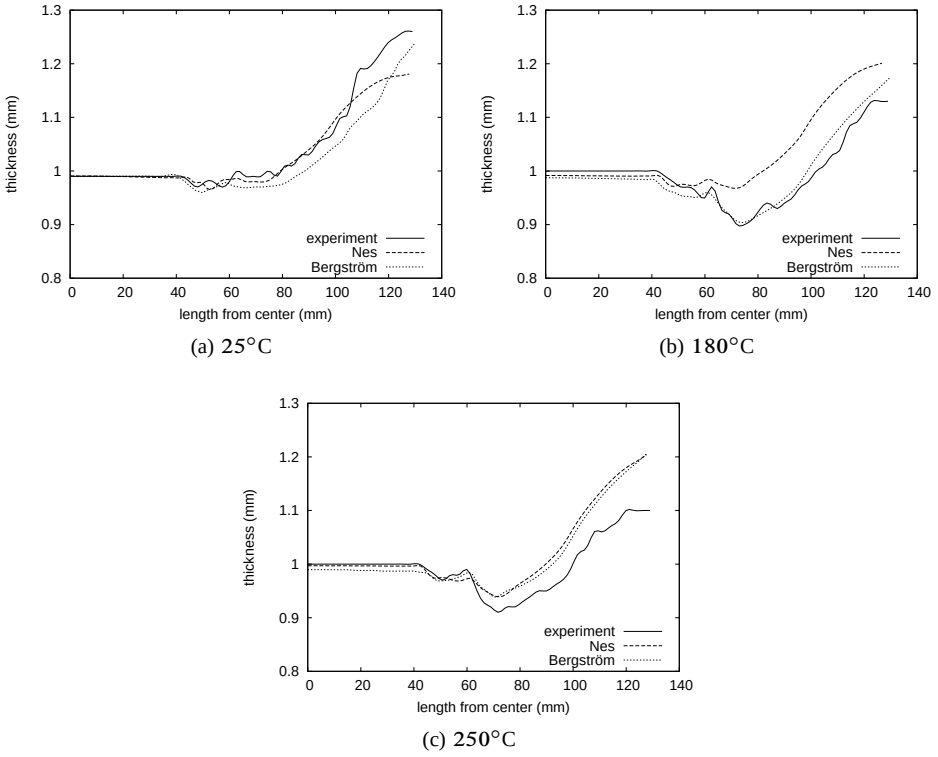

(a) 25°C (b) 180°C

(c) 250°C

Figure 4.16: Thickness distributions curves for AA 6016-T4 alloy at different temperatures.

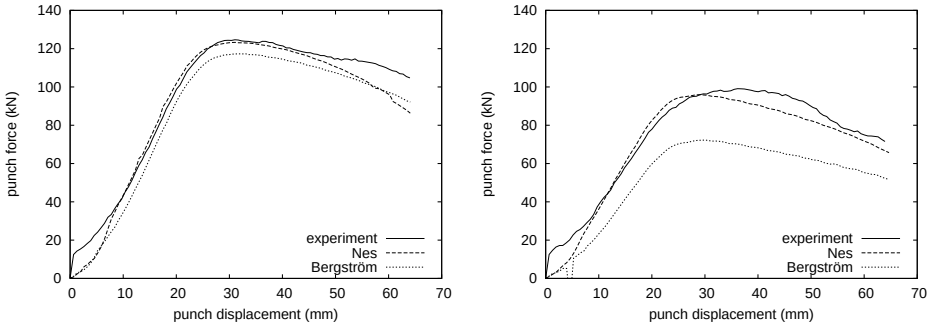

(a) 25°C (b) 250°C

Figure 4.17: Punch force–displacement curves for AA 6061-T4 alloy at different temperatures.

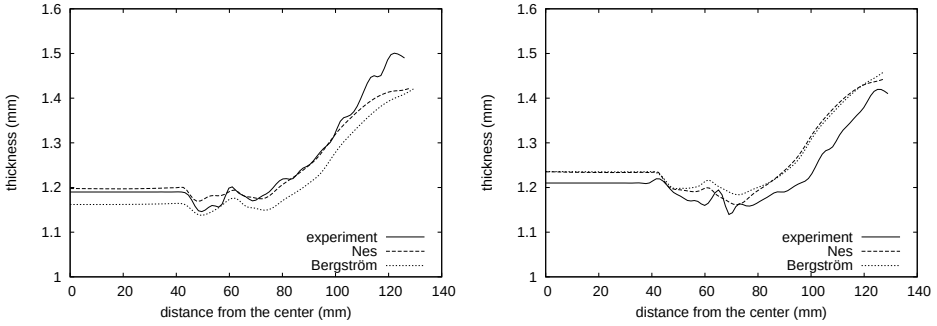

(a) 25°C (b) 250°C

Figure 4.18: Thickness distribution curves for AA 6061-T4 alloy at different temperatures.

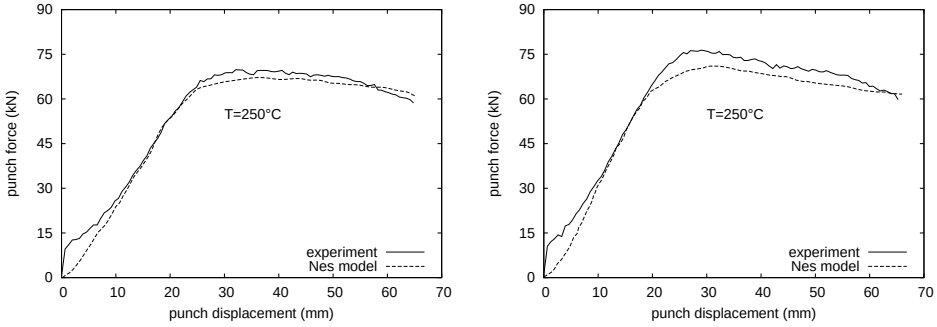

(a) AA 6016-T4 alloy (b) AA 6016-T6 alloy

Figure 4.19: Deep drawing of cylindrical cup—effect of tempering.

the punch and the thickness distribution of the cup at a depth of 64 mm are compared with the experiments performed at 25 °C and 250 °C are presented in Figures 4.17 and 4.18.

Comparing the different punch force–displacement curves, it can be seen that the general trends with changing temperature are predicted well. However, the Nes model is slightly overestimating the punch force after the highest point of the experimental curve at 25 °C. The Bergström model underestimates the punch force at both temperatures. At 250 °C, this underestimation is more severe with the Bergström model.

At room temperature, both hardening models predict more thinning at the bottom than observed in the experiments. At elevated temperature, it can be observed that the predicted thickness reduction in the bottom of the cup is much too high using the Bergström model and only slightly too high with the Nes model.

In Figure 4.19, the force–displacement diagrams of the punch are plotted for the simulations and the experiments performed on AA 6016 alloy at different tempering conditions. From the punch force–displacement curves, it can be seen that the numerical model un-

derestimates the maximum punch force for T6 tempering condition more than predicted in T4 condition. It is noted that the higher initial strength in peak aged (T6) condition caused by the precipitates sheared with the moving dislocations is included in the model by a phenomenological fit function given in Equation (4.2).

4.3 Effect of Temperature on Anisotropy

For the accurate numerical simulation of sheet metal forming, the use of an appropriate material model is of vital importance. Particularly for warm forming simulation, an accurate coupled thermo-mechanical material model for the anisotropic yield function with temperature and rate dependent hardening is required. Use of anisotropic material models in numerical analysis requires thorough material characterization under multiple loading conditions. Since the material anisotropy and hardening behavior change with higher temperatures, the anisotropy coefficients and the hardening behavior must be determined as a function of temperature to perform accurate thermo-mechanical finite element analysis for these materials.

Prior research available for simulation of warm forming processes focused only on the effect of elevated temperature on the evolution of the flow stress. Van den Boogaard and Huétink (2006) characterized the behavior of AA 5754-O for which two types of flow laws were used: the modified power law and the physically based Bergström model. The Vegter yield surface (Vegter and van den Boogaard, 2006) used in this case was assumed to remain constant with respect to changing temperatures. Only the coefficients of the hardening laws were fitted as function of temperature and strain rate. The predictions of the material model, however, underestimated the values of the punch load in both models. Recently, Kurukuri *et al.* (2009) presented warm deep drawing simulations using the more advanced physically based Nes hardening model for 5754-O alloy and still it underestimates the punch force, even though it performs better than the Bergström model. In all the above works, the effect of temperature on the yield locus shape and anisotropy coefficients were not explored.

In the last decade, very accurate anisotropic yield functions were proposed for sheet metal forming simulations at room temperature, such as the planar anisotropic Vegter yield locus (Vegter and van den Boogaard, 2006) based on experimental measurements and Barlat yield functions (Barlat *et al.*, 2003) for aluminum alloys. However, very limited experimental data of yield loci at elevated temperatures has been reported. This is because the determination of yield loci at elevated temperatures is not an easy task. Recently, Merklein *et al.* (2008) designed an experimental setup for the biaxial tensile testing of sheet metal at elevated temperatures. Naka *et al.* (2003) investigated the effects of temperature on yield locus for 5083 aluminum alloy sheet. They obtained the yield locus for a fine grain Al–Mg alloy (5083-O) sheet by performing biaxial tensile tests, using cruciform specimens, at temperatures of 30 °C, 100 °C, 170 °C, 250 °C, and 300 °C at $1s^{-1}$ strain rate. In the present work, an effort is being made to use the combination of experimental measurements and a crystal plasticity model to identify the yield locus parameters at elevated temperature by activating more slip systems.

For the material model to account for changes in temperature, the anisotropy coefficients which describe the state of anisotropy must be represented as a function of temperature. At room temperature, the Vegter yield surface parameters were identified from the mechanical

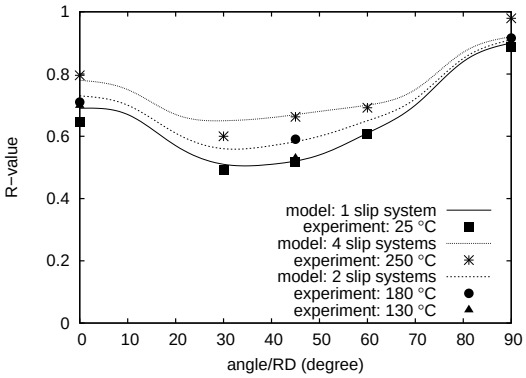

Figure 4.20: Lankford R value measured (symbols) and calculated (lines) at different temperatures for AA 6016-T4 alloy.

tests proposed in Vegter and van den Boogaard (2006). The evolution of yield surface due to temperature is included by identifying the anisotropy coefficients at several temperatures from the Visco Plastic Self Consistent (VPSC) crystal plasticity model (Lebensohn and Tomé, 1993). Experimental observations have shown that in addition to the octahedral slip systems other slip system families can be activated when the temperature is increased (Bacroix and Jonas, 1988). EBSD maps measured from the deep drawn cylindrical cups at several temperatures also revealed that at room temperature the bands are parallel to the $\{111\}\langle 110\rangle$ plane while at 250 °C, these bands are also parallel to the $\{112\}$ and sometimes $\{110\}$, $\{100\}$ planes when EBSD maps are plotted in band contrast mode.

The activated slip system families and their Critical Resolved Shear Stresses (CRSS) were obtained at specific temperatures by fitting the R values calculated with the VPSC model to the R values measured at these temperatures and for several tensile directions as shown in Figure 4.20. Measured R values at 130 °C are equal to the values at room temperature meaning that only the $\{111\}\langle 110\rangle$ slip systems are activated in this temperature range. A good fit was obtained at 180 °C by using the $\{111\}\langle 110\rangle$ and $\{112\}\langle 110\rangle$ families with CRSS ratio 1:1.2 while at 250 °C four families of slip systems $\{111\}$,$\{110\}$,$\{100\}$ and $\{112\}\langle 110\rangle$ are required with the CRSS ratios $0.9 : 1 : 1.1 : 1$. For all the calculations with the VPSC model the initial experimentally measured texture was described by 2000 orientations. Figure 4.21 shows the change in the shape (stress values are normalized with respect to equivalent (uniaxial) stress, σ_{eq}). It is evident from Figure 4.21 that temperature has a distinct effect on the yield surface's shape, which must be accounted for during warm forming simulations.

In the simulations the die and the blank holder were given a temperature of 250 °C, while the punch was kept at 25 °C. During deep drawing operation the area under the punch was at 25 °C and the temperature has gradually increased from 25 °C to 250 °C in the wall to flange of the cup. From the VPSC calculations, the Vegter yield locus parameters were calculated only at specific temperatures, *i.e.* at 25 °C, 130 °C, 180 °C and 250 °C. Quadratic interpolating functions were used to define the yield locus parameters as a continuous

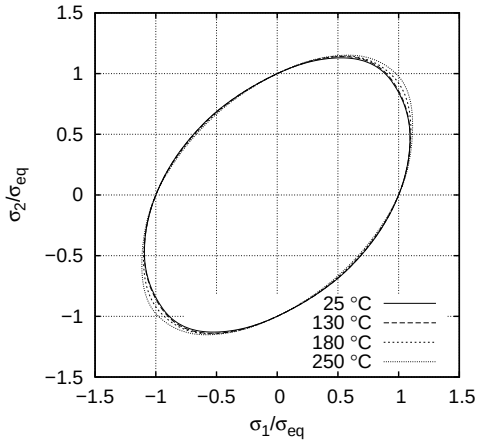

Figure 4.21: The Vegter yield function for AA 6016-T4 at several temperatures (stresses normalized to show the change in the yield surface shape).

function of temperature.

Simulations with the temperature dependent Vegter yield locus and the Nes hardening model are performed. In the simulations a temperature dependent friction coefficient is used, with a linear relation from 0.06 to 0.12 for temperatures from 90 °C to 110 °C and constant before and after this range.

To investigate the influence of yield locus shape change due to temperature, warm deep drawing simulations of cylindrical cups are performed with and without considering the effect of temperature in the simulations. In Figure 4.22, the force–displacement diagrams of the punch, the thickness distributions of the cup at a depth of 64 mm and the earing profiles are plotted for the experiments and the simulations.

Comparing the simulated punch force–displacement curves with and without temperature effects together with the experiments, it can be seen that the numerical model underestimates the experimental curve in both simulations at 250 °C. This underestimation is slightly higher with the effect of temperature on the yield locus. From the thickness distribution vs. distance from the center of the cup curve as shown in Figure 2.12, it can be observed that a better agreement for the wall thickness is predicted when the effect of temperature on the yield locus is included.

Figure 4.22(c) shows that the deformation temperature strongly influences the anisotropy and earing profile. From the room temperature experiment, the earing profile exhibits four ears. When the deformation temperature is increased to 250 °C, experimental earing profile nearly exhibits two ears in the first series of experiments presented in Chapter 2. The model cannot show the change from four to two earing profiles in both situations. However, the model does show different earing profiles when the effect of temperature on yield locus is included, *i.e.* the model including the temperature effects leads to an earing profile that is exactly opposite to the one obtained without temperature effects.

From these warm forming simulations of the cylindrical cup deep drawing, it can be

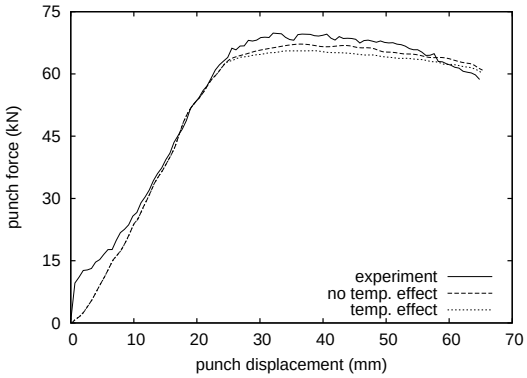

(a) Punch force–displacement curves.

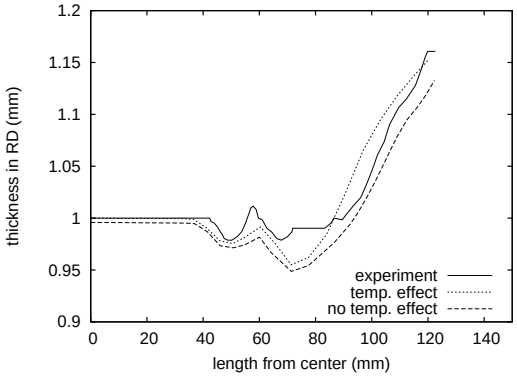

(b) Thickness distribution in RD.

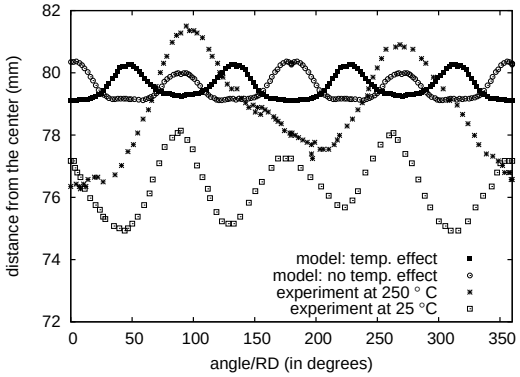

(c) Earing profiles.

Figure 4.22: Deep drawing of cylindrical cup—experiments and simulations with and without temperature effects on yield locus (AA 6016-T4 alloy) at 250 °C.

Figure 4.23: Warm deep drawn square cup (courtesy Corus RD & T).

concluded that the effect of temperature on shape change of yield locus has an effect notably on the predicted thickness distribution, indeed the predicted thickness with the model including temperature effects coincides the experimentally measured thickness at the bottom. In the die radius area also, the model with temperature effects performs slightly better than the one obtained without temperature effects.

4.4 Warm Deep Drawing of a Square Cup

To assess the implemented material models (Nes and Bergström hardening models) further warm forming of a *square cup* made of Al–Mg sheet (AA 5754-O alloy) with an initial thickness of 1.2 mm is simulated. The square cup is fabricated by Corus in collaboration with Inalfa at Inalfa Metal Products BV., Belgium and is presented in Figure 4.23.

Simulations were carried out using the Nes and the Bergström hardening models. Orthotropic symmetry was assumed for the material model. A quarter of the blank was modeled and boundary conditions were applied on the displacement degrees of freedom to represent the symmetry. The sheets were modeled with 5300 discrete Kirchhoff triangular shell elements with 3 translational, 3 rotational and 1 temperature degree of freedom per node. The tools were modeled as rigid contours with a prescribed temperature. In the presented simulations the die and the blank holder were given a temperature of 300 °C, while the punch was kept at 25 °C. Anisotropy of the sheet was described by using the Vegter yield surface parameters as given in Table 4.1.

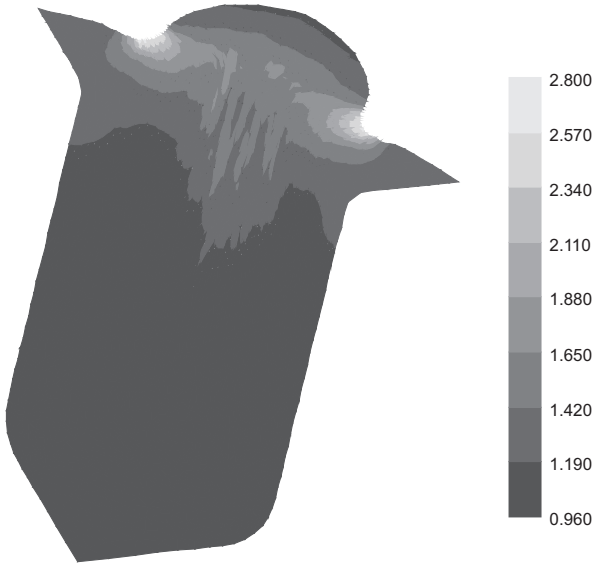

Figure 4.24: Predicted thickness distribution using the Nes model

The calculated thickness distribution is presented in Figure 4.24. It indicates that the simulated local thickening would occur even to about 2.8 mm. However, in the measurements, it was about 1.5 mm at a drawing depth of 170 mm. It is noted that the simulations were performed with constant blank holding force. This means that the pressure on the flange is spreading uniformly on the flange without accounting for the local thickening effects. Consequently, it leads to even more wrong prediction of material flow behavior. Apparently, the simulation result gives the same trend but the absolute values are different.

Figure 4.25, shows the simulated punch force–displacement and thickness distribution from the center of the cup to the flange of the cup for the Nes and the Bergström models. From the thickness distribution plot, more thinning of the wall is observed in the experiments than the simulations. It is noted that the simulations are performed with the material data as was used in the cylindrical cup deep drawing simulations of Al–Mg alloys presented in Section 4.1. Because, the exact material data is not available for the used material. However, it can be concluded that the implemented models are capable of simulating the complex geometries than simple deep drawn cylindrical cups without failure.

4.5 Conclusion

A temperature and strain rate dependent anisotropic material model for finite element analysis of warm forming process was implemented into the in-house implicit finite element code DiekA. The simulations of the uniaxial tests show that the initiation of strain localization can be predicted with a membrane element model. At room temperature the predicted

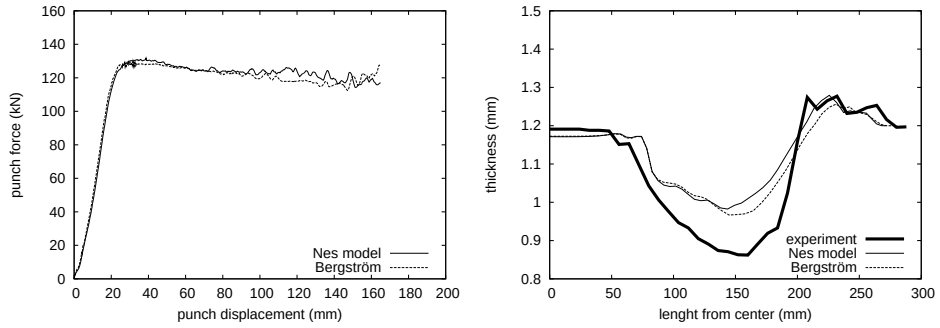

(a) Punch force–displacement curves

(b) Thickness distribution plot

Figure 4.25: Simulation results for warm deep drawn cup at 300 °C using the Nes and Bergström models.

failure strain for AA 5754 corresponds to the experimental ultimate strain. At elevated temperatures, the Nes model predicts the localization strain very well, much better than with the Bergström model.

From the presented simulations of the cylindrical cup deep drawing, it can be concluded that the shape of the yield locus has an important effect on the calculated punch force–displacement curve and also on the predicted thickness distribution. This was demonstrated by the difference in the results obtained for the Vegter and Barlat Yld2000 models.

From the presented warm deep drawing simulations, it can also be concluded that the Nes model performs much better than the Bergström model. The Nes model has more physical basis for the description of plastic deformation.

Generally, the calculated punch force and especially the thickness distributions deviated from experiments. The deviation in thickness distributions is more severe at elevated temperatures. The effect of temperature on the yield locus has an effect notably on the predicted thickness distribution.

The study of temperature effect on yield locus shape was performed mainly to understand the change of earing behavior. It was observed that different slip systems will be activated at elevated temperature. This behavior was mimicked in a crystal plasticity model by assuming that temperature controls the Critical Resolved Shear Stress (CRSS) *i.e.* number of active slip systems. To be used in a macroscopic simulation, the Vegter yield criterion is made temperature dependent by adapting the stress ratios, based on the crystal plasticity analysis. This implementation showed a shift in earing behavior at elevated temperatures. Experimental determination of the earing of cylindrical cups at elevated temperatures presented in Chapter 2, did not give consistent results and is highly sensitive to the tool setup. Hence it is recommended to further investigate the earing behavior in sheet forming processes at elevated temperatures.

The punch force prediction can be improved by adapting the friction coefficients, but that leads to an even thinner predicted bottom area. It is recommended that the friction be investigated in more detail.

5. Stretch Forming with Intermediate Heat Treatments

In the aerospace industry stretch forming is often used to produce skin parts. During stretch forming a sheet is clamped at two sides and stretched over a die, such that the sheet gets the shape of the die. However, for complex shapes it is necessary to use expensive intermediate heat treatments in order to avoid Lüder lines and still achieve large deformations. To optimize this process finite element simulations are performed. The accuracy of finite element analysis depends largely on the material models that precisely describe the work hardening during stretching and work hardening reduction during heat treatments. In this chapter, different material modeling strategies for stretch forming are presented and their predictive capabilities are verified. A leading edge skin part, made of AA 2024 has been chosen for the study.

Firstly, a short introduction of the stretch forming process is given. The material characterization tests on AA 2024 with intermediate heat treatments and their results are briefly described in Section 5.2. These results are used to describe the hardening behavior. Then in Section 5.3, material models for stretching with intermediate heat treatments are considered. The experimental procedure for stretch forming of an aircraft skin part is described in Section 5.4. In Section 5.5, numerical simulations are presented to demonstrate the applicability of the material modeling strategies proposed in this chapter. Finally, the chapter ends with concluding remarks.

5.1 Introduction

Stretch forming is a process in which a desired shape is obtained by stretching a sheet blank or extrusion sections over a tool surface while applying a tensile stress. It is a manufacturing process well suited to the fabrication of parts which are convex in nature, with relatively low levels of bending (McMurray *et al.*, 2009). This often makes stretch forming the process of choice in the aircraft industry for manufacturing of large open shapes such as wing leading edges of aircraft wings and engine cowlings (Straatsma and Velterop, 2004). The basic principles of the stretch forming process of the leading edge of an aircraft wing is shown in Figure 5.1. An advantage of this process is that only one die is needed. The undeformed sheet is clamped with two CNC controllable grippers which can determine the trajectory of deformation of the clamped sheet relative to the die.

The stretch forming of the leading edge can be divided into four steps. During the first step, the sheet is draped around the die without any contact with the die by moving the

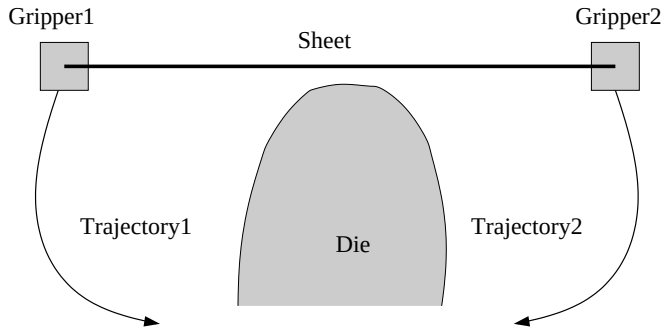

Figure 5.1: Principle of stretch forming.

grippers towards each other. In the second step, the grippers are moved down until the sheet touches the die. During the third stage, the sheet is stretched plastically around the die until the sheet and die are completely in contact. In the last stretching step, extra strains are induced in the sheet by moving the grippers vertically downwards in order to minimize the effect of spring back (Hol, 2009).

The most commonly used material for aircraft skin parts is the heat treatable aluminum alloy AA 2024. In the fabrication of significant doubly curved surfaces using heat treatable aluminum alloy sheet, large strain gradients are induced across the part and lead to surface defects, like Lüder lines and orange peel, which cause to rejection of the components. In order to avoid these failures and still achieve large deformations, a multi-stage forming approach is normally employed. In this procedure several forming steps with intermediate annealing treatments are employed to return the sheet to a more ductile condition (Straatsma and Velterop, 2004; O'Donnell *et al.*, 2008). It has been shown that such an intermediate heat treatment will not fully return the strained sheet to its original condition (Drysdale and Bahrani, 1985).

Traditionally, the forming steps with inter-stage annealing and die shape are defined using production experience and are improved by trial and error. This is a costly and time consuming way that may lead to sub-optimal solutions. Models of the stretch forming process are useful to achieve such an optimal process control. The advantage of models is that they can be used before the tools are made, avoiding lengthy and expensive trial-and-error runs for modifications of the tools and for reducing the number of expensive intermediate annealing steps. "Thorough" models, such as models based on the finite element method are needed to gain fundamental knowledge of the stretch forming process (Jaspart *et al.*, 2004; Wisselink and van den Boogaard, 2005). Hence the goal of the finite element model is to facilitate the optimization of the number and possibly the duration of each intermediate annealing step and therefore of the whole process. However, material models used in the finite element analysis of stretch forming of aircraft skin parts with intermediate heat treatments are still mainly based on phenomenological laws (Wisselink and van den Boogaard, 2005). Hence, further improvement requires the use of a set of thermo-mechanical material models that explicitly consider the effect of microstructure on plastic deformation, the static recovery and the particle coarsening due to precipitation during

intermediate heat treatment (Teyssier and Miroux, 2004). These physical mechanisms should be modeled up to a level that is required for macroscopic process simulations.

5.2 Stretch Forming Characterization Tests for AA 2024

The stretch forming process used for producing the aircraft skin part consists of several deformation steps with intermediate annealing treatments at 340 °C. The annealing treatments remove the strain hardening of the previous step. The material properties of AA 2024 are well known for several tempering conditions, amongst others the high strength conditions (T3, T4, T8 and their derivatives), but also the full-annealed condition (Bray, 1990). However, the properties after intermediate annealing for AA 2024 are unknown. Only a schematic graph of the influence of several ageing and overageing conditions are given by Bray (1990). This graph shows that the strength decreases due to overageing while the strain to fracture only increases upon strong overageing.

A number of tensile tests were performed at National Aerospace Laboratory (NLR) by Stork Fokker and NLR, in order to understand the effect of intermediate annealing steps with stretching. Tests were performed on AA 2024 Clad in T3 condition with a thickness of 1.6 mm. Each sample was first annealed at a temperature of 340 °C for different annealing times, which is a common treatment to relieve stress. After this treatment the samples were given several strain steps with each strain step followed by an intermediate heat treatment. All the samples considered were loaded in the rolling direction with the strains applied in one or two steps (2 %, 4 %, 6 %, and 2×2.5 %). Complete details of these experimental results were published elsewhere (Straatsma and Velterop, 2004; Velterop, 2004). These results are used for validating and comparing the implemented material models in this work. For brevity, the important findings are described here. Straatsma and Velterop (2004) found that the first annealing treatment of T3 causes a large decrease of the mechanical properties like the ultimate tensile strength decreases from 440 MPa to 290 MPa, yield strength drops from 340 MPa to 170 MPa and fracture strain decreases from 17 % to 10 %. An annealing time of 20 minutes is sufficient for recovery of deformation structures caused by up to 6 % stretching. Particularly, tensile and yield strengths decrease significantly due to 20 minutes annealing at 340 °C during the first annealing step. Consecutive strain steps and intermediate anneals slightly decrease the tensile strength and increase the yield strength. There is no influence of the material batch. A representative set of true stress–strain curves of these experiments is presented in Figure 5.2.

The initial material was in T3 condition *i.e.* it was solutionized, cold deformed and aged at room temperature. Due to this ageing, very small precipitates and/or GP zones are present. During the successive annealing at 340 °C several phenomena can happen: recrystallization, recovery, precipitation/coarsening of the particles. The microstructure evolution during stretch forming with intermediate annealing of AA 2024 was investigated by Teyssier and Miroux (2004). They focused mainly on understanding the relationship between the evolution of the microstructure, effect of chemical composition and the changing mechanical properties during the stretch forming with intermediate heat treatments.

Electrical resistivity measurements were performed to follow precipitation. The observed sharp decrease of resistivity during the first annealing on T3 condition (initial material) indicates a decrease of the solute content accompanying the nucleation and/or growth

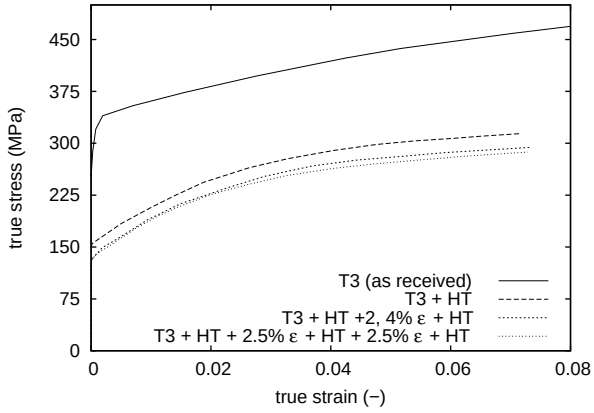

Figure 5.2: Experimental stress–strain curves with intermediate heat treatments (HT: heat treatment at 340 °C for 20 minutes).

of precipitates. Optical and scanning electron microscopy were used to measure the grain size and the size and density of precipitates. From the micrographs, no evidence of recrystallization was found as there was no nucleation or growth of new grains Teyssier and Miroux (2004). Recovery and precipitation kinetics were determined from the hardness measurements. X-ray diffraction analysis (XRD) was used to identify the different types of precipitates present during heat treatments.

The decrease of mechanical properties during first annealing can be explained by the overageing, *i.e.* coarsening of particles, even if extra precipitation may occur. During the subsequent annealing treatments, no visible new precipitates were observed, *i.e.* the density of the precipitates is constant and only coarsening mechanism plays a dominant role.

Recovery may happen during the first annealing and more surely during the following annealing steps to remove the work hardening introduced by stretch forming passes.

5.3 Material Model

To describe the deformation due to stretch forming, the microstructural based Nes work hardening model is used. To describe the particle coarsening and static recovery during intermediate heat treatments, simple empirical equations based on physical observations are used.

5.3.1 Work Hardening

For the description of the work hardening in AA 2024, the Nes model described in Section 3.6 is used with the following simplifications. As the stretch forming of aircraft skins takes place at room temperature, the temperature and strain rate effects are negligible. In the dynamic recovery process, the subgrain growth described by the Equation (3.54), occurs only during deformation beyond stage III in the elevated temperature range. Hence the effect of subgrain

growth is also neglected in this analysis. Further simplifications to the Nes model are made by neglecting the DSA effect described by Equations (3.58)–(3.60) due to very little Mg solute content of the material. The calculation time could be reduced considerably by using a simplified isothermal implementation of the Nes model.

In age hardening aluminum alloys, the strengthening effect mainly comes from precipitation hardening due to shearing and bypassing of particles by dislocations and solid solution hardening effects (Shercliff and Ashby, 1990a,b; Deschamps and Bréchet, 1999a,b). Shearing is possible only if the interface between particle and matrix is coherent *i.e.* continuity of the crystal structure but not necessarily the same inter-atomic distances. Bypass or Orowan mechanism occurs if the interface between particle and matrix is incoherent (Reppich, 1993). Precipitates can also indirectly contribute to the strengthening of alloys by influencing the storage of dislocations during microstructure evolution.

In the present model, the contribution due to precipitates for the strengthening is described according to Myhr *et al.* (2001). The particles are assumed to be spherical and of equal size (*i.e.* monodispersive). This means that the constituent equations were derived on the basis of the classical analytical solutions for the dislocation-particle interaction. According to Myhr *et al.* (2001) the stress contribution due to a population of precipitates with a mean radius r and volume fraction f_r is given by:

$$\tau_p = (2\beta G b^2)^{(-1/2)} \frac{1}{br} \left(\frac{3f_r}{2\pi}\right)^{1/2} F_{s,0}^{3/2} \tag{5.1}$$

$F_{s,0}$ is the force at which one dislocation will pass one particle:

$$F_{s,0} = 2\beta G b^2 \min\left[\left(\frac{r}{r_c}\right)^{3/2}, 1\right] \tag{5.2}$$

This gives

$$\tau_p = 2\beta G \frac{b}{r} \left(\frac{3f_r}{2\pi}\right)^{1/2} \min\left[\left(\frac{r}{r_c}\right)^{3/2}, 1\right] \tag{5.3}$$

r_c is the critical radius deciding between shearing and bypassing mechanisms. In the above equations, G is the shear modulus of the aluminum matrix, b is the length of the Burgers vector and β is a constant close to 0.5. The precipitate size and volume fractions (input parameters) are determined by fitting the proportional limit to experimental measurements for different stretching and consecutive heat treatments presented in Figure 5.2 with Equation (5.3).

In age hardening aluminum alloys solid solution elements such as Mg, Si and Cu give rise to considerable work hardening. In the Nes model the interactions between the mobile dislocations and the dislocation substructure, solute content and particles are treated in terms of a combined effect due to both short- and long- range stresses given in Equations (3.30) and (3.31) respectively.

In the model, the initial dislocation ρ_0 was chosen to be $10^{11}\,\mathrm{m}^{-2}$ by assuming the material is fully recovered after the first heat treatment on initial material in T3 condition at 340 °C for 20 minutes. An average grain size of 16 μm was measured and used in the simulations. Solute concentrations come from the mass balance. The initial dislocation

Table 5.1: Volume fraction and size of the particles calculated for different stretching and consecutive heat treatments.

Condition	vol. fraction (%)	particle size (m)
T3	1.3	$5.0 \cdot 10^{-9}$
T3 + HT	1.3	$13.4 \cdot 10^{-9}$
T3 + HT + 2 to 6% stretching + HT	1.3	$16.6 \cdot 10^{-9}$

density ρ_0 in T3 condition is obtained by fitting the proportionality limit of the model to the experimental one. It was found to be equal to $3.1 \cdot 10^{13}\,\mathrm{m}^{-2}$.

The sensitivity study of the Nes model in respect to the model parameters shows that only two parameters have a significant influence on the stress–strain relation:

- q_c controls the work hardening (storage of dislocation and subgrain formation and misorientation)
- ξ_ρ controls the dynamic recovery.

Both parameters have a roughly similar effect on the stress–strain curve so an infinite number of combinations of these parameters can fit the experimental stress-strain curves. However, each combination gives a different result for the dislocation density and subgrain evolution. The q_c and ξ_ρ parameters are obtained by fitting the stress–strain curves on the material after first heat treatment on initial material in T3 condition at 340 °C for 20 minutes giving the most realistic dislocation density and subgrain size. The fit of the strain–stress curve is not perfect for all strains, which is clearly visible in Figure 5.3. All the other parameters have negligible influence when they are varied within their range of possible values. Default values are used based on the literature and the selected and fitted parameters of the Nes model are presented in Table 5.2.

Table 5.2: Parameters of the Nes model for AA 2024 (T3 + HT).

ν_D	$1.0 \cdot 10^{13}\,\mathrm{s}^{-1}$	b	$2.86 \cdot 10^{-10}\,\mathrm{m}$	κ	$1.3 \cdot 10^{-23}\,\mathrm{J/K}$
q_c	18.0	C	40.0	f	0.1
α_1	0.3	α_2	3.0	κ_0	$3.5\,\mathrm{m}^{-1}$
U_s	$1.5 \cdot 10^5\,\mathrm{J/mol}$	U_sd	$1.3 \cdot 10^5\,\mathrm{J/mol}$	U_t^s	$1.5 \cdot 10^5\,\mathrm{J/mol}$
κ_2	2.0	κ_3	0.7	φ_c	0.3489
B_t	57.0	ω_t	20.0	e_t	0.54
B_ρ	0.23	ξ_ρ	45.0	ω_s	1.0
e_ρ	0.67	B_δ	100.0	ξ_δ	20.0
e_δ	0.65	ρ_0	$1.0 \cdot 10^{11}\,\mathrm{m}^{-1}$	S_{IV}	0.15
q_IV	2.0	φ_IV	0.052 rad	m	0.8
r	$13.4 \cdot 10^{-9}\,\mathrm{m}$	f_r	0.013	β	0.36
r_c	$5.0 \cdot 10^{-9}\,\mathrm{m}$	c	0.0042		

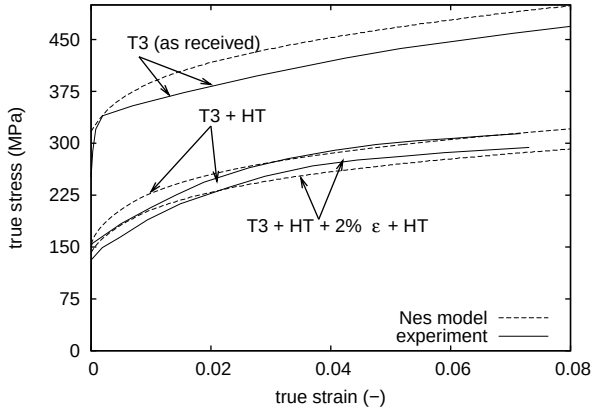

Figure 5.3: True stress–strain curves with intermediate heat treatments—experiments and model (HT: heat treatment at 340 °C for 20 minutes).

5.3.2 Isothermal Ageing Model

During age hardening, Guinier Preston (GP) zones nucleate and grow from the quenched solid solution and deplete it. During the *nucleation* phase, the radius of the particles is considered constant and the volume fraction is variable. When the solubility limit is reached, precipitates coarsen by competitive *growth* and in the model the radius of the precipitates is considered as a variable and the volume fraction of the precipitates becomes constant. It was found in the experiments of Teyssier and Miroux (2004) that nucleation of GP zones is observed mainly during the first 2 minutes of initial heat treatment at 340 °C for 20 minutes on T3 condition and no or very little nucleation of GP zones were observed in the consecutive heat treatments. Hence, ageing is controlled by the coarsening kinetics and the particle coarsening effects are considered by a relatively simple empirical expression. Coarsening is described here by the growth of the mean particle radius r of assumed spherical shape with time t. No attempt has been made at present to include changes in particle shape or in the distribution of particle size during coarsening, though it is acknowledged that these can be important effects. According to Shercliff and Ashby (1990a); Rylands *et al.* (1994), the size evolution in each annealing sequence is:

$$r = \left(r_i^n + kt\right)^{1/n} \tag{5.4}$$

with

$$k = \frac{k_0}{T} \exp\left(-\frac{Q}{RT}\right) \tag{5.5}$$

where Q is the activation energy for volume diffusion of Cu atoms between particles which is equal to 136 kJ/mol, R is the universal gas constant, t is the process annealing time and the bulk diffusion coefficient $n = 3$ is considered in the simulations. k_0 is then obtained by fitting the predicted particle radius presented in Table 5.1 and equal to $4.5 \cdot 10^{-13}\mathrm{K{\cdot}m^3/s}$.

5.3.3 Static Recovery Model

The term "recovery" refers to the restoration of material properties back to their original or undeformed state after heavy deformation and prior to recrystallization (Kuo and Lin, 2007). Static recovery is specifically attributed to the process that occurs after deformation whereas dynamic recovery takes place during the course of deformation. It is well known that recovery of most metals is primarily due to changes in the dislocation structure (Humphreys and Haterly, 2004). Dislocation recovery is not a simple microstructural change, but is constituted by a series of events: dislocation tangling immediately after deformation, dislocation cell formation, annihilation of dislocations within cells, subgrain formation and subgrain growth (Nes, 1994; Humphreys and Haterly, 2004). The coarsening of the dislocation cells or subgrains is summarized as static recovery during the annealing processes.

In this work, an empirical approach based on physical observations of recovery kinetics based on type 2 model of Humphreys and Haterly (2004) is used. According to Humphreys and Haterly (2004), if the variable measuring the amount of hardening remaining in the material is X_{R}, then the kinetics of recovery, $\mathrm{d}X_{\mathrm{R}}/\mathrm{d}t$ is defined as follows:

$$\frac{\mathrm{d}X_{\mathrm{R}}}{\mathrm{d}t} = -BX_{\mathrm{R}}^{q} \tag{5.6}$$

Taking

$$X_R = \frac{\sqrt{\rho} - \sqrt{\rho_0}}{\sqrt{\rho_{\mathrm{d}}} - \sqrt{\rho_0}} \tag{5.7}$$

The total dislocation density evolution due to recovery kinetics is given by:

$$\rho = \left[\sqrt{\rho_0} + \left(\sqrt{\rho_{\mathrm{d}}} - \sqrt{\rho_0}\right)\left(1 + (q-1)Bt\right)^{\left(-\frac{1}{q-1}\right)}\right]^2 \tag{5.8}$$

where ρ_0 is the total dislocation density of fully soft material, ρ_{d} is the dislocation density of deformed configuration just before annealing and t is the annealing time. The recovery kinetics parameters B and q are temperature dependent and fitted for the temperatures of interest. Usually the exponent q is found to be in the range of 3 to 5; and $q = 4$ is chosen in this work.

Coupling with the Nes Model and Application to AA 2024

When deforming the material after annealing, it is expected that the deformation of the recovered structure starts with stage II. Therefore the in-cell dislocation density during recovery is related to the total dislocation density using the same scaling relation as during stage II:

$$\rho_{\mathrm{i}} = \frac{\rho}{f\left(q_{\mathrm{b}}^2 - 1\right) + 1} \tag{5.9}$$

The fully soft dislocation density is taken as $\rho_0 = 10^{11}\mathrm{m}^{-2}$ According to the experimental results, 20 minutes annealing at 340 °C is supposed to be enough to obtain a fully recovered microstructure. The parameter B is then chosen in such a way that ρ_{i} gets close to ρ_0 after 20 minutes annealing at 340 °C. It is found that after a sharp decrease, ρ_{i} decreases

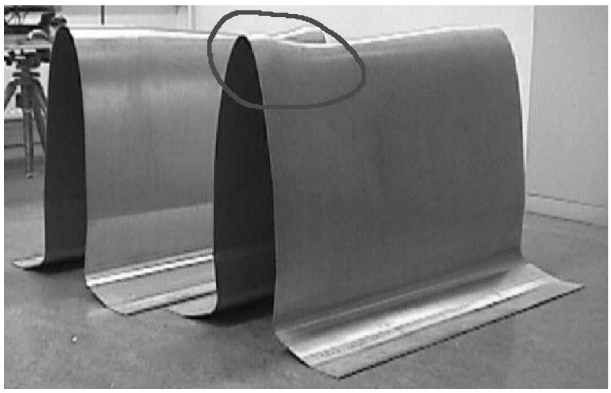

Figure 5.4: Skin parts after stretch forming.

only slowly with time, whatever the value of B. A value of $B = 0.1\text{s}^{-1}$ is chosen as a compromise between the value of ρ_i after 20 minutes annealing at 340 °C and the rate of decrease of ρ_i at the beginning of annealing.

5.4 Experimental Stretch Forming of Aircraft Skins

A number of sheets have been stretched using manually determined trajectory of the grippers. The dimensions of the sheet are $1130 \times 1920 \times 3.5$ mm. Five intermediate heat treatments are used. To measure the strain in the final part a grid of dots with known dimensions was applied to the undeformed sheet. Due to the large dimensions of the sheet only part of the sheet which is known to deform mostly was digitized. The final part is shown in Figure 5.4.

The PHAST$^{\text{TM}}$ strain measurement system (Atzema, 2003) has been used to measure the strains after stretch forming. This system is based on 3D image processing. Digital photos are taken from different positions of the product and some beacons. The strains are calculated from the recognized grid points and beacons (Figure 5.5) using photogrammetry.

A correction in the thickness calculation must be considered as it was calculated from the strains measured from the outer plane of the sheet instead of midplane. In this case the thickness is corrected up to 0.1 mm, as was confirmed by direct thickness measurements at the edges.

5.5 Finite Element Simulations

The initial shape of the sheet and tools is shown in Figure 5.6. As the geometry of the die is symmetric and therefore the geometry of the final product is also symmetric only half of the sheet is modeled. The part of the sheet that is clamped between the gripper jaws is not modeled, as ideal clamping is assumed. The prescribed displacement boundary conditions

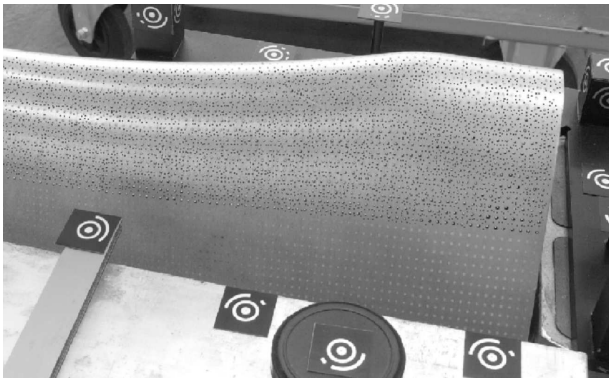

Figure 5.5: Parts with recognized grid points and beacons.

are applied to the remaining edges of the sheet in the gripper jaws. The cheeks are modeled as cylinders. Both cheek nodes and prescribed sheet nodes are given the same prescribed displacements.

It can be seen in Figure 5.6 that the initial shape of the sheet is curved, which agrees with the industrial practice as the sheet is slightly bent before clamping it into the machine. The initial curvature is modeled by taking the initial shape of the sheet equal to a shallow cosine. This shape is equal to the shape of the buckle mode of a compressed sheet. In this example the edges of the sheet are moved only 15 mm inwards. It is assumed that this bend causes no stresses and plastic deformations in the sheet. By modeling this initial cosine shape it is ensured that the sheet deforms in the correct upward direction, when the sheet is draped around the die in the first part of the stretch process. This also avoids numerical instabilities during the finite element simulation.

The cheeks and die are assumed to be rigid bodies, *i.e.* they are undeformable with respect to the sheet. A penalty method is used to describe the contact between the rigid tools and the sheet. The friction between the sheet and rigid tools (die and cheeks) is described with Coulomb's friction model with a friction coefficient of 0.1 .

The sheet has been meshed with 2810 triangular elements with a refinement close to the symmetry line. The size of the element edges ranges from 20 to 40 mm. The used discrete Kirchhoff shell elements (Batoz and Lardeur, 1989), take membrane as well as bending stiffnesses into account.

The used trajectory of the grippers is shown in Figure 5.7. It is a piecewise linear approximation of the trajectory used for the experiments. The rotations of the grippers have been neglected, as they are relatively small. The positions at which an intermediate heat treatment is given to the sheet are marked.

Two different hardening models: a phenomenological power law model and the physically based Nes model are used for the simulations. To describe the anisotropy and biaxial behavior of the sheet, the Vegter yield function presented in Chapter 3 is used and the input parameters are given in Table 5.3.

In the complete stretch forming process on a saddle-shaped skin part, the sheet was

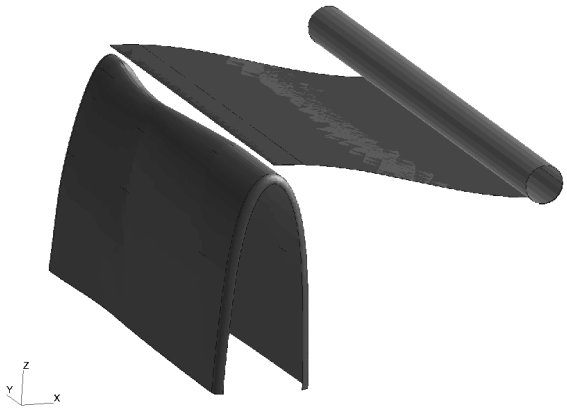

Figure 5.6: Initial Sinusoidal shape of sheet and tools.

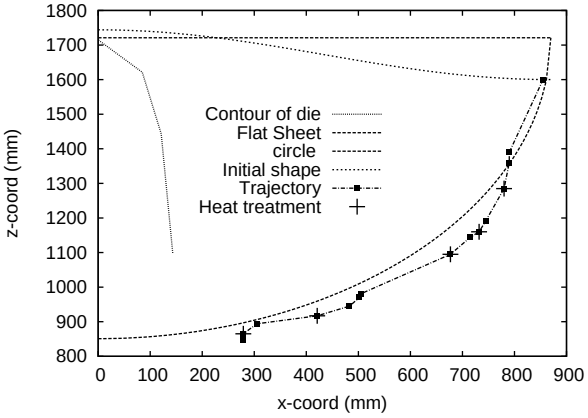

Figure 5.7: Trajectory of the grippers used in the simulation.

Table 5.3: Measured stress and strain ratios for the AA 2024-O sheet (Vegter yield locus data).

angle with RD	0°	45°	90°
$(\sigma_1/\sigma_1^{\mathrm{RD}})_{\mathrm{un}}$	1.0	0.98	0.99
f_{ps}	1.14	1.1	1.09
f_{sh}	0.576	0.579	0.577
f_{bi}	0.96		
R-value	0.52	0.67	0.52
$(\varepsilon_2/\varepsilon_1)_{\mathrm{bi}}$	1.0635		

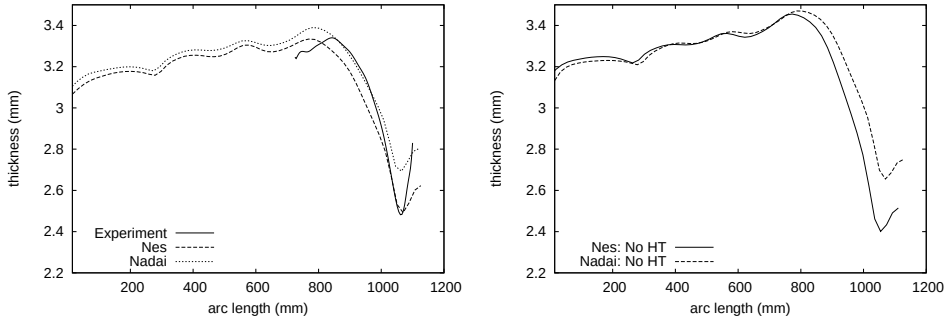

(a) with heat treatment (b) without heat treatment

Figure 5.8: Thickness along symmetry line with and without heat treatments (HT).

annealed 5 times. After sufficient annealing time, mechanical properties are restored due to the physical mechanisms of particle coarsening and recovery of the stored dislocations. In the simulation the annealing step is included by using the simple models for particle coarsening and static recovery presented in Section 5.3.2 and Section 5.3.3 respectively. During the heat treatment, the new values for the precipitate size and total dislocation density for a given annealing temperature and time are calculated. Further deformation steps are continued using the physically based Nes work hardening model with the reset values of precipitate size and dislocation density at every integration point of the DKT elements. In the case of the power law model, the annealing step is included only phenomenologically by resetting the (equivalent) plastic strain to zero, thus deleting complete work hardening in all integration points.

In Figure 5.8 the thickness along the symmetry line is presented after all stretching phases with and without heat treatments for the Nes and Nadai models. With heat treatments, the deformations are stable and they are almost completely kinematically determined. The physically based Nes model gives better thickness prediction, particularly at the critical region of the part, than the phenomenological Nadai model (see Figure 5.8(a)). From the die force–gripper displacement diagram in Figure 5.9(a) where the die force drops to zero immediately after first heat treatment for the Nadai model, the stress and strain values at every integration point are reset to zero. For the Nes model, the force does not completely drop to zero because the work hardening effect is not completely deleted and residual stresses are left in the material. This is also evident from the predicted equivalent plastic strain in the final part with heat treatment presented in Figure 5.10. The Nes model predicts a higher equivalent plastic strain than the Nadai model.

From Figure 5.9(b), without intermediate heat treatments steps, the die force is higher as there is no removal of work hardening. Correspondingly without heat treatments, more thinning is observed in the critical region of the part shown in Figure 5.8(b). This thinning is more severe with the Nes model. Apart from the heat treatments, a drop in vertical force on die, for example for the gripper displacement between 500 mm to 600 mm, corresponds to loss of contact between the die and the sheet.

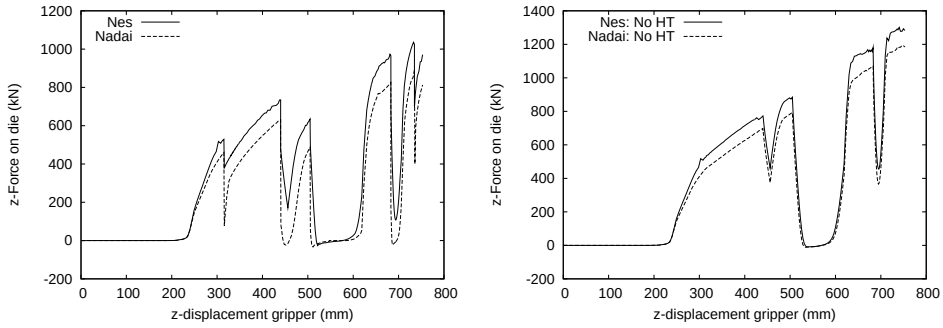

(a) with heat treatment (b) without heat treatment

Figure 5.9: Vertical force on die with and without heat treatments (HT).

In Figure 5.11, the effect of different approaches for heat treatments are studied. In this study, simulations are performed with a physics based approach for heat treatments by considering the particle coarsening and static recovery and a phenomenological approach *i.e.* assuming the work hardening effect is completely removed by resetting plastic strains to zero. Simulations are also performed without intermediate heat treatments. In all the three situations, the work hardening effect is described using the physically based Nes model. From Figure 5.11(a), it is clearly seen that the force–displacement curve is more stable with the physically based approach for heat treatments than the phenomenological approach as it shows the jiggles in the force–displacement curve. With the phenomenological approach, after every intermediate heat treatment the vertical force on the die drops to zero as the strains are completely removed. However, this is not completely realistic. From the thickness along the symmetry line plot shown in Figure 5.11(b) follows that with the phenomenological approach the thinning effect in the critical region is overestimated and the physically based approach is much better. Without heat treatments too much thinning effect is observed.

5.6 Conclusions

The main objective of the work is to develop and use a suitable numerical model for the finite element analysis of the stretch forming of aircraft skin parts with intermediate heat treatments. An important part of the numerical model is the modeling of the material behavior. Both the hardening behavior during the stretching process, and the reduction of work hardening behavior during the heat treatment process are considered. Two hardening models are compared: a phenomenological Nadai hardening model and a physically based model according to Nes. The reduction in work hardening during heat treatment is modeled by considering the underlying physics such as the overageing model for particle coarsening and the static recovery model. A phenomenological approach is also used for the comparison by deleting all work hardening effect from the previous stretching phases.

From the presented simulations, it can be concluded that primarily the physics based material modeling gives better results. The predicted thickness distribution especially in

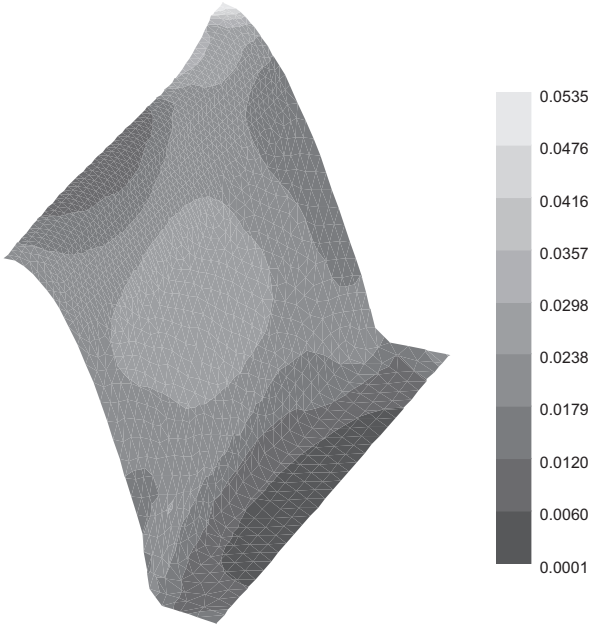

(a) Nes model

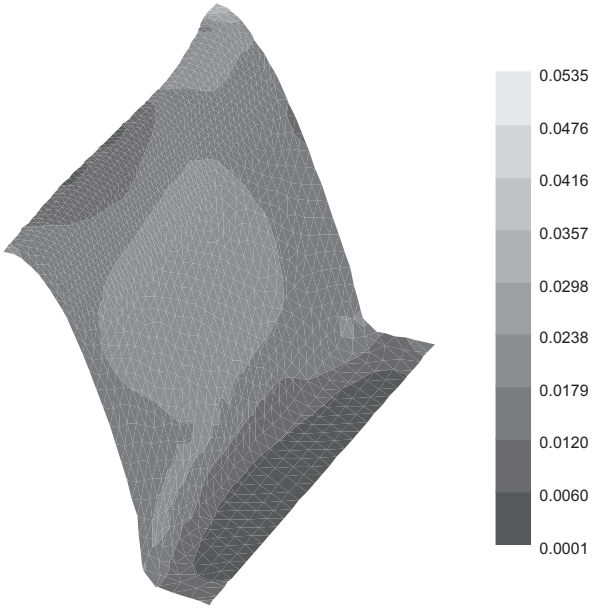

(b) Nadai model

Figure 5.10: The predicted equivalent plastic strain in the final product with heat treatments.

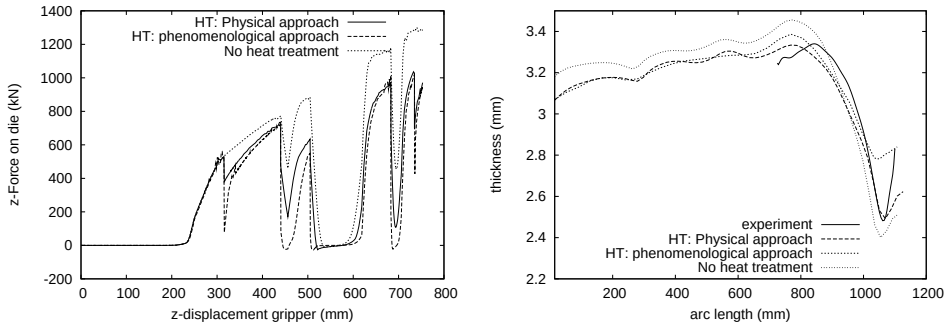

(a) Vertical force on die

(b) Thickness along symmetry line

Figure 5.11: Influence of heat treatment on predicted vertical force on die and thickness along symmetry line.

the critical region of the part using the Nes model for work hardening; and the overageing and static recovery models for intermediate annealing give better agreement with the experiments.

In this work the material models are compared only with uniaxial experiments and the predicted thickness distribution from simulations are used for the validation. In order to have more confidence in the implemented material models, further validation of FEM results such as the vertical force on die and the strain distribution are useful. There is also room for improvement in the material modeling as in the current models, the effect of particle coarsening and static recovery are treated separately. In reality, the effect of particle coarsening and recovery on the reduction of work hardening during heat treatments is coupled.

6. Conclusions and Recommendations

In this thesis, the numerical modeling of thermally assisted forming of aluminum sheet is presented. In thermally assisted forming of aluminum, the mechanical loading is combined with a thermal component *e.g.* deformation at elevated temperatures and annealing between deformation steps. The most important part of numerical simulation of a thermo-mechanical forming process is the constitutive model to describe the material behavior under different process conditions and the thermo-mechanical finite element model. In this chapter, conclusions from the research are presented and recommendations are given for further research.

Warm Forming

Material Modeling An important difference between cold forming and warm forming is caused by the strain rate sensitivity of aluminum at temperatures above 125 °C. For cold forming, the material behavior is completely determined by work hardening and rate effects can be neglected. For warm forming of aluminum alloys apart from the work hardening effects, the strain rate sensitivity over the complete range from room temperature up to 250 °C should be well represented. Hence, material models for warm sheet forming are more complex than for cold forming.

In this work on warm forming, three different automotive aluminum alloys are considered: a non-heat treatable Al–Mg alloy (AA 5754-O), and two variants of heat treatable Al–Mg–Si alloys (AA 6016 and AA 6061) at different tempering conditions. In Al–Mg alloys, hardening is mainly due to the presence of solute atoms in solid solution, which causes lattice distortions that impede the dislocation motion. On the other hand, in Al–Mg–Si alloys strengthening is determined by the precipitates formed during ageing (heat) treatment and therefore control of precipitation during ageing treatment is critical for attaining optimal material behavior. Hence apart from the strain rate and temperature effects, material models will also need to consider the effects of solutes and precipitates on work hardening. Material models based on consideration of the underlying physical processes are expected to have a larger range of usability in this respect. These type of models based on the evolution of microstructure and dislocation density are called physically based models.

Two mainstream dislocation based hardening models were used in this thesis, a one parameter model (total dislocation density)—the Bergström model—and a more advanced three parameter model (dislocation density inside the cell, cell size and misorientation between cells)—the Nes model, to describe the evolution of microstructure. The Nes model directly takes into account the chemical composition such as solute concentration of different constituents, grain size, volume fraction and size of the precipitates. Hence, the Nes

model is quite capable of describing the changing material behavior due to ageing of heat treatable Al–Mg–Si alloys. In Al–Mg alloys, dynamic strain ageing effects can be seen in the experimental results, *i.e.* up to 100 °C, a low strain rate gives higher stresses and high strain rate gives lower stresses. This phenomenon is covered by the Nes model.

The Nes model relies on a multi-parameter microstructure description, for which a lot of parameters are unavoidable. However, very few parameters (maximum 4 parameters) are fitted parameters which are identified from the experimental flow curves at different temperatures and strain rates and the remaining parameters are almost equal for aluminum alloys. The Nes model can describe the experimental stress–strain curves better than the Bergström model.

A large difference between the two hardening models is observed when strain rate jumps are modeled. After a strain rate increase, the Bergström model predicts a gradual changing stress towards the flow stress curve that corresponds to the higher strain rate. With the Nes model, an initial jump in the flow stress is observed, followed by asymptotically approaching the higher strain rate curve, which is a better representation of the experiments. On a strain rate decrease, the stress in the experiments dropped very fast. Nevertheless, the Nes model represents this behavior better than the Bergström model, but not as good as in the case of strain rate increase from lower to higher using the Nes model. In sheet forming processes, strain rates are generally not constant, therefore it is recommended to fine tune the parameters which are influencing the strain rate effects in the Nes model in order to better describe the material behavior at changing strain rates.

In the simulations, the biaxial and anisotropic behavior of the aluminum sheet is described using two advanced yield functions: Vegter and Barlat Yld2000. The Vegter yield function is directly based on the experimentally measured yield stresses and strain ratios in simple shear, uniaxial, plane strain and equi-biaxial states in RD, TD and 45 ° to the RD. The Barlat Yld-2000 yield function is derived based on the approach of linear transformations of a stress tensor. The input parameters of the Barlat Yield function are identified from the uniaxial tensile tests in RD, TD and 45 ° to the RD; and from the equi-biaxial stress and strain ratios.

Finite Element Modeling Simulation of aluminum sheet forming at elevated temperatures requires the solution of a thermo-mechanically coupled set of equations. The high conduction coefficient and low thickness of the aluminum sheet makes sure that the temperature is almost constant across the sheet thickness. Hence, Shell elements are used with only one thermal d.o.f. per node. The gradient in the thickness direction need not be modeled. Because of the large heat capacity of the tools, the temperature of the tools is not much affected by the blank. The stiffness of the tools is also much greater than that of the blank. It is therefore justified to model the tools as rigid contours with prescribed temperatures.

The simulations of the uniaxial tests show that the initiation of strain localization can be predicted with a membrane element model. At room temperature the predicted failure strain corresponds to the experimental ultimate strain. At elevated temperatures, the Nes model predicts the localization strain very well, much better than with the Bergström model.

From the warm deep drawing simulations, it can be concluded that the Nes model performs much better than the Bergström model as the Nes model has more physical basis for the description of plastic deformation. In the simulations, the effect of temperature on

anisotropy is studied by identifying the Vegter yield data from crystal plasticity analysis by assuming the activation of more slip systems at elevated temperatures. Including the use of temperature effects on yield data notably improves the thickness prediction at the bottom of the cup and predicts the earing behavior with four ears in $45°$ to the RD and TD. It is, however, different from without consideration of temperature effect, where in four ears are observed along RD and TD.

The effect of anisotropy in deep drawing is generally viewed based on the number of ears, their location with respect to rolling direction and their amplitude. Experimental determination of the earing of cylindrical cups at elevated temperatures did not give consistent results and are highly sensitive to the tool setup. In a first series of experiments, at room temperature, the earing profile exhibited four ears in RD and TD, whereas at elevated temperatures the earing profile exhibited two ears at TD. In the second series of experiments the earing profile at elevated temperature nearly exhibited four ears with reduced amplitudes along RD and TD. The earing profiles from the third series of experiments is completely different from the previous series of experiments by showing an irregular earing profile. However, the earing profiles are reproducible in a series. Hence it is recommended to further investigate the earing behavior in sheet forming processes at elevated temperatures.

Stretch Forming with Intermediate Heat Treatments

The main objective of this work is to develop and use a suitable numerical model for the finite element analysis of the stretch forming of an aircraft skin part with intermediate heat treatments. This can only be accomplished by predicting the material behavior correctly during stretching as well as during intermediate annealing steps. In this work, the material behavior during stretching was modeled by two hardening models. A completely phenomenological power law model and the physically based Nes model. The removal of residual stresses during heat treatments is modeled first phenomenologically by resetting all plastic strains to zero and another approach based on considering the underlying physics such as the particle coarsening and the recovery of dislocations during heat treatment.

It can be concluded from the simulation of aircraft skin parts with intermediate heat treatments that the physics based material modeling gives better results. The predicted thickness distribution especially in the critical region of the part using the Nes model for work hardening; and the overageing and static recovery models for intermediate annealing gives better agreement with the experiments. The material models are compared mainly with uniaxial flow curves and the predicted thickness distribution from simulations are used for validation. Hence it is highly recommended to further validate numerical results with experimental results to gain more confidence in the implemented material model.

In this work, mainly numerical results in terms of material modeling are discussed. It is further recommended to combine this material modeling approach with the optimization algorithm to optimize the trajectory of the grippers and thereby determine where heat treatments should be applied.

A. Continuum Mechanics

This appendix contains a number of continuum mechanics equations that are frequently used in the mathematical formulation of sheet metal forming problems. A more complete overview can be found in many textbooks *e.g.* Malvern (1969); Chadwick (1976); Bowen and Wang (1989); Brown (2009).

A.1 Kinematics and Strains

A change in the configuration of a continuum body results in a displacement. The displacement of a body has two components: a rigid body displacement and a deformation. A rigid body displacement consists of a simultaneous translation and rotation of the body without changing its shape or size. Deformation implies the change in shape and/or size of the body from an initial or undeformed configuration Ω_0 to a current or deformed configuration Ω_t (Figure A.1).

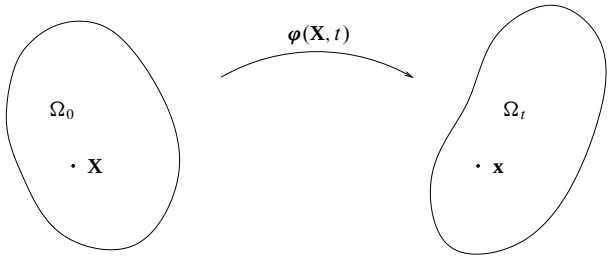

Figure A.1: Deformation of body Ω_0 in the reference configuration to the current configuration Ω_t.

The material deformation gradient tensor $\mathbf{F}(\mathbf{X}, t)$ is a second-order tensor that represents the gradient of the mapping function $\boldsymbol{\varphi}(\mathbf{X}, t)$, which describes the *motion of a continuum*. The material deformation gradient tensor characterizes the local deformation at a material point with position vector $\mathbf{X}$ by *transforming* a material line element emanating from that point from the *reference configuration* $\mathbf{X}$ to the *current* or *deformed configuration* $\mathbf{x}$, assuming continuity in the mapping function $\boldsymbol{\varphi}(\mathbf{X}, t)$. Thus we have,

$$\mathbf{F}(\mathbf{X}, t) = \frac{\partial \boldsymbol{\varphi}(\mathbf{X}, t)}{\partial \mathbf{X}} \tag{A.1}$$

The *Jacobian* (determinant) of the deformation gradient represents the volume ratio of the current configuration with respect to the reference configuration, hence: $J = \det \mathbf{F} > 0$. The deformation gradient $\mathbf{F}$, like any second-order tensor, can be decomposed, using the polar decomposition theorem, into a product of two second-order tensors: an orthogonal tensor and a positive definite symmetric tensor

$$\mathbf{F} = \mathbf{R} \cdot \mathbf{U} = \mathbf{V} \cdot \mathbf{R} \tag{A.2}$$

where the tensor $\mathbf{R}$ is a proper orthogonal tensor, *i.e.* $\mathbf{R}^{-1} = \mathbf{R}^{\mathrm{T}}$, representing a rotation; the tensor $\mathbf{U}$ is the right stretch tensor; and $\mathbf{V}$ the left stretch tensor. The terms *right* and *left* means that they are to the right and left of the rotation tensor $\mathbf{R}$, respectively. $\mathbf{U}$ and $\mathbf{V}$ are both positive definite. The polar decomposition can be interpreted as a rigid rotation after deformation or vice versa.

Several rotation-independent deformation tensors are used in solid mechanics. The most popular of these are the right and left Cauchy-Green deformation tensors defined as follows

$$\mathbf{C} = \mathbf{F}^{\mathrm{T}} \cdot \mathbf{F} = \mathbf{U}^2 \tag{A.3}$$

$$\mathbf{B} = \mathbf{F} \cdot \mathbf{F}^{\mathrm{T}} = \mathbf{V}^2 \tag{A.4}$$

With the introduction of $\mathbf{C}$ and $\mathbf{B}$, the most widely used Green-Lagrange strain tensor and Euler-Almansi strain tensor are defined.

$$\mathbf{E} = \tfrac{1}{2}(\mathbf{C} - \mathbf{I}) \tag{A.5}$$

$$\mathbf{e} = \tfrac{1}{2}(\mathbf{I} - \mathbf{B}^{-1}) \tag{A.6}$$

Plasticity theories often require measures of the *rate* of deformation of a solid, such as strain rate in the deformed configuration. The material time derivative of $\mathbf{x}$ is the velocity $\mathbf{v}$ of the material point $\mathbf{X}$:

$$\mathbf{v} = \dot{\mathbf{x}} = \frac{\partial \boldsymbol{\varphi}(\mathbf{X}, t)}{\partial t} \tag{A.7}$$

The local change of current configuration (deformation and rotation) in rate form is given by the *velocity gradient* $\mathbf{L}$. It is often more convenient to express $\mathbf{L}$ in terms of coordinates in the reference configuration by noting that

$$\mathbf{L} = \frac{\partial \mathbf{v}}{\partial \mathbf{x}} = \dot{\mathbf{F}} \cdot \mathbf{F}^{-1} \tag{A.8}$$

The velocity gradient can be decomposed in the rate of deformation tensor $\mathbf{D}$ and the spin tensor $\mathbf{W}$:

$$\mathbf{L} = \mathbf{D} + \mathbf{W} \tag{A.9}$$

where $\mathbf{D}$ is the symmetric part and $\mathbf{W}$ the skew-symmetric part of $\mathbf{L}$. In elasto-plastic analysis of metals, the rate of deformation is commonly decomposed in an elastic and a plastic part

$$\mathbf{D} = \mathbf{D}^{\mathrm{e}} + \mathbf{D}^{\mathrm{p}} \tag{A.10}$$

A.2 Stresses

Stresses are the response to a certain deformation of body. Stresses can also occur due to changing temperatures in the body without deformation. These are referred to as thermal stresses. In continuum mechanics, the stress tensor $\boldsymbol{\sigma}$, introduced by Cauchy, is a measure of the average amount of force exerted per unit area of a surface.

The other stress measures regard forces as acting on the undeformed solid. Consequently, to define them it must be known not only what the deformed solid looks like, but also what it looked like before deformation.

Kirchhoff stress:

$$\boldsymbol{\tau} = J\boldsymbol{\sigma} \tag{A.11}$$

First Piola-Kirchhoff stress:

$$\mathbf{P} = J\mathbf{F}^{-1} \cdot \boldsymbol{\sigma} \tag{A.12}$$

The First Piola-Kirchhoff stress tensor can be regarded as the internal force per unit undeformed area acting within a solid.

Second Piola-Kirchhoff stress:

$$\mathbf{S} = J\mathbf{F}^{-1} \cdot \boldsymbol{\sigma} \cdot \mathbf{F}^{-\mathrm{T}} \tag{A.13}$$

The Second Piola-Kirchhoff stress tensor can also be visualized as force per unit undeformed area, except that the forces are regarded as acting within the undeformed solid, rather than on the deformed solid.

In general, it is best not to try to attach too much physical significance to these stress measures. Cauchy stress is the best physical measure of internal force—it is the force per unit area acting inside the deformed solid. The other stress measures are best regarded as generalized forces (in the sense of Lagrangian mechanics), which are work-conjugate to particular strain measures.

A.3 Objectivity or Frame Invariance

In the theory of plasticity, constitutive equations, in general, are given in rate form as the relation between a stress rate and a strain rate (or the rate of deformation). The constitutive relation must be frame invariant or objective *i.e.* independent of any rigid body motions. Objectivity is the principle that an observer, wherever he may be located, always observes the same stress in a given body. If the stress and strain measures are material quantities then objectivity is automatically satisfied. However, if the quantities are spatial, then the objectivity of the stress rate is not guaranteed even if the strain rate is objective.

Under rigid body rotations, the Cauchy stress tensor $\boldsymbol{\sigma}$ transforms as

$$\boldsymbol{\sigma}_{\mathrm{r}} = \mathbf{Q} \cdot \boldsymbol{\sigma} \cdot \mathbf{Q}^{\mathrm{T}}; \qquad \mathbf{Q} \cdot \mathbf{Q}^{\mathrm{T}} = \mathbf{I} \tag{A.14}$$

Since $\boldsymbol{\sigma}$ is a spatial quantity and the transformation follows the rules of tensor transformations, $\boldsymbol{\sigma}$ is objective.

However, the material time derivative of the Cauchy stress tensor is not an objective stress rate.

$$\dot{\boldsymbol{\sigma}}_{\mathrm{r}} = \dot{\mathbf{Q}} \cdot \boldsymbol{\sigma} \cdot \mathbf{Q}^{\mathrm{T}} + \mathbf{Q} \cdot \dot{\boldsymbol{\sigma}} \cdot \mathbf{Q}^{\mathrm{T}} + \mathbf{Q} \cdot \boldsymbol{\sigma} \cdot \dot{\mathbf{Q}}^{\mathrm{T}} \tag{A.15}$$

or

$$\dot{\boldsymbol{\sigma}}_{\mathrm{r}} \neq \mathbf{Q} \cdot \dot{\boldsymbol{\sigma}} \cdot \mathbf{Q}^{\mathrm{T}} \tag{A.16}$$

Therefore the stress rate is *not objective* unless the rate of rotation is zero, *i.e.* $\mathbf{Q}$ is constant. To overcome this problem modified time derivatives may be constructed to preserve objectivity. A commonly used objective rate is the co-rotational stress rate

$$\overset{\nabla}{\boldsymbol{\sigma}} = \dot{\boldsymbol{\sigma}} - \mathbf{W} \cdot \boldsymbol{\sigma} + \boldsymbol{\sigma} \cdot \mathbf{W} \tag{A.17}$$

also frequently referred to as the Jaumann rate.

A.4 Finite Element Formulation

The thermo-mechanically coupled problem to be solved is defined by the conservation of mass, momentum, moment of momentum and energy. These principles lead to the following equations, respectively:

$$\dot{\rho} + \rho \nabla \cdot \mathbf{v} = 0 \tag{A.18a}$$

$$\rho \dot{\mathbf{v}} = \nabla \cdot \boldsymbol{\sigma} + \rho \mathbf{b} \tag{A.18b}$$

$$\boldsymbol{\sigma} = \boldsymbol{\sigma}^{\mathrm{T}} \tag{A.18c}$$

$$\rho \dot{U}_{\mathrm{int}} = \boldsymbol{\sigma} : \mathbf{D} - \nabla \cdot \mathbf{q} + \rho r \tag{A.18d}$$

where ρ is the mass density, $\mathbf{v}$ the velocity, $\boldsymbol{\sigma}$ the Cauchy stress, $\mathbf{b}$ the body force per unit mass, U_{int} the internal energy per unit mass, $\mathbf{D}$ the rate of deformation, $\mathbf{q}$ the heat flux and r represents a specific heat source. The stress $\boldsymbol{\sigma}$ is a result of the strain and strain history and the heat flux $\mathbf{q}$ is a function of the temperature gradient. In sheet forming simulations, the acceleration term $\dot{\mathbf{v}}$ is usually neglected due to the quasi-static nature of the problem.

These equilibrium conditions have to be fulfilled in a given configuration, which is not known beforehand along with the unknown displacement and temperature fields. Thus, the thermo-mechanical problem to be solved can be defined as: find a displacement field $\mathbf{d}(\mathbf{x})$ and temperature field $T(\mathbf{x})$ such that the balance equations are fulfilled, subject to the essential boundary conditions:

$$\mathbf{d} = \bar{\mathbf{d}} \quad \text{on } \Gamma_{\mathrm{d}} \qquad T = \bar{T} \quad \text{on } \Gamma_{\mathrm{T}} \tag{A.19}$$

and the natural boundary conditions

$$\boldsymbol{\sigma} \cdot \mathbf{n} = \bar{\mathbf{t}} \quad \text{on } \Gamma_{\mathrm{t}} \qquad \mathbf{q} \cdot \mathbf{n} = -\bar{h} \quad \text{on } \Gamma_{\mathrm{h}} \tag{A.20}$$

where Γ_{d} is that part of the boundary on which the displacements $\bar{\mathbf{d}}$ are prescribed, Γ_{T} the part where the temperature $\bar{T}$ is prescribed, Γ_{t} the part where the traction $\bar{\mathbf{t}}$ is prescribed and Γ_{h} the part where the heat flux $\bar{h}$ into the body is prescribed. Ω is the analyzed deformed domain.

A.4.1 Weak Equilibrium

Using the weighted residual method, integration by parts and the divergence theorem, the weak form of the momentum equation becomes

$$\int_{\Omega} \nabla \mathbf{w}_{\mathrm{d}} : \boldsymbol{\sigma} \, \mathrm{d}\Omega - \int_{\Omega} \mathbf{w}_{\mathrm{d}} \cdot \rho \mathbf{b} \, \mathrm{d}\Omega - \int_{\Gamma_t} \mathbf{w}_{\mathrm{d}} \cdot \bar{\mathbf{t}} \, \mathrm{d}\Gamma = 0 \quad \forall \, \mathbf{w}_{\mathrm{d}} \in \mathbb{V} \tag{A.21}$$

where $\mathbb{V}$ contains all C_0 vector functions with a value of 0 on Γ_d. Similarly, the weak form of conservation of energy equation follows:

$$\int_{\Omega} w_{\mathrm{T}} (\rho \dot{U} - \boldsymbol{\sigma} : \mathbf{D}) \, \mathrm{d}\Omega - \int_{\Omega} \nabla w_{\mathrm{T}} \cdot \mathbf{q} \, \mathrm{d}\Omega - \int_{\Gamma_{\mathrm{h}}} w_{\mathrm{T}} \bar{h} \, \mathrm{d}\Gamma - \int_{\Omega} w_{\mathrm{T}} \rho r \, \mathrm{d}\Omega = 0 \quad \forall \, w_{\mathrm{T}} \in \mathbb{T} \tag{A.22}$$

where $\mathbb{T}$ contains all C_0 functions with a value of 0 on Γ_T. This equation is often referred to as the virtual heat equation.

The weak form of momentum equation (A.21) and energy equation (A.22) have the advantage over their respective strong forms in Equations (A.18b) and (A.18d) that less stringent demands are imposed on differentiability of the solution.

A spatial discretization is used to discretize the space dimension, such as the *finite elements* based on the Galerkin method to find an approximate solution of the weak equilibrium equations. The nodal displacements and temperatures are the unknowns, assembled in a vector $\mathbf{u}$. The first integral in (A.21) and second integral in (A.22) depend on the current stress and heat flux and are denoted as internal force vector $\mathbf{f}_{\mathrm{int}}$. In the first integral of (A.22) $\dot{U}$ and $\mathbf{D}$ relate directly to the first time derivative of the nodal temperatures and displacements resepectively. The remaining integral terms of both equations are related to the externally applied force vector $\mathbf{f}_{\mathrm{ext}}$. Under the condition that the discretized weak form of momentum and energy balance equations are fulfilled for every admissible weighting vector $\mathbf{w}$, the semi-discrete equations in vector form become

$$\mathbf{f}_{\mathrm{int}} - \mathbf{f}_{\mathrm{ext}} = \mathbf{0} \tag{A.23}$$

The semi-discrete equations in (A.23) are generally nonlinear due to plastic deformation and large strains and displacements; therefore an incremental-iterative strategy is applied. Extensive presentation of deriving and solving these semi-discretized equations using the incremental-iterative approach is given by Van den Boogaard (2002).

B. Derivatives of the Flow Stress for the Nes Model

B.1 Athermal Stress

In Equation (3.31) for the athermal stress contribution, the relations for τ_p and τ_{cl} are constant with respect to the microstructure evolution.
Therefore, $\frac{d\tau_a}{d\gamma} = \frac{d\tau_d}{d\gamma} = \frac{\partial\tau_d}{\partial\rho_i}\frac{\partial\rho_i}{\partial\gamma} + \frac{\partial\tau_d}{\partial\delta}\frac{\partial\delta}{\partial\rho_i}\frac{\partial\rho_i}{\partial\gamma}$. $\frac{\partial\tau_d}{\partial\rho_i}$ and $\frac{\partial\tau_d}{\partial\delta}$ are given as follows:

$$
\begin{aligned}
\frac{\partial\tau_d}{\partial\rho_i} = {} & \frac{\alpha_1 Gb}{2\sqrt{\rho_i}} + \left[\exp\left(-\frac{5q_c}{\delta\sqrt{\rho_i}}\right)\alpha_1 Gb\left(\frac{5q_c}{\delta}\right)\left(\frac{1}{2}\rho_i^{-\frac{3}{2}}\right)\sqrt{\rho_i}\right] \\
& \left[\sum_{n=0}^{7}\frac{n}{n!}\left(\frac{5q_c}{\delta\sqrt{\rho_i}}\right)^{n-1} - \sum_{n=0}^{7}\frac{1}{n!}\left(\frac{5q_c}{\delta\sqrt{\rho_i}}\right)^{n}\right] \\
& + \frac{1}{2\sqrt{\rho_i}}\exp\left(-\frac{5q_c}{\delta\sqrt{\rho_i}}\right)\sum_{n=0}^{7}\frac{1}{n!}\left(\frac{5q_c}{\delta\sqrt{\rho_i}}\right)^{n} \\
& + \left[\frac{5}{7}\exp\left(-\frac{5q_c}{\delta\rho_i}\right)\left(\frac{5q_c^2}{\delta^2}\right)\left(\frac{1}{2}\rho_i^{-\frac{3}{2}}\right)\right] \\
& \left(\sum_{n=0}^{6}\frac{1}{n!}\left(\frac{5q_c}{\delta\sqrt{\rho_i}}\right)^{n} - \sum_{n=0}^{6}\frac{1}{n!}n\left(\frac{5q_c}{\delta\sqrt{\rho_i}}\right)^{n-1}\right) \\
& + \frac{\alpha_2 Gb}{1-\Gamma(1)}\left[\exp\left(-\frac{5q_c}{\delta\sqrt{\rho_i}}\right)\left(\frac{5q_c}{\delta}\right)\left(\frac{1}{2}\rho_i^{-\frac{3}{2}}\right)\right] \\
& \left[\sum_{n=0}^{7}\frac{n}{n!}\left(\frac{5q_c}{\delta\sqrt{\rho_i}}\right)^{n-1} - \sum_{n=0}^{7}\frac{1}{n!}\left(\frac{5q_c}{\delta\sqrt{\rho_i}}\right)^{n}\right] \\
& + \frac{\alpha_2^{sc} Gb}{1-\Gamma(1)}\left[\exp\left(-\frac{5q_c}{\delta\sqrt{\rho_i}}\right)\left(\frac{5q_c}{\delta}\right)\left(\frac{1}{2}\rho_i^{-\frac{3}{2}}\right)\right] \\
& \left(\sum_{n=0}^{7}\frac{1}{n!}\left(\frac{5q_c}{\delta\sqrt{\rho_i}}\right)^{n} - \sum_{n=0}^{7}\frac{n}{n!}\left(\frac{5q_c}{\delta\sqrt{\rho_i}}\right)^{n-1}\right)\left[\Gamma_2(0)\frac{1}{\delta} + \frac{1}{D}\right]
\end{aligned}
\tag{B.1}
$$

$$
\begin{aligned}
\frac{\partial \tau_\mathrm{d}}{\partial \delta} &= \alpha_1 G b \left[\exp\left(-\frac{5q_\mathrm{c}}{\delta\sqrt{\rho_\mathrm{i}}} \right) \left(\frac{1}{\delta^2} \right) 5q_\mathrm{c} \right] \\
&\left[\sum_{n=0}^{7} \frac{n}{n!} \left(\frac{5q_\mathrm{c}}{\delta\sqrt{\rho_\mathrm{i}}} \right)^{n-1} - \sum_{n=0}^{7} \frac{1}{n!} \left(\frac{5q_\mathrm{c}}{\delta\sqrt{\rho_\mathrm{i}}} \right)^{n} \right] \\
&+ \alpha_1 G b \left[\frac{5}{7} \exp\left(-\frac{5q_\mathrm{c}}{\delta\sqrt{\rho_\mathrm{i}}} \right) \frac{5q_\mathrm{c}^2}{\delta^3\sqrt{\rho_\mathrm{i}}} \right] \\
&\left[\sum_{n=0}^{6} \frac{1}{n!} \left(\frac{5q_\mathrm{c}}{\delta\sqrt{\rho_\mathrm{i}}} \right)^{n} - \sum_{n=0}^{6} \frac{n}{n!} \left(\frac{5q_\mathrm{c}}{\delta\sqrt{\rho_\mathrm{i}}} \right)^{n-1} \right] \\
&- \alpha_1 G b \left[\frac{5}{7} \exp\left(-\frac{5q_\mathrm{c}}{\delta\sqrt{\rho_\mathrm{i}}} \right) \frac{q_\mathrm{c}}{\delta^2} \sum_{n=0}^{6} \frac{1}{n!} \left(\frac{5q_\mathrm{c}}{\delta\sqrt{\rho_\mathrm{i}}} \right)^{n} \right] \\
&+ \frac{\alpha_2 G b}{1-\Gamma_1(1)} \left[\exp\left(-\frac{5q_\mathrm{c}}{\delta\sqrt{\rho_\mathrm{i}}} \right) \frac{5q_\mathrm{c}}{\delta^2\sqrt{\rho_\mathrm{i}}} \right] \left[\Gamma_2(0) \frac{1}{\delta} + \frac{1}{D} \right] \\
&\left[\sum_{n=0}^{7} \frac{1}{n!} \left(\frac{5q_\mathrm{c}}{\delta\sqrt{\rho_\mathrm{i}}} \right)^{n} - \sum_{n=0}^{7} \frac{n}{n!} \left(\frac{5q_\mathrm{c}}{\delta\sqrt{\rho_\mathrm{i}}} \right)^{n-1} \right] \\
&+ \frac{\alpha_2^{\mathrm{sc}} G b}{1-\Gamma_1(1)} \left[\exp\left(-\frac{5q_\mathrm{c}}{\delta\sqrt{\rho_\mathrm{i}}} \right) \frac{5q_\mathrm{c}}{\delta^2\sqrt{\rho_\mathrm{i}}} \right] \left[\Gamma_2(0) \frac{1}{\delta} + \frac{1}{D} \right] \\
&\left[\sum_{n=0}^{7} \frac{n}{n!} \left(\frac{5q_\mathrm{c}}{\delta\sqrt{\rho_\mathrm{i}}} \right)^{n-1} - \sum_{n=0}^{7} \frac{1}{n!} \left(\frac{5q_\mathrm{c}}{\delta\sqrt{\rho_\mathrm{i}}} \right)^{n} \right] \\
&+ \alpha_2 G b \left[1 - \frac{1 - \left(1 - \exp\left(-\frac{5q_\mathrm{c}}{\delta\sqrt{\rho_\mathrm{i}}} \right) \sum_{n=0}^{7} \frac{1}{n!} \left(\frac{5q_\mathrm{c}}{\delta\sqrt{\rho_\mathrm{i}}} \right)^{n} \right)}{\Gamma_1(1) - 1} \right] \frac{\Gamma_2(0)}{\delta^2} \\
&+ \alpha_2^{\mathrm{sc}} G b \left[\frac{1 - \left(1 - \exp\left(-\frac{5q_\mathrm{c}}{\delta\sqrt{\rho_\mathrm{i}}} \right) \sum_{n=0}^{7} \frac{1}{n!} \left(\frac{5q_\mathrm{c}}{\delta\sqrt{\rho_\mathrm{i}}} \right)^{n} \right)}{\Gamma_1(1) - 1} \right] \frac{\Gamma_2(0)}{\delta^2}
\end{aligned}
\tag{B.2}
$$

B.2 Thermal Stress

Equation (3.30) can be written in dimensionless quantities as follows:

$$
\tau_\mathrm{t} = \frac{\Pi_2 T}{\omega_\mathrm{t} c_\mathrm{sc}^{-e_\mathrm{t}}} \operatorname{arcsinh}\left(\frac{\Pi_1^2 \omega_\mathrm{t} c_\mathrm{sc}^{1-e_\mathrm{t}} \dot{\gamma}}{2 B_\mathrm{t}^s m \left[\rho_\mathrm{i} + \Pi_1 \frac{\kappa_0 \varphi}{\delta} \right]} \exp\left(\Pi_3 \frac{U_\mathrm{sd}}{T} - \Pi_4 \right) \right) \tag{B.3}
$$

For simplicity, let

$$
\tau_\mathrm{t} = \Xi \cdot \Lambda \tag{B.4}
$$

Then

$$
\tau_\mathrm{t}' = \Xi' \cdot \Lambda + \Xi \cdot \Lambda' \tag{B.5}
$$

where

$$\Xi = \frac{\Pi_2 T}{\omega_t c_{sc}^{-e_t}}$$

with

$$c_{sc} = c_0 + c + (c_{ss} - c)\left[1 - \exp\left(-\Theta^{n_{sc}}\right)\right]$$

and

$$\Theta = \frac{B_{sc} m}{\Pi_1^2 \dot{\gamma}} \exp\left(\Pi_4 - \Pi_3 \frac{U_{sd}}{T}\right)\left(\rho_i + \Pi_1 \frac{\kappa_0 \varphi}{\delta}\right)$$

and

$$\Lambda = \left(\Lambda_{aas} + \sqrt{1 + \Lambda_{aas}^2}\right)$$

with

$$\Lambda_{aas} = \exp\left(\frac{\Pi_3 U_t^s}{T} - \Pi_4 + \log\left(\Lambda_{pe}\right)\right)$$

and

$$\Lambda_{pe} = \frac{\Pi_1^2 \omega_t \dot{\gamma} c_{sc}^{1-e_t}}{2 m B_t^s \left[\rho_i + \Pi_1 \frac{\kappa_0 \varphi}{\delta}\right]}$$

Then

$$\frac{\partial \tau_t}{\partial(\dots)} = \frac{\partial \tau_t}{\partial \Xi} \cdot \frac{\partial \Xi}{\partial(\dots)} \cdot \Lambda + \Xi \cdot \frac{\partial \tau_t}{\partial \Lambda} \cdot \frac{\partial \Lambda}{\partial(\dots)} \tag{B.6}$$

with

$$\frac{\partial \Xi}{\partial(\dots)} = \frac{\partial \Xi}{\partial c_{sc}} \cdot \frac{\partial c_{sc}}{\partial \Theta} \cdot \frac{\partial \Theta}{\partial(\dots)} \tag{B.7}$$

$$\frac{\partial \Lambda}{\partial(\dots)} = \frac{\partial \Lambda}{\partial \Lambda_{aas}} \cdot \frac{\partial \Lambda_{aas}}{\partial \Lambda_{pe}} \cdot \frac{\partial \Lambda_{pe}}{\partial(\dots)} \tag{B.8}$$

Hence

$$\frac{\partial \Xi}{\partial c_{sc}} = \frac{\Xi}{c_{sc}}; \qquad \frac{\partial c_{sc}}{\partial \Theta} = (c_{sc} - c)\exp\left(-\Theta^{n_{sc}}\right) n_{sc} \Theta^{n_{sc}-1}$$

similarly

$$\frac{\partial \Lambda}{\partial \Lambda_{aas}} = \frac{1}{\Lambda_{aas} + \sqrt{\Lambda_{aas}^2 + 1}}\left(1 + \frac{\Lambda_{aas}}{\sqrt{\Lambda_{aas}^2 + 1}}\right);$$

$$\frac{\partial \Lambda_{aas}}{\partial \Lambda_{pe}} = \exp\left(\frac{\Pi_3 U_t^s}{T} - \Pi_4 + \log\left(\Lambda_{pe}\right)\right)\frac{1}{\Lambda_{pe}}$$

Now

$$\frac{\partial\Theta}{\partial\rho_\mathrm{i}} = \frac{B_\mathrm{sc}m}{\Pi_1^2\dot{\gamma}}\exp\left(\Pi_4 - \Pi_3\frac{U_\mathrm{sd}}{T}\right) \tag{B.9}$$

$$\frac{\partial\Theta}{\partial\delta} = \frac{B_\mathrm{sc}m}{\Pi_1^2\dot{\gamma}}\exp\left(\Pi_4 - \Pi_3\frac{U_\mathrm{sd}}{T}\right)\left(-\Pi_1\frac{\kappa_0\varphi}{\delta^2}\right) \tag{B.10}$$

$$\frac{\partial\Theta}{\partial\varphi} = \frac{B_\mathrm{sc}m}{\Pi_1^2\dot{\gamma}}\exp\left(\Pi_4 - \Pi_3\frac{U_\mathrm{sd}}{T}\right)\left(\Pi_1\frac{\kappa_0}{\delta}\right) \tag{B.11}$$

$$\frac{\partial\Theta}{\partial\dot{\gamma}} = -\frac{B_\mathrm{sc}m}{\Pi_1^2\dot{\gamma}^2}\exp\left(\Pi_4 - \Pi_3\frac{U_\mathrm{sd}}{T}\right)\left(\rho_\mathrm{i} + \Pi_1\frac{\kappa_0\varphi}{\delta}\right) \tag{B.12}$$

and

$$\frac{\partial\Lambda_\mathrm{pe}}{\partial\rho_\mathrm{i}} = \Lambda_\mathrm{pe}c_\mathrm{sc}^{1-e_\mathrm{t}}(1-e_\mathrm{t})c_\mathrm{sc}^{-e_\mathrm{t}}\frac{\partial c_\mathrm{sc}}{\partial\Theta}\frac{\partial\Theta}{\partial\rho_\mathrm{i}} - \Lambda_\mathrm{pe} \tag{B.13}$$

$$\frac{\partial\Lambda_\mathrm{pe}}{\partial\delta} = \Lambda_\mathrm{pe}c_\mathrm{sc}^{1-e_\mathrm{t}}(1-e_\mathrm{t})c_\mathrm{sc}^{-e_\mathrm{t}}\frac{\partial c_\mathrm{sc}}{\partial\Theta}\frac{\partial\Theta}{\partial\delta} + \Lambda_\mathrm{pe}\left(\Pi_1\frac{\kappa_0\varphi}{\delta^2}\right) \tag{B.14}$$

$$\frac{\partial\Lambda_\mathrm{pe}}{\partial\varphi} = \Lambda_\mathrm{pe}c_\mathrm{sc}^{1-e_\mathrm{t}}(1-e_\mathrm{t})c_\mathrm{sc}^{-e_\mathrm{t}}\frac{\partial c_\mathrm{sc}}{\partial\Theta}\frac{\partial\Theta}{\partial\varphi} - \Lambda_\mathrm{pe}\left(\Pi_1\frac{\kappa_0}{\delta}\right) \tag{B.15}$$

$$\frac{\partial\Lambda_\mathrm{pe}}{\partial\dot{\gamma}} = \Lambda_\mathrm{pe}c_\mathrm{sc}^{1-e_\mathrm{t}}(1-e_\mathrm{t})c_\mathrm{sc}^{-e_\mathrm{t}}\frac{\partial c_\mathrm{sc}}{\partial\Theta}\frac{\partial\Theta}{\partial\dot{\gamma}} + \Lambda_\mathrm{pe}\left(\frac{c_\mathrm{sc}^{1-e_\mathrm{t}}}{\dot{\gamma}}\right) \tag{B.16}$$

with dimensionless quantities: Π_1, Π_2, Π_3 and Π_4 given by:

$$\Pi_1 = \frac{G_\mathfrak{sc}}{\tau_\mathfrak{sc}} \qquad \Pi_2 = \frac{kT_\mathfrak{sc}}{\tau_\mathfrak{sc}b^3} \tag{B.17}$$

$$\Pi_3 = \frac{U_\mathfrak{sc}}{kT_\mathfrak{sc}} \qquad \Pi_4 = \ln\left(\nu_\mathrm{D}t_\mathfrak{sc}\right) \tag{B.18}$$

$(\ldots)_\mathfrak{sc}$ are the respective scaling parameters.

Bibliography

Abedrabbo, N., F. Pourboghrat and J. Carsley (2007), Forming of AA 5182-O and AA 5754-O at elevated temperatures using coupled thermo-mechanical finite element models, *International Journal of Plasticity*, vol. 23, pp. 841–875.

Andersen, S. J., H. W. Zandbergen, J. Jansen, C. Treholt and U. Tundal (1998), The crystal structure of the β'' phase in Al–Mg–Si alloys, *Acta Materialia*, vol. 46, pp. 3283–3298.

Atzema, E. H. (2003), The new trend in strain measurements: fast, accurate and portable: PHAST^{TM}, in: U. P. Singh *et al.* (eds.), *Sheet Metal 2003: Proc. of 10th Int. Conf.*, pp. 405–412.

Ayres, R. and M. Wenner (1979), Strain and strain rate hardening effects in punch stretching of 5182-o aluminum at elevated temperatures, *Metallurgical Transactions A*, vol. 10, pp. 41–46.

Bacroix, B. and J. J. Jonas (1988), The influence of non-octahedral slip on texture development in fcc metals, *Textures and Microstructures*, vol. 8, pp. 267–311.

Barlat, F., J. C. Brem, J. W. Yoon, K. Chung, R. E. Dick, D. J. Lege, F. Pourboghrat, S. H. Choi and E. Chu (2003), Plane stress yield function for aluminum alloy sheets—part 1: Theory, *International Journal of Plasticity*, vol. 19, pp. 1297–1319.

Batoz, J. L. and P. Lardeur (1989), A discrete shear triangular element with nine d.o.f. for the analysis of thick to very thin plates, *International Journal for Numerical Methods and Engineering*, vol. 28, pp. 533–560.

Belytschko, T., W. K. Liu and B. Moran (2006), *Nonlinear finite elements for continua and structures*, Wiley, Chichester.

Bergström, Y. (1969), Dislocation model for the stress–strain behavior of polycrystalline α-Fe with special emphasis on the variation of the densities of mobile and immobile dislocations, *Materials Science and Engineering*, vol. 5, pp. 193–200.

Bergström, Y. (1983), The plastic deformation of metals—a dislocation model and its applicability, *Reviews on Powder Metallurgy and Physical Ceramics*, vol. 2, pp. 105–115.

Bolt, P., N. Lamboo and P. Rozier (2001), Feasibility of warm drawing of aluminum products, *Journal of Materials Processing Technology*, vol. 115, pp. 118–121.

Bolt, P. J., N. A. P. M. Lamboo, J. F. C. van Leeuwen and R. J. Werkhoven (2000), Warm drawing of aluminium components, in: *Proceedings of the 7th Saxon Conference on Forming Technology, Lightweight Construction by Forming Technology*, pp. 101–118, Chemnitz, Germany.

Bowen, R. M. and C. C. Wang (1989), *Introduction to Continuum Mechanics for Engineers*, Plenum Press, Newyork, USA.

Bray, J. W. (1990), Properties and selection: Nonferrous alloys and special purpose mate-

rials, in: J. R. Davis, P. Allen, S. R. Lampman and T. B. Zorc (eds.), *Metals Handbook*, vol. 2, pp. 29–72, ASM International, Materials Park, Ohio.

Brown, A. F. (2009), *Applied Mechanics of Solids*, CRC Press, Ohio, USA.

Carle, D. and G. Blount (1999), The suitability of aluminium as an alternative material for car bodies, *Materials and Design*, vol. 20, pp. 267–272.

Chadwick, P. (1976), *Continuum Mechanics, Concise Theory and Problems*, George Allen & Unwin Ltd., London.

Chancerelle, G. (2002), The sheet stretch forming, in: K. Siegert (ed.), *New Developments in Sheet Metal Forming Technology*, pp. 71–90, Fellbach, Germany.

Courtney, T. H. (1990), *Mechanical behaviour of materials*, McGraw–Hill.

Crisfield, M. A. (1997), *Non-linear finite element analysis of solids and structures, Vol. 2: Advanced Topics*, J. Wiley & Sons, New York.

Deschamps, A. and Y. Bréchet (1999a), Influence of predeformation on ageing in an Al–Zn–Mg alloy — part I : microstructure evolution and mechanical properties, *Acta Materialia*, vol. 47, pp. 281–292.

Deschamps, A. and Y. Bréchet (1999b), Influence of predeformation on ageing in an Al–Zn–Mg alloy — part II : Modeling of precipitation kinetics and yield stress, *Acta Materialia*, vol. 47, pp. 293–305.

Drysdale, R. J. and A. S. Bahrani (1985), The effect of annealing processes on the limit strains of an aluminum alloy, *Journal of Mechanical Working Technology*, vol. 11, pp. 105–114.

Dutta, I. and S. M. Allen (1991), A calorimetric study of precipitation in commercial aluminum alloy 6061, *Journal of Materials Science Letters*, vol. 10, pp. 323–326.

Edwards, G. A., K. Stiller, G. L. Dunlop and M. J. Couper (1998), The precipitation sequence in Al–Mg–Si alloys, *Acta Materialia*, vol. 46 (11), pp. 3893–3904.

Estrin, Y. (1996), Dislocation density related constitutive modeling, in: A. S. Krausz and K. Krausz (eds.), *Unified Constitutive Laws of Plastic Deformation*, pp. 69–104, Academic Press, San Diego.

Finch, D., S. Wilson and J. Dorn (1946), Deep drawing aluminium alloys at elevated temperatures, part–i: Deep drawing cylindrical cups, *Transactions ASM*, vol. 36, pp. 254–289.

Helms, H., U. Lambrecht and U. Höpfner (2005), Energy savings by lightweighting, Institute for Energy and Environmental Research, Heidelberg.

Hill, R. (1948), A theory of the yielding and plastic flow of anisotropic metals, *Proceedings of the Royal Society of London; Series A*, vol. 193, pp. 281–297.

Hol, J. (2009), *Optimization of the stretch forming process using the finite element method*, Master Thesis, University of Twente.

Holmedal, B., O. Engler and E. Nes (2005a), Modelling dynamic strain ageing in aluminium magnesium alloys, in: A. Khan and A. Khoei (eds.), *Dislocations, Plasticity, Damage and Metal Forming: Material Response and Multiscale Modeling*, pp. 334–336, Neat Press, Maryland, USA.

Holmedal, B., K. Marthinsen and E. Nes (2005b), A unified microstructural metal plasticity model applied in testing, processing, and forming of aluminum alloys, *Zeitschrift für Metallkunde*, vol. 96, pp. 532–545.

Hosford, W. F. (1972), A generalized isotropic yield criterion, *Journal of Applied Mechanics*, vol. 39, pp. 607–609.

Hull, D. (1965), *Introduction to dislocations*, Pergamon Press, Oxford.

Humphreys, F. J. and M. Haterly (2004), *Recrystallization and Related Annealing Phenomena*, Elsevier Ltd, Oxford, UK.

Jaspart, O., A. François, O. Magotte and L. D'Alvise (2004), Numerical simulation of the stretch forming process for prediction of fracture and surface defect, in: *7th ESAFORM Conference on Material Forming*, pp. 499–502, Trondheim, Norway.

Kuo, C. M. and C. S. Lin (2007), Static recovery activation energy of pure copper at room temperature, *Scripta Materialia*, vol. 57, pp. 667–670.

Kurukuri, S., A. H. van den Boogaard, A. Miroux and B. Holmedal (2009), Warm forming simulation of Al–Mg sheet, *Journal of Materials Processing Technology*, vol. 209, pp. 5636–5645.

Laughlin, D. E., W. F. Miao, L. M. Karabin and D. J. Chakrabarti (1998), Precipitation mechanism in Al–Mg–Si alloys, in: S. Das (ed.), *Automotive Alloys II*, pp. 63–79, TMS, Warrendale, PA.

Lebensohn, R. A. and C. N. Tomé (1993), A self-consistent anisotropic approach for the simulation of plastic deformation and texture development of polycrystals: Application to zirconium alloys, *Acta Metallurgica et Materialia*, vol. 41, pp. 2611–2624.

Li, D. and A. Ghosh (2003), Tensile deformation behavior of aluminum alloys at warm forming temperatures, *Materials Science and Engineering A*, vol. 352, pp. 279–286.

Malvern, L. E. (1969), *Introduction to the mechanics of a continuous medium*, Prentice-Hall Inc., Englewood Cliffs, New Jersey.

Martchek, K. J. (2006), Modeling more sustainable aluminum: case study, *International Journal of Life Cycle Assessment*, vol. 11, pp. 34–37.

Marthinsen, K. and E. Nes (2001), Modelling strain hardening and steady state deformation of Al–Mg alloys, *Materials Science and Technology*, vol. 17, pp. 376–388.

McMurray, R. J., M. O'Donnell, A. G. Leacock and D. Brown (2009), Modelling the effect of pre-strain and inter-stage annealing on the stretch forming of a 2024 aluminum alloy, *Key Engineering Materials*, vol. 410–411, pp. 421–428.

Merklein, M., W. Hußnätter and M. Geiger (2008), Characterization of yielding behavior of sheet metal under biaxial stress condition at elevated temperatures, *CIRP Annals – Manufacturing Technology*, vol. 57, pp. 269–274.

Mildenberger, U. and A. Khare (2000), Planning for an environment-friendly car, *Technovation*, vol. 20, pp. 205–214.

Miller, W. S., L. Zhuang, J. Bottema, A. J. Wittebrood, P. de Smet, A. Haszler and A. Vieregge (2000), Recent developments in aluminium alloys for the automotive industry, *Materials Science and Engineering A*, vol. 280, pp. 37–49.

Moon, Y. H., Y. K. Kang, J. W. Park and S. R. Gong (2001), Tool temperature control to increase the deep drawability of aluminum 1050 sheet, *Machine Tools and Manufacture*, vol. 41, pp. 1283–1294.

Myhr, O. R., O. Grong and S. J. Andersen (2001), Modelling of the age hardening behavior of Al–Mg–Si alloys, *Acta Materialia*, vol. 49, pp. 65–75.

Naka, T., Y. Nakayama, T. Uemori, R. Hino and F. Yoshida (2003), Effects of temperature on yield locus for 5083 aluminum alloy sheet, *Journal of Materials Processing Technology*, vol. 140, pp. 494–499.

Naka, T. and F. Yoshida (1999), Deep drawability of type 5083 aluminium-magnesium alloy sheet under various conditions of temperature and forming speed, *Journal of Materials*

Processing Technology, vol. 89–90, pp. 19–23.
Nes, E. (1994), Recovery revisited, *Acta Metallurgica et Materialia*, vol. 43, pp. 2189–2207.
Nes, E. (1998), Modelling of work hardening and stress saturation in FCC metals, *Progress in Materials Science*, vol. 145, pp. 129–193.
Nes, E. and K. Marthinsen (2002), Modelling the evolution in microstructure and properties during plastic deformation of FCC-metals and alloys—an approach towards a unified model, *Materials Science and Engineering A*, vol. 322, pp. 176–193.
Nes, E., K. Marthinsen and B. Holmedal (2004), The effect of boundary spacing on substructure strengthening, *Materials Science and Technology*, vol. 20, pp. 1377–1382.
Neugebauer, R., T. Altan, M. Geiger, M. Kleiner and A. Stezing (2006), Sheet metal forming at elevated temperatures, *Annals of the CIRP*, vol. 55, pp. 793–816.
Novotny, S. and M. Geiger (2003), Process design for hydroforming of lightweight metal sheets at elevated temperatures, *Journal of Materials Processing Technology*, vol. 138, pp. 594–599.
O'Donnell, M., D. Banabic, A. G. Leacock, D. Brown and R. J. McMurray (2008), The effect of pre-strain and inter-stage annealing on the formability of a 2024 aluminum alloy, *International Journal of Forming Processes*, vol. 1, pp. 253–256.
Pijlman, H. H. (2001), *Sheet material characterisation by multi-axial experiments*, Ph.D. thesis, University of Twente.
Reppich, B. (1993), A comprehensive treatment, in: R. W. Cahn, P. Hassen and E. J. Kramer (eds.), *Materials science and technology*, vol. 6, p. 93, VCH, Weinheim, Germany.
Rietman, A. D. (1999), *Numerical Analysis of Inhomogeneous Deformation in Plane Strain Compression*, Ph.D. thesis, University of Twente.
Rylands, L. M., D. M. J. Wilkes, W. M. Rainforth and H. Jones (1994), Coarsening of precipitates and dispersoids in aluminum alloy matrices: a consolidation of the available experimemntal data, *Journal of Materials Science*, vol. 29, pp. 1895–1900.
Shehata, F., M. J. Painter and R. Pearce (1978), Warm forming of aluminium/magnesium alloy sheet, *Journal of Mechanical Working Technology*, vol. 2, pp. 279–291.
Shercliff, H. R. and M. F. Ashby (1990a), A process model for age-hardening aluminium alloys — part I: The model, *Acta Metallurgica et Materialia*, vol. 38, pp. 1789–1802.
Shercliff, H. R. and M. F. Ashby (1990b), A process model for age-hardening aluminium alloys — part II: Applications, *Acta Metallurgica et Materialia*, vol. 38, pp. 1803–1812.
Simo, J. C. and T. J. R. Hughes (2000), *Computational inelasticity, interdisciplinary applied mathematics*, Springer, New York.
Straatsma, E. N. and L. Velterop (2004), Influence of heat treatments and straining steps on mechanical properties in the stretch forming process, in: B. C. Muddle, A. J. Morton and J. F. Nie (eds.), *9th International Conference on Aluminum Alloys*, pp. 771–776, Brisbane, Australia.
Teyssier, E. and A. Miroux (2004), *Microstructure evolutions during industrial sheet forming of AA 2024 aluminum alloy*, P04.4.063, Netherlands Institute for Metals Research (NIMR).
Toros, S., F. Ozturk and I. Kacar (2008), Review of warm forming of aluminum-magnesium alloys, *Journal of Materials Processing Technology*, vol. 207, pp. 1–12.
Van den Boogaard, A. H. (2002), *Thermally enhanced forming of aluminium sheet*, Ph.D. thesis, University of Twente.

Van den Boogaard, A. H., P. J. Bolt and R. J. Werkhoven (2001), Modeling of AlMg sheet forming at elevated temperatures, *International Journal of Forming Processes*, vol. 4, pp. 361–375.

Van den Boogaard, A. H. and J. Huétink (2006), Simulation of aluminum sheet forming at elevated temperatures, *Computer Methods in Applied Mechanics and Engineering*, vol. 195, pp. 6691–6709.

Van den Boogaard, A. H., H. H. Pijlman and J. Huétink (2000), Anisotropic yield functions in a co-rotating reference frame, in: *Third ESAFORM Conference on Material Forming*, pp. 11–14, Stuttgart, Germany.

Van Liempt, P. (1994), Work hardening and substructural geometry of metals, *Journal of Materials Processing Technology*, vol. 45, pp. 459–464.

Van Riel, M. (2009), *Strain path dependency in sheet metal*, Ph.D. thesis, University of Twente.

Vegter, H., H. L. J. ten Horn Carel, Y. U. An, E. H. Atzema, H. H. Pijlman, A. H. van den Boogaard and J. Huétink (2003), Characterization and modelling of the plastic material behavior and its application in sheet metal forming simulation, in: E. Õnate and D. R. J. Owen (eds.), *Computational Plasticity VII - Fundamentals and Applications*, pp. 1–20, CIMNE, Barcelona, Spain.

Vegter, H. and A. H. van den Boogaard (2006), A plane stress yield function for anisotropic material by interpolation of biaxial stress states., *International Journal of Plasticity*, vol. 22, pp. 557–580.

Velterop, L. (2004), *Stretch forming of aluminum — Mechanical properties AA 2024 Alclad*, nLR-TR-2004-148, National Aerospace Laboratory NLR.

Vetter, R. and A. van den Beukel (1977), Dislocation production in cold worked copper, *Scripta Metallurgica et Materialia*, vol. 11, pp. 143–146.

Wilson, D. V. (1988), Aluminium versus steel in the family car—the formability factor, *Journal of Mechanical Working Technology*, vol. 16, pp. 257–277.

Wisselink, H. H. and A. H. van den Boogaard (2005), Finite element simulation of the stretch-forming of aircraft skins, in: L. M. Smith, F. Pourboghrat, J. W. Yoon and T. B. Stoughton (eds.), *Proceedings Of The 6th International Conference and Workshop On Numerical Simulation of 3D Sheet Metal Forming Processes*, pp. 60–65, Detroit, USA.

Woodthorpe, J. and R. Pearce (1970), The anomalous behavior of aluminum sheet under balanced biaxial tension., *International Journal of Mechanical Sciences*, vol. 12, pp. 341–346.

Yoon, J. W., D. Y. Yang, K. Chung and F. Barlat (1999), A general elasto-plastic finite element formulation based on incremental deformation theory for planar anisotropy and its application to sheet metal forming, *International Journal of Plasticity*, vol. 15, pp. 35–67.

Zandbergen, H. W., S. J. Andersen and J. Jansen (1997), Structure determination of Mg_5Si_6 in Al by dynamic electron diffraction studies, *Science*, vol. 227, pp. 1221–1225.

Zienkiewicz, O. C. and R. L. Taylor (2005), *The Finite Element Method, volume 2: Solid Mechanics*, Butterworth–Heinemann, 6th edn.

Index